AGH UNIVERSITY OF SCIENCE AND TECHNOLOGY

FIELD OF SCIENCE: Engineering and Technology

SCIENTIFIC DISCIPLINE: Automation, Electronic and Electrical Engineering

DOCTORAL THESIS

Microwave directional couplers' design with the use of planar quasi-TEM transmission line sections. Analysis, experimental investigation and applications

Author: Robert Smolarz

Supervisor: Prof. Sławomir Gruszczyński

Completed in:

Faculty of Computer Science, Electronics and Telecommunications

Institute of Electronics

Krakow, 2021

Microwave directional couplers' design with the use of planar quasi-TEM transmission line sections. Analysis, experimental investigation and applications

Robert Smolarz

AGH University of Science and Technology

AGH University of Science and Technology
Institute of Electronics

Supervisor

Prof. Sławomir Gruszczyński

Declaration

I hereby declare that the work in this Thesis is my own original work, except where indicated in the text.

The Thesis is based on the following publications:

R. Smolarz, K. Staszek, K. Wincza and S. Gruszczynski, "A 24 GHz microwave sensor with built-in calibration capability designed in MMIC technology," *IEEE Access*, vol. 9, pp. 31513-31524, February 2021.

R. Smolarz, K. Wincza, and S. Gruszczynski "Modal phase velocity compensation in multilayer differentially fed directional couplers," *Microwave and Optical Technology Letters*, vol. 62, no. 5, pp. 1882-1887, May 2020.

S. Gruszczynski, R. Smolarz, and K. Wincza, "Differential Bi-Level Microstrip Directional Coupler with Equalized Coupling Coefficients for Directivity Improvement," *Electronics*, vol. 9, no. 4, pp. 547-, March 2020.

S. Gruszczynski, R. Smolarz, C. Wu, and K. Wincza, "Monolithic Miniaturized Differentially-Fed Branch-Line Directional Coupler in GaAs Monolithic Technology," *Electronics*, vol. 9, no. 3, pp. 446-, March 2020.

S. Gruszczynski, R. Smolarz, and K. Wincza, "Realization of high-performance broadband quadrature directional couplers in UMS PH25 technology," *Electronics*, vol. 8, no. 12, pp. 1520-, December 2019.

R. Smolarz, K. Wincza and S. Gruszczynski, "Impedance transforming rat-race couplers with modified Lange secton," *Journal of Electromagnetic Waves and Applications*, vol. 32, no. 8, pp. 972–983, May 2018.

R. Smolarz, K. Wincza and S. Gruszczynski, "Impedance transforming tandem couplers with increased bandwidth and transformation ratio," *IEEE Microwave and Wireless Components Letters*, vol. 28, no. 4, pp. 299–301, March 2018.

R. Smolarz, K. Wincza and S. Gruszczynski, "Design of low-loss durectional couplers with compensated coupled-line sections in suspended microstrip technique," *International Joutnal of RF and Microwave Computer-Aided Engineering*, vol. 27, no. 8, October 2017.

R. Smolarz, K. Wincza, and S. Gruszczynski, "Design of 3-dB Differentially-Fed Tandem Directional Couplers," in *Proc. of the IEEE MTT-S International Wireless Symposium (IWS)*, Guangzhou, China, May 2019, pp. 1–3.

R. Smolarz, K. Wincza, and S. Gruszczynski, "Broadband low-loss impedance transforming rat-race coupler in suspended microstrip technique," in *Proc. of the 22nd International Microwave and Radar Conference (MIKON)*, Poznan, Poland, May 2018, pp. 291–293.

K. Janisz, R. Smolarz, A. Rydosz, K. Wincza, and S. Gruszczynski, "Compensated 3-dB lange directional coupler in suspended microstrip technique," in *Proc. of the 7th IEEE International Symposium on Microwave, Antenna, Propagation, and EMC Technologies (MAPE) 2017*, Xi'an, China, October 2017, pp. 289–291.

July 2021

Microwave directional couplers' design with the use of planar quasi-TEM transmission line sections. Analysis, experimental investigation and applications

Robert Smolarz

Abstract

Modern radio communication and radiolocation systems have to fulfill ever demanding requirements. Cellular network standards such as LTE Advanced or 5G are based on operation across a broad frequency band. It is also important that wireless devices become increasingly efficient and miniaturized. These requirements can be addressed by designing integrated circuits using the strip transmission line technique in which a quasi-TEM wave propagation appears. From a practical point of view, such circuits are manufactured using *printed circuit board* (PCB) technology or on special ceramic or semiconductor substrates with *monolithic microwave integrated circuit* (MMIC) technology. In both cases, the integration of active and passive systems within one device or functional block becomes simple in terms of simulation and fabrication. However, such networks feature insertion and reflection losses that appear at the connections of mismatched circuits operating in the microwave frequencies. Another issue is related to the miniaturization aspect, which is especially crucial for passive components designed using the MMIC technique. In the case of components consisting of transmission lines (e.g. directional couplers), the geometry of the designed circuitry can exceed the size of a single integrated circuit, which is defined by a chosen technological process.

The scope of this dissertation focuses on three main aspects related to microwave directional couplers. The first concerns the possibility of improving the properties of couplers composed of coupled-line sections designed in both PCB and MMIC technologies. This work discusses the methods of even and odd phase velocity compensation in symmetrical structures, as well as the equalization of inductive and capacitive coupling coefficients in asymmetric structures. Such approaches improve the electrical performance of the couplers in terms of obtained directivity, isolation and return losses. The author proposed the utilization of such methods in single-ended and differentially-fed directional couplers. Furthermore, an investigation on the reduction of total losses in two- and four-coupled-line section has been conducted.

The second aspect is focused on the development and analysis of impedance-transforming directional couplers operating in narrow and wide frequency bandwidths. In well-known solutions, the impedance of all of the coupler's ports is the same and is equal to the standardized value of 50 Ω. In cases where such a coupler has been connected with a component that has a different impedance, an effect called impedance mismatch is observed. Such an issue has a direct influence on return loss increase, and therefore on the degradation of the total performance of the circuit. In such cases, the use of impedance-transforming directional couplers is desirable and enables the significant improvement of circuit parameters. First, a reduction of the return losses between the ports of the elements is obtained. Second, the overall size of the designed circuit can be reduced because additional matching circuits are no needed. In this work, studies related to the impedance-transforming hybrid couplers based on rat-race and tandem topologies operating in narrow and broad operational bandwidths is presented. In comparison

to well-known solutions, the impedance-transformation ratio is increased. Moreover, an enhancement of the bandwidth in the rat-race coupler is also obtained.

The last topic discussed in the dissertation focuses on the utilization of the developed directional couplers in complex, monolithic applications based on gallium arsenide. As part of the work, two miniaturized hybrid couplers in a single-ended and a differentially-fed branch-line topology have been proposed. The couplers have been used in the design of a monolithic sensor intended for measurements of material dielectric permittivities and in a monolithic balanced differentially excited amplifier, which has been designed for the purposes of this dissertation. The third of the designed chips is a monolithic *frequency-modulated continuous-wave* (FMCW) radar front end operating in the automotive frequency band, in which a previously designed compensated three-coupled-line section coupler was utilized.

The developed design methods and circuits have been experimentally verified by measurements of the fabricated structures. In each of the proposed directional couplers, the performance has been improved in relation to the existing solutions. In addition, the last chapter confirms the applicability of the developed monolithic solutions in monolithic microwave integrated circuits.

Projektowanie mikrofalowych sprzęgaczy kierunkowych w technice linii transmisyjnych quasi-TEM. Analiza, projektowanie i badania eksperymentalne.

Robert Smolarz

Streszczenie

Wymagania stawiane przed nowoczesnymi systemami radiokomunikacyjnymi i radiolokacyjnymi są coraz wyższe. Standardy sieci komórkowych takie jak LTE Advanced czy 5G opierają swoje działanie na pracy w szerokim paśmie częstotliwości. Ważne jest też, aby urządzenia radiowe osiągały coraz większą sprawność i większy stopień zminiaturyzowania. Założenia te można spełnić projektując układy zintegrowane wykorzystujące technikę linii paskowych, w których występuje zjawisko propagacji fali quasi-TEM. Z praktycznego punktu widzenia, są to obwody wykonywane na laminatach w tzw. technologii PCB (ang. *Printed Circuit Board*) lub na specjalnych podłożach pół ceramicznych, półprzewodnikowych w technologii monolitycznej. W obu tych przypadkach, zintegrowanie układów aktywnych z pasywnymi w obrębie jednego urządzenia czy też bloku funkcjonalnego staje się proste pod względem symulacji oraz wykonania. Niestety dużym problemem są straty wtrąceniowe oraz odbiciowe, które pojawiają się na połączeniach niedopasowanych układów pracujących w paśmie mikrofalowym. Inną problematyczną kwestią jest miniaturyzacja układów pasywnych projektowanych szczególnie w technice monolitycznej. W przypadku realizacji komponentów składających się z linii transmisyjnych (np. sprzęgacze kierunkowe), geometria projektowanego układu może być większa niż rozmiar pojedynczego układu scalonego, który jest zdefiniowany przez dany proces technologiczny.

Zakres niniejszej rozprawy doktorskiej skupia się na trzech głównych aspektach związanych z mikrofalowymi sprzęgaczami kierunkowymi. Pierwszy z nich dotyczy możliwości polepszenia właściwości sprzęgaczy zbudowanych z sekcji sprzężonych linii transmisyjnych wykonanych w technologii PCB i monolitycznej. W ramach pracy omówiono metody kompensacji prędkości fazowych rodzajów parzystego i nieparzystego (struktury symetryczne) oraz indukcyjnego i pojemnościowego współczynnika sprzężenia (struktury asymetryczne), które mogą być zastosowane w sprzęgaczach o pobudzeniu klasycznym (tzw. *single-ended*) lub różnicowym. Zaproponowano również rozwiązania pozwalające na projektowanie dwu- i cztero- paskowych sekcji sprzężonych o zredukowanych stratach całkowitych (sprzęgacz w topologii Langego).

Drugim aspektem jest opracowanie oraz analiza sprzęgaczy kierunkowych pozwalających na transformację impedancji w wąskim i szerokim paśmie pracy. W klasycznych rozwiązaniach, impedancja wszystkich wrót sprzęgacza jest taka sama i w większości wypadków równa 50 Ω. W przypadku, gdy do tak zaprojektowanego sprzęgacza zostanie podłączony układ o innej impedancji (np. układ nieliniowy w postaci wzmacniacza), następuję tzw. niedopasowanie impedancyjne i degradacja parametrów całego obwodu poprzez powstałe straty odbiciowe. W takim przypadku, zastosowanie sprzęgaczy kierunkowych transformujących impedancję jest wskazane i pozwala na znaczącą poprawę właściwości układowych. Po pierwsze następuje redukcja wspomnianych strat odbiciowych między wrotami elementów. Po drugie, rozmiary projektowanego obwodu mogą zostać znacząco zmniejszone, ze względu na brak dodatkowych obwodów dopasowujących. W niniejszej pracy przedstawiono opracowane wąskopasmowe i szerokopasmowe sprzęgacze hybrydowe transformujące impedancje, w których znacząco zwiększono

tzw. współczynnik transformacji impedancji oraz nastąpiło zwiększenie pasma operacyjnego. Układy te zostały oparte o topologię pierścieniową (tzw. *rat-race*) oraz tandemową zbudowaną z sekcji linii sprzężonych.

Ostatni, poruszony temat skupia się na użyciu opracowanych sprzęgaczy kierunkowych o polepszonych właściwościach do zastosowań w bardziej złożonych układach wykonanych w technice monolitycznej bazującej na arsenku galu. W ramach pracy zaproponowano dwa zminiaturyzowane sprzęgacze hybrydowe w topologii gałęziowej (tzw. *branch-line*) o pobudzeniu: single-ended i różnicowym. Zaproponowane układy zostały następnie wykorzystane kolejno w projekcie monolitycznego sensora do badań np.: przenikalności dielektrycznej materiałów oraz w monolitycznym zrównoważonym wzmacniaczu pobudzanym różnicowo, który został zaprojektowany na potrzeby niniejszej rozprawy. Trzecim z zaprojektowanych układów jest monolityczny układ radaru z ciągłą falą modulowaną częstotliwościowo FMCW (ang. *Frequency-Modulated Continuous-Wave Radar*) pracujący w paśmie przewidzianym dla branży automotive w którym wykorzystano wcześniej zaprojektowany skompensowany sprzęgacz trójpaskowy zbliżeniowy.

Opracowane metody projektowe oraz układy zostały zweryfikowane eksperymentalnie poprzez pomiary wykonanych układów lub symulacje (tak stało się jedynie w przypadku monolitycznego wzmacniacza zrównoważonego). W każdym z zaproponowanych sprzęgaczy kierunkowych stwierdzono poprawę parametrów względem znanych już rozwiązań. Dodatkowo, ostatni rozdział w którym to zweryfikowano aplikacyjność potwierdza możliwość implementacji opracowanych rozwiązań monolitycznych w monolitycznych mikrofalowych układach scalonych.

Contents

List of Figures

List of Tables

1. Introduction

This chapter is focused on the theoretical basics of coupled-line sections, directional coupler theory, and compensation methods utilized for the improvement of the electrical parameters of the directional couplers. The chapter begins with an analysis of well-known symmetrical and asymmetrical two-coupled-line sections utilized in single-ended structures, and a four-coupled-line section which is used in differentially-fed couplers. In the next Section of the chapter, the theory of the directional coupler is introduced. The last Subsection is focused on short introduction of compensation methods utilized in symmetric and asymmetric coupled-line sections.

1.1. Directional Couplers

1.1.1. Single-Ended Directional Couplers
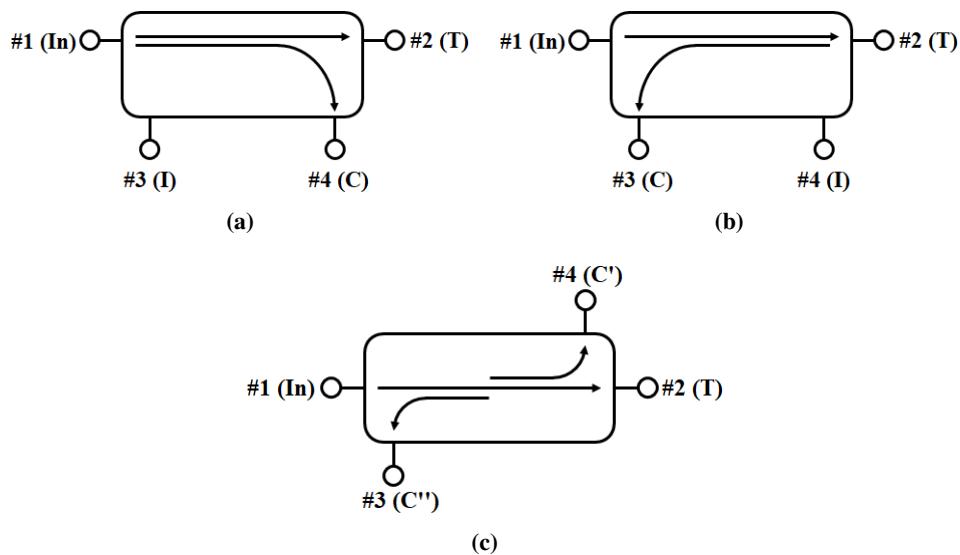
Figure 1.1: Symbols presenting directional couplers in terms of direction of signal flow: forward-wave directional coupler (a), backward-wave directional coupler (b), and dual directional coupler (c). The ports are marked: *In*- input, *T* - through, *C* - coupled, *I* - isolated.

Single-ended directional couplers are one of the most frequently utilized classes of passive components in microwave engineering [83], [71], [32], [33], [50], [51], [68]. Such elements are four-port circuits in which, by utilizing proper topology, the signal flow can be properly modified in terms of

phase shifting between ports or power division. Regarding the direction of signal flow, two general types of directional couplers can be mentioned: single-directional couplers which are additionally divided in to forward-wave structures [88], [60], backward-wave ones [13], [95] and dual-directional couplers [25], [23], [141], [148]. These components are presented in Fig. 1.1. As previously mentioned, directional couplers are a class of four-port circuits in which each port has a specific functionality. Thus, the following ports can be distinguished: input, through, coupled and isolated.

Scattering parameters (or S-Parameters) are commonly used to describe the behavior of microwave circuits. An ideal four-port component is defined by the following S-Parameters matrix [109]:

$$[S] = \begin{bmatrix} 0 & S12 & S13 & S14 \\ S21 & 0 & S23 & S24 \\ S31 & S32 & 0 & S34 \\ S41 & S42 & S43 & 0 \end{bmatrix}. \tag{1.1}$$

The Matrix 1.1 has been derived for fully matched four-port reciprocal circuit. For the lossless case, the following equations can be found [109]:

$$S_1^* 3 S_{23} + S_{14}^* S_{24} = 0 \tag{1.2}$$

$$S_{14}^* S_{13} + S_{24}^* S_{23} = 0 \tag{1.3}$$

$$S_{14}^* \left(\mid S_{13} \mid^2 - \mid S_{24} \mid^2 \right) = 0 \tag{1.4}$$

$$S_{12}^* S_{23} + S_{14}^* S_{34} = 0 \tag{1.5}$$

$$S_{14}^* S_{12} + S_{34}^* S_{23} = 0 \tag{1.6}$$

$$S_{23} \left(\mid S_{12} \mid^2 - \mid S_{34} \mid^2 \right) = 0. \tag{1.7}$$

If $S_{14} = S_{23} = 0$ is used in (1.4) and (1.7), the following relations can be seen:

$$\mid S_{12} \mid^2 + \mid S_{13} \mid^2 = 1 \tag{1.8}$$

$$\mid S_{12} \mid^2 + \mid S_{24} \mid^2 = 1 \tag{1.9}$$

$$\mid S_{13} \mid^2 + \mid S_{34} \mid^2 = 1 \tag{1.10}$$

$$\mid S_{24} \mid^2 + \mid S_{34} \mid^2 = 1 \tag{1.11}$$

which leads to the relations that $\mid S_{13} \mid = \mid S_{24} \mid$ and $\mid S_{12} \mid = \mid S_{34} \mid$. Moreover, by choosing the phase references on three of the four ports, some simplification can be done [109] $S_{12} = S_{34} = \alpha$, $S_{13} = \beta e^{j\theta}$, $S_{24} = \beta e^{j\varphi}$, where α, β are real values, and θ, φ are phase constants. As long as the dot product of rows 2 and 3 gives

$$S_{12}^* S_{13} + S_{24}^* S_{34} = 0, \tag{1.12}$$

the following relation between phase constants θ and φ is fulfilled:

$$\theta + \varphi = \pi \pm 2n\pi. \tag{1.13}$$

The integer multiples of 2π can be ignored, thus the scattering parameter matrix of the single-ended directional coupler can be obtained for two practical cases [109]:

 – *Symmetric coupler* $\theta = \varphi = \frac{\pi}{2}$). When the phases of the terms with amplitude β are chosen to be equal, then:

$$[S] = \begin{bmatrix} 0 & \alpha & j\beta & 0 \\ \alpha & 0 & 0 & j\beta \\ j\beta & 0 & 0 & \alpha \\ 0 & j\beta & \alpha & 0 \end{bmatrix} \tag{1.14}$$

 – *Antisymmetric coupler* ($\theta = 0$, $\varphi = \pi$). When the phases of the terms with amplitude β are chosen to be $180°$ apart, then:

$$[S] = \begin{bmatrix} 0 & \alpha & \beta & 0 \\ \alpha & 0 & 0 & -\beta \\ \beta & 0 & 0 & \alpha \\ 0 & -\beta & \alpha & 0 \end{bmatrix} \tag{1.15}$$

Furthermore, it must be mentioned that for both cases, between amplitudes α and β the following relation has to be assumed to achieve lossless structures:

$$\alpha^2 + \beta^2 = 1. \tag{1.16}$$

Having values of powers observed on each port of a coupler or its scattering parameters, the specific properties related to the performance of a directional coupler can be calculated. Such properties are:

 – *Coupling*:
$$C = -10log\frac{P_3}{P_1} = -20log\left(\mid S_{31} \mid\right) [dB] \tag{1.17}$$

 – *Isolation*:
$$I = -10log\frac{P_4}{P_1} = -20log\left(\mid S_{41} \mid\right) [dB] \tag{1.18}$$

 – *Directivity*:
$$D = -10log\frac{P_4}{P_3} = -20log\left(\mid S_{43} \mid\right) [dB] \tag{1.19}$$

– *Insertion Loss*:

$$L = -10log\frac{P_2}{P_1} = -20log\left(\mid S_{21} \mid\right)[dB] \tag{1.20}$$

– *Return Loss*:

$$RL = -10log\frac{P_{nn}^-}{P_{nn}^+} = -20log\left(\mid S_{nn} \mid\right)[dB] \tag{1.21}$$

where P^+ is the incident power, P^- is the reflected power, and n is the number of considered ports.

Moreover, between coupling, isolation, and the directivity of a directional coupler, the following relation holds:

$$I = D + C\,[dB]\,. \tag{1.22}$$

1.1.2. Differentially Excited Directional Couplers

One of the most desirable properties of differentially-fed circuits is related to the possibility of the rejection of additional noise. Such an aspect has a significant impact on the performance of sensitive microwave systems. Thus, improvement of differentially-fed networks such as directional couplers is crucial and has been the subject of many papers [135], [149], [106], [107], [64], [18]. The general symbol of the differentially-fed coupler is presented in Fig. 1.2. As can be seen, such a network has eight ports, which can be grouped into pairs. Such a structure can be excited in a broad-side or edge-wise configuration.
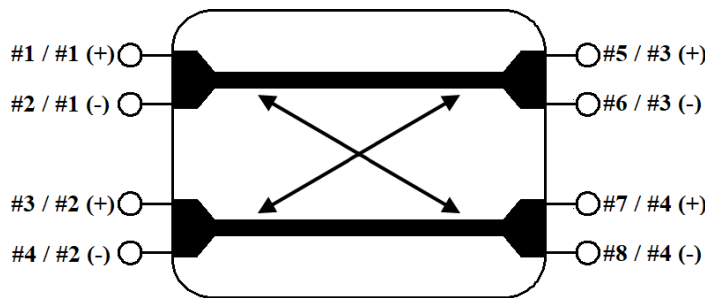
Figure 1.2: The differentially-fed coupled-lines directional coupler symbol with numbered ports used in this thesis.

The differentially-fed networks can be defined with mixed-mode scattering parameters, which have been introduced in the literature [14], [15], [35] for four-port circuits. Such an approach has also been extended for the eight-port cases [135]. By utilizing this methodology, the mixed-mode S-Parameters can be calculated from nodal simulation and measurement results. For the considered differentially-fed directional coupler consisting of a four-coupled-line section, the mixed-mode S-Parameters matrix can be written as:

$$
\begin{bmatrix}
b_{1diff} \\
b_{2diff} \\
b_{3diff} \\
b_{4diff} \\
b_{1comm} \\
b_{2comm} \\
b_{3comm} \\
b_{4comm}
\end{bmatrix}
=
\begin{bmatrix}
S_{diff} & S_{diff/comm} \\
S_{comm/diff} & S_{comm}
\end{bmatrix}
\begin{bmatrix}
a_{1diff} \\
a_{2diff} \\
a_{3diff} \\
a_{4diff} \\
a_{1comm} \\
a_{2comm} \\
a_{3comm} \\
a_{4comm}
\end{bmatrix}
\tag{1.23}
$$

The normalized power waves a and b can be derived for common and different excitations as follows [135]:

$$
\begin{aligned}
a_{1diff} &= \tfrac{1}{\sqrt{2}}(a_1 - a_2), & a_{1comm} &= \tfrac{1}{\sqrt{2}}(a_1 + a_2) \\
a_{2diff} &= \tfrac{1}{\sqrt{2}}(a_3 - a_4), & a_{2comm} &= \tfrac{1}{\sqrt{2}}(a_3 + a_4) \\
a_{3diff} &= \tfrac{1}{\sqrt{2}}(a_5 - a_6), & a_{3comm} &= \tfrac{1}{\sqrt{2}}(a_5 + a_6) \\
a_{4diff} &= \tfrac{1}{\sqrt{2}}(a_7 - a_8), & a_{4comm} &= \tfrac{1}{\sqrt{2}}(a_7 + a_8) \\
b_{1diff} &= \tfrac{1}{\sqrt{2}}(b_1 - b_2), & b_{1comm} &= \tfrac{1}{\sqrt{2}}(b_1 + b_2) \\
b_{2diff} &= \tfrac{1}{\sqrt{2}}(b_3 - b_4), & b_{2comm} &= \tfrac{1}{\sqrt{2}}(b_3 + b_4) \\
b_{3diff} &= \tfrac{1}{\sqrt{2}}(b_5 - b_6), & b_{3comm} &= \tfrac{1}{\sqrt{2}}(b_5 + b_6) \\
b_{4diff} &= \tfrac{1}{\sqrt{2}}(b_7 - b_8), & b_{4comm} &= \tfrac{1}{\sqrt{2}}(a_7 + a_8).
\end{aligned}
\tag{1.24}
$$

Moreover, it must be mentioned that according to the literature [135], the mixed-mode sub-matrices 1.23 can be defined as:

$$
S_{diff} = \frac{1}{2}
\begin{bmatrix}
S_{11} - S_{21} - S_{12} + S_{22} & S_{13} - S_{23} - S_{14} + S_{24} & S_{15} - S_{25} - S_{16} + S_{26} & S_{17} - S_{27} - S_{18} + S_{28} \\
S_{13} - S_{41} - S_{32} + S_{42} & S_{33} - S43 - S_{34} + S_{44} & S_{35} - S_{45} - S_{36} + S_{46} & S_{37} - S_{47} - S_{38} + S_{48} \\
S_{51} - S_{61} - S_{52} + S_{62} & S_{53} - S_{63} - S_{54} + S_{64} & S_{55} - S_{65} - S_{56} + S_{66} & S_{57} - S_{67} - S_{58} + S_{68} \\
S_{71} - S_{81} - S_{72} + S_{82} & S_{73} - S_{83} - S_{74} + S_{84} & S_{75} - S_{85} - S_{76} + S_{86} & S_{77} - S_{87} - S_{78} + S_{88}
\end{bmatrix}
\tag{1.25}
$$

$$
S_{comm} = \frac{1}{2}
\begin{bmatrix}
S_{11} + S_{21} + S_{12} + S_{22} & S_{13} + S_{23} + S_{14} + S_{24} & S_{15} + S_{25} + S_{16} + S_{26} & S_{17} + S_{27} + S_{18} + S_{28} \\
S_{13} + S_{41} + S_{32} + S_{42} & S_{33} + S43 + S_{34} + S_{44} & S_{35} + S_{45} + S_{36} + S_{46} & S_{37} + S_{47} + S_{38} + S_{48} \\
S_{51} + S_{61} + S_{52} + S_{62} & S_{53} + S_{63} + S_{54} + S_{64} & S_{55} + S_{65} + S_{56} + S_{66} & S_{57} + S_{67} + S_{58} + S_{68} \\
S_{71} + S_{81} + S_{72} + S_{82} & S_{73} + S_{83} + S_{74} + S_{84} & S_{75} + S_{85} + S_{76} + S_{86} & S_{77} + S_{87} + S_{78} + S_{88}
\end{bmatrix}
\tag{1.26}
$$

$$
S_{diff/comm} = \frac{1}{2}
\begin{bmatrix}
S_{11} - S_{21} + S_{12} - S_{22} & S_{13} - S_{23} + S_{14} - S_{24} & S_{15} - S_{25} + S_{16} - S_{26} & S_{17} - S_{27} + S_{18} - S_{28} \\
S_{13} - S_{41} + S_{32} - S_{42} & S_{33} - S43 + S_{34} - S_{44} & S_{35} - S_{45} + S_{36} - S_{46} & S_{37} - S_{47} + S_{38} - S_{48} \\
S_{51} - S_{61} + S_{52} - S_{62} & S_{53} - S_{63} + S_{54} - S_{64} & S_{55} - S_{65} + S_{56} - S_{66} & S_{57} - S_{67} + S_{58} - S_{68} \\
S_{71} - S_{81} + S_{72} - S_{82} & S_{73} - S_{83} + S_{74} - S_{84} & S_{75} - S_{85} + S_{76} - S_{86} & S_{77} - S_{87} + S_{78} - S_{88}
\end{bmatrix}
\tag{1.27}
$$

$$
S_{comm/diff} = \frac{1}{2}
\begin{bmatrix}
S_{11} + S_{21} - S_{12} - S_{22} & S_{13} + S_{23} - S_{14} - S_{24} & S_{15} + S_{25} - S_{16} - S_{26} & S_{17} + S_{27} - S_{18} - S_{28} \\
S_{13} + S_{41} - S_{32} - S_{42} & S_{33} + S43 - S_{34} - S_{44} & S_{35} + S_{45} - S_{36} - S_{46} & S_{37} + S_{47} - S_{38} - S_{48} \\
S_{51} + S_{61} - S_{52} - S_{62} & S_{53} + S_{63} - S_{54} - S_{64} & S_{55} + S_{65} - S_{56} - S_{66} & S_{57} + S_{67} - S_{58} - S_{68} \\
S_{71} + S_{81} - S_{72} - S_{82} & S_{73} + S_{83} - S_{74} - S_{84} & S_{75} + S_{85} - S_{76} - S_{86} & S_{77} + S_{87} - S_{78} - S_{88}
\end{bmatrix}
\tag{1.28}
$$

and moreover, can be calculated according to the expression [15]:

$$S_{mixedmode} = M S_{nodal} M^{-1}, \tag{1.29}$$

where matrix M is defined as:

$$M = \frac{1}{\sqrt{2}} \begin{bmatrix} 1 & -1 & 0 & 0 & 0 & 0 & 0 & 0 \\ 0 & 0 & 1 & -1 & 0 & 0 & 0 & 0 \\ 0 & 0 & 0 & 0 & 1 & -1 & 0 & 0 \\ 0 & 0 & 0 & 0 & 0 & 0 & 1 & -1 \\ 1 & 1 & 0 & 0 & 0 & 0 & 0 & 0 \\ 0 & 0 & 1 & 1 & 0 & 0 & 0 & 0 \\ 0 & 0 & 0 & 0 & 1 & 1 & 0 & 0 \\ 0 & 0 & 0 & 0 & 0 & 0 & 1 & 1 \end{bmatrix}. \tag{1.30}$$

It can be proven, that for the derived mixed-mode matrix, sub-matrices $S_{diff/comm}$ and $S_{comm/diff}$ are equal to zero for a double symmetrical passive network. Thus, the following relations can be shown [135]:

$$\begin{aligned} S_{11} &= S_{22} = S_{33} = S_{44} = S_{55} = S_{66} = S_{77} = S_{88} \\ S_{21} &= S_{43} = S_{65} = S_{87}, \quad S_{31} = S_{42} = S_{75} = S_{86} \\ S_{41} &= S_{32} = S_{76} = S_{85}, \quad S_{51} = S_{62} = S_{73} = S_{84} \\ S_{61} &= S_{52} = S_{74} = S_{84}, \quad S_{71} = S_{53} = S_{64} = S_{28} \\ S_{81} &= S_{54} = S_{63} = S_{72} \end{aligned} \tag{1.31}$$

Furthermore, from the reciprocity we have:

$$S_{xy} = S_{yx} \tag{1.32}$$

and by applying (1.31) and (1.32) in to (1.28) and (1.27) the following relation can be noticed:

$$S_{comm/diff} = S_{diff/comm} = 0. \tag{1.33}$$

1.2. Hybrid Couplers Based on Directly-Connected-Line Topologies

Hybrid couplers are specific type of directional couplers which can be realized by utilizing directly connected transmission lines. Typically, such components provide an equal power split (coupling $C = 3$ dB), which implies that $\alpha = \beta = 1/\sqrt{2}$. In terms of the phase shift between output ports, two topologies can be noticed: quadrature hybrids (branch-line couplers) which provide $90°$ of differential phase and magic-T hybrids (the rat-race couplers) which ensure a $180°$ shift.

A classic 3-dB branch-line coupler is presented in Fig. 1.3a. Such a coupler is composed of directly connected four quarter-wave transmission lines - two of them having characteristic impedance Z_0 and two having a value of $Z_0/\sqrt{2}$. The scattering matrix of the considered hybrid is defined as follows [109]:

$$[S] = -\frac{1}{\sqrt{2}} \begin{bmatrix} 0 & j & 1 & 0 \\ j & 0 & 0 & 1 \\ 1 & 0 & 0 & j \\ 0 & 1 & j & 0 \end{bmatrix}. \tag{1.34}$$

Assuming that, port #1 is an input port, the signal is divided between ports #2 and #3, whereas port #4 is isolated i.e. no power is observed there. The frequency response of the branch-line coupler is shown in Fig. 1.3b.

(a)

(b)
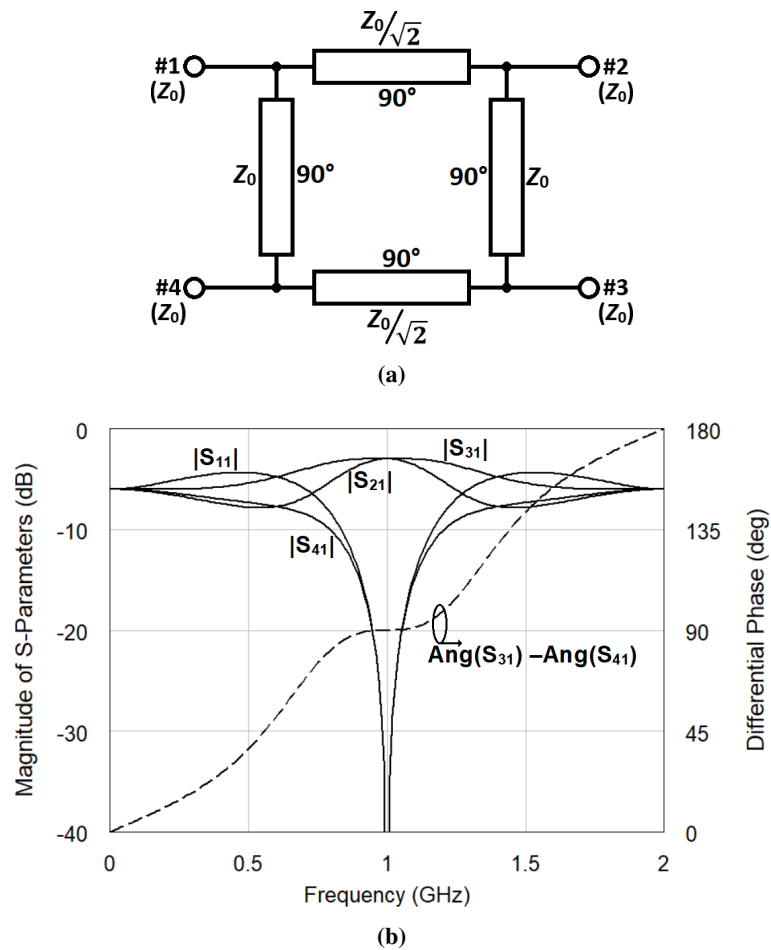
Figure 1.3: The classic 3-dB branch-line coupler (a) and its frequency response, where s-parameters are marked by solid lines and the differential phase is marked by a dashed line (b).

The second hybrid topology, which is the magic-T, can be realized as a rat-race coupler. This structure is presented in Fig. 1.4a. As can be seen, such a coupler is composed of transmission lines with same impedance of $Z_0\sqrt{2}$. Three of these are quarter-wave transmission-lines, whereas the forth

has a 270° electrical length. The scattering matrix which describes the behavior of the coupler at the center frequency, has the following form [109]:

$$[S] = -\frac{j}{\sqrt{2}} \begin{bmatrix} 0 & 1 & 0 & -1 \\ 1 & 0 & 1 & 0 \\ 0 & 1 & 0 & 1 \\ -1 & 0 & 1 & 0 \end{bmatrix}. \tag{1.35}$$

Assuming that the signal is applied into port #1, equal power division is observed between ports #2 and #4, while port #3 is isolated. However, when the coupler is treated as a power combiner, by feeding ports #2 and #3, the sum of both signals is obtained at port #1 and difference is defined at port #4. The frequency response of such a hybrid coupler is presented in Fig. 1.4b.
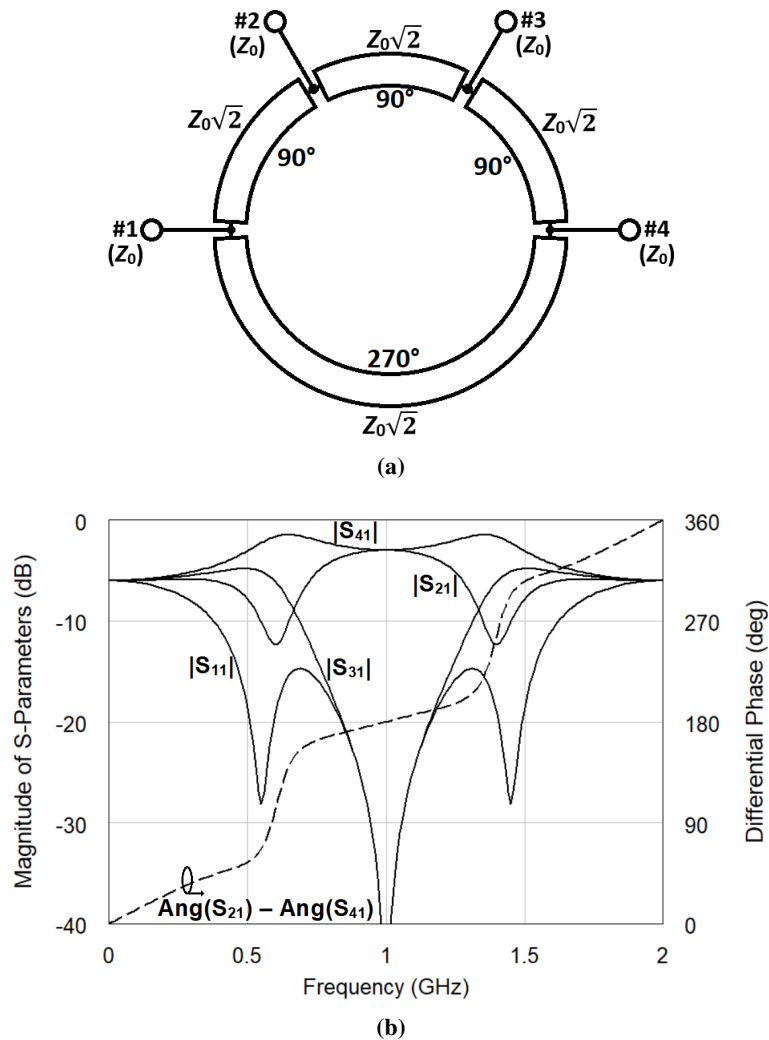
Figure 1.4: The classic 3-dB rat-race coupler (a) and frequency response presenting scattering parameters (solid lines) and the differential phase (dashed line) (b).

R. Smolarz   *Microwave directional couplers' design with the use of planar quasi-TEM transmission line sections.*

1.3. Theoretical Analysis of Coupled-Line Structures

1.3.1. Two-Coupled-Transmission-Line Section

A coupled-line section consisting of transmission-lines in which quasi-TEM waves propagate is a well-known structure in electronics and microwave engineering. Exemplary practical realizations of a two-coupled-transmission-line section (otherwise called a three-conductor coupled-line section) are shown in Fig. 1.5.
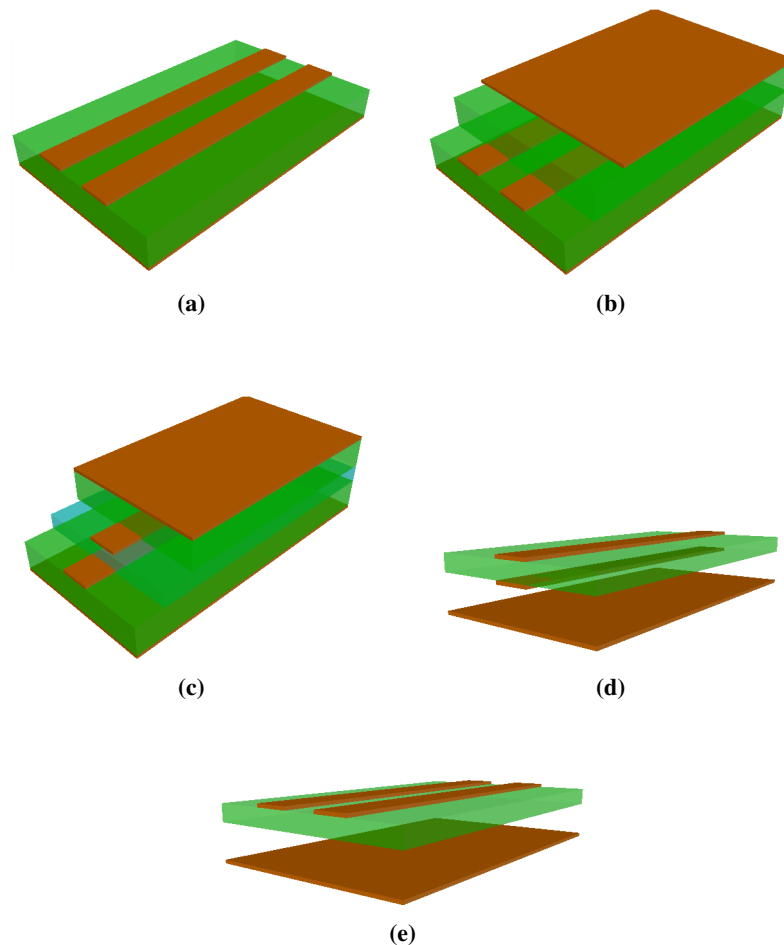
Figure 1.5: Commonly known realizations of two-coupled-line sections: microstrip (a), stripline - edge-wise configuration (b), stripline - broad-side configuration (c), suspended microstrip broadside configuration (d), and suspended microstrip edge-wise configuration (e).

In the two-coupled-line section, three conductors can be distinguish i.e. two signal lines, and the reference conductor which is usually a ground plane which is placed underneath (for a microstrip technique) or on both sides of the signal lines (for a stripline technique). According to electromagnetic field theory, and telegrapher's equations, such a structure can be modeled as a lossy circuit composed of capacitances, inductances, resistances and conductances, which is presented in Fig. 1.6a. It should be noted, that all parameters are defined by the per unit length values. Commonly to simplify calculations,

a lossless coupled-line section is taken into consideration. In such a case, resistances, and conductances are equal to zero i.e. $R_1 = R_2 = G_1 = G_2 = G_m = 0$, which leads to the simpler circuit shown in Fig. 1.6b.
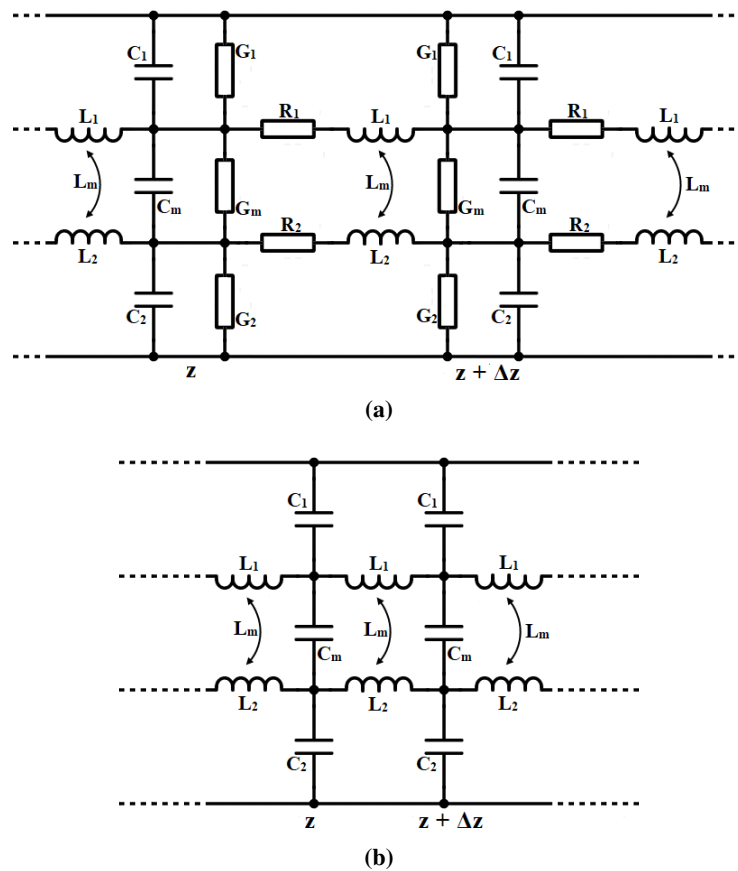
Figure 1.6: Circuit equivalents of a lossy (a), and lossless (b) two-coupled-line section consisting of lumped elements.

For analysis purposes, a microstrip structure presented in Fig. 1.7 has been chosen. For such a technique, a two-coupled-line section can be investigated in terms of self capacitances: C_1 and, C_2 formed between signal conductors and the ground plane, while the mutual capacitance C_m exists between signal lines [96]. For the presented configuration, both signal lines are characterized by electrical charges Q_1, Q_2 and voltages V_1, V_2 for the first and the second transmission lines, respectively.
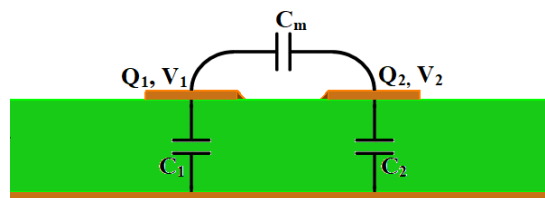
Figure 1.7: Capacitive model of two-coupled-transmission-lines section.

For such a circuit, the relations between voltages, and capacitances can be found by utilizing circuit theory i.e.

$$Q_1 = C_1 V_1 + C_m(V_1 - V_2) = (C_1 + C_m)V_1 - C_m V_2 \tag{1.36}$$

$$Q_2 = C_2 V_2 + C_m(V_2 - V_1) = -C_m V_1 + (C_2 + C_m)V_2. \tag{1.37}$$

Having derived relations, the capacitance matrices can be found as

$$[C] = \begin{bmatrix} C_{11} & C_{12} \\ C_{21} & C_{22} \end{bmatrix} = \begin{bmatrix} C_1 + C_m & -C_m \\ -C_m & C_2 + C_m \end{bmatrix}. \tag{1.38}$$

Furthermore, by using the calculated capacitance matrix $[C]$, an inductance matrix $[L]$ can be derived according to the formula [154]

$$[L] = \mu_0 \epsilon_0 [C_0]^{-1} \tag{1.39}$$

where μ_0 is free space magnetic permeability, ε_0 is free space electric permittivity, and C_0 is a capacitive matrix found for two-coupled-transmission-lines in homogeneous substrate characterized by permittivity equal to unity (free space assumption).

A) A Symmetric Coupled-Line Section

Due to the symmetry of a structure, parameters and response can be calculated utilizing odd-even mode analysis. A circuit consisting of capacitances which is the equivalent of a coupled-lines section is shown in Fig. 1.8 [96]. In the Fig. 1.8a the even mode network is presented, while in the Fig. 1.8b the odd mode equivalent is shown.
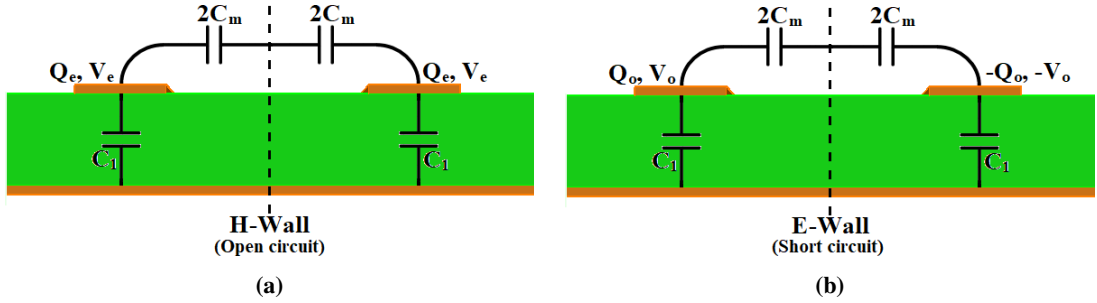
Figure 1.8: Equivalent circuits for symmetric coupled-lines section for even (a), and odd (b) modes.

According to the presented schematics, capacitances for each of the modes can be defined as follows:

$$C_{0e} = C_1 \tag{1.40}$$

$$C_{0o} = C_1 + 2C_m. \tag{1.41}$$

The modal impedances for a homogeneous medium can be calculated as follows [43]:

$$Z_{0e} = \frac{1}{v_{pe}C_e} = \frac{\omega}{\beta_e C_e} \tag{1.42}$$

$$Z_{0o} = \frac{1}{v_{po}C_o} = \frac{\omega}{\beta_o C_o} \tag{1.43}$$

where Z_{0e}, v_{pe}, β_e are: impedance, phase velocity and phase constant of the even mode, respectively, while Z_{0o}, v_{po}, β_o are related to the odd mode. Moreover, for the homogeneous substrate, phase velocity for even, and odd modes are equal:

$$v_{pe} = v_{po} = \frac{c}{\sqrt{\varepsilon_r}}. \tag{1.44}$$

For an inhomogeneous medium, the odd and even impedances can be found by using [43]:

$$Z_{0e} = \frac{1}{c\sqrt{C_e C_{0e}}} \tag{1.45}$$

$$Z_{0o} = \frac{1}{c\sqrt{C_o C_{0o}}} \tag{1.46}$$

where c is the speed of light, and C_e, C_o are even, and odd-mode per-unit-length capacitances are defined as:

$$C_e = C_{0e} \varepsilon_{ef(e)} \tag{1.47}$$

$$C_o = C_{0o} \varepsilon_{ef(o)}. \tag{1.48}$$

where $\varepsilon_{ef(e)}$, and $\varepsilon_{ef(o)}$ are the electrical permittivities for the even, and odd modes, respectively. In general, with even and odd impedances, the resulting impedance of symmetric coupled-lines section can be found [109]

$$Z_0 = \sqrt{Z_{0e} Z_{0o}}. \tag{1.49}$$

The calculated impedances can be used to define general coupling coefficient k:

$$k = \frac{Z_{0e} - Z_{0o}}{Z_{0e} + Z_{0o}} \tag{1.50}$$

and combining (1.49) with (1.50) the following relations can be found:

$$Z_{0e} = Z_0 \sqrt{\frac{1+k}{1-k}} \tag{1.51}$$

$$Z_{0o} = Z_0 \sqrt{\frac{1-k}{1+k}}. \tag{1.52}$$

Furthermore, modal impedances can be calculated in terms of capacitive and inductive parameters as has been shown in [96]:

$$Z_{0e} = \sqrt{\frac{L_1 + L_m}{C_1 - C_m}} \tag{1.53}$$

$$Z_{0o} = \sqrt{\frac{L_1 - L_m}{C_1 + C_m}}. \tag{1.54}$$

B) An Asymmetric Coupled-Line Section

A 3D view of asymmetric coupled-lines is presented in Fig. 1.9. Such a structure is composed of two different-width transmission-lines realized with a microstrip technique and therefore, it can be analyzed by using circuit presented in the Fig. 1.7. Due to the fact, that strips have different geometry, the impedances and therefore the capacitances are not equal i.e. $C_1 \neq C_2$. It can be noticed, that values of capacitances can be derived from the capacitance matrix $[C]$ according to relations:

$$C_1 = C_{11} - C_m \tag{1.55}$$

$$C_2 = C_{22} - C_m, \tag{1.56}$$

Assuming homogeneous medium in which dielectric permittivity $\varepsilon = 1$, the values of capacitance matrix are respectively:

$$C_{11} = \frac{1}{cZ_{L1}} \tag{1.57}$$

$$C_{22} = \frac{1}{cZ_{L2}} \tag{1.58}$$

$$C_m = k\sqrt{C_{11}C_{22}} \tag{1.59}$$

where Z_{L1} and Z_{L2} are transmission-lines impedances, c is the speed of light in free space, and k is the coupling factor between strips. The capacitive, and inductive coupling coefficients can be also derived [96], [112]:

$$k_C = \frac{C_m}{\sqrt{C_1 C_2}} \tag{1.60}$$

$$k_L = \frac{L_m}{\sqrt{L_1 L_2}}. \tag{1.61}$$
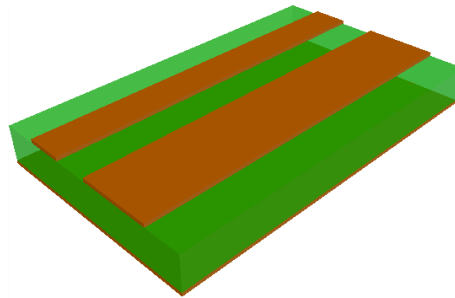
Figure 1.9: A 3D view of asymmetric coupled-transmission-lines realized in the microstrip technique.

1.3.2. Four-Coupled-Transmission-Line Section

A multi-conductor coupled-line section will be explained with the example of a six-conductor structure in which four conductors are treated as signal lines and two are utilized as ground planes. It can be noticed, that such a situation can be easily implemented in a stripline or buried microstrip techniques. Such a structure is presented in 1.10, whereas in 1.11 the equivalent circuit consisting of capacitances is presented. The mentioned circuit can be divided in to four equivalent circuits which are derived for four modes: even-differential, odd-differential, even-common and odd-common [135]. Such schematics are shown in 1.12.
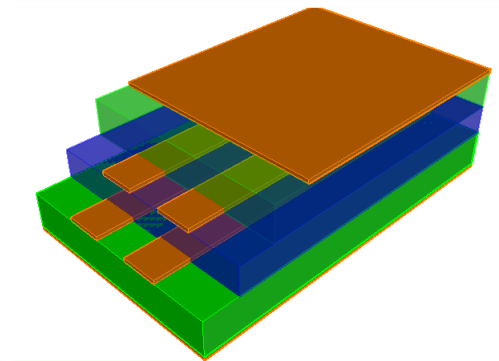
Figure 1.10: A 3D model of a four-coupled-line section designed using the stripline technique.
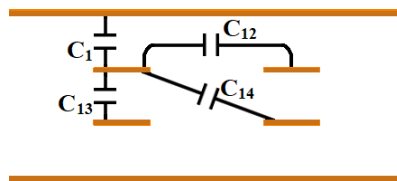
Figure 1.11: Capacitive schematic of a differentially-fed directional coupler.
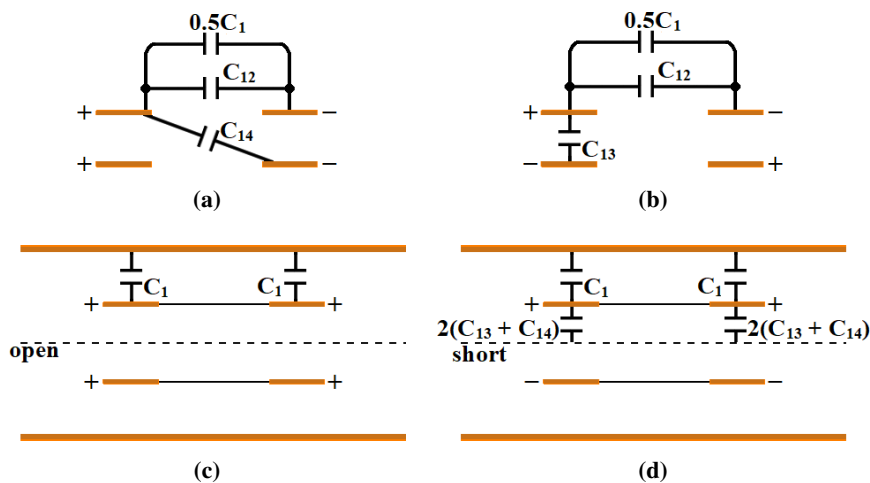
Figure 1.12: The equivalent capacitive circuits for a differentially excited structure with even-differential (a), odd-differential (b), even-common (c) and odd-common (d) modes.

It has to be mentioned, that the considered structure is fully symmetrical, thus all self capacitances (C_1) formed between the signal lines, and the ground planes are equal. All denoted parameters are per-unit-length values, and the following relations define such a structure [135]:

$$C_{e(diff)} = 0.5C_1 + \mid C_{12} \mid + \mid C_{14} \mid \tag{1.62}$$

$$C_{o(diff)} = 0.5C_1 + \mid C_{12} \mid + \mid C_{13} \mid \tag{1.63}$$

$$C_{e(comm)} = 2C_1 \tag{1.64}$$

$$C_{o(comm)} = 2C_1 + 4 \mid C_{13} \mid + 4 \mid C_{14} \mid \tag{1.65}$$

$$C_1 = C_{11} - \mid C_{12} \mid - \mid C_{13} \mid - \mid C_{14} \mid \tag{1.66}$$

where $C_{o(diff)}$, $C_{e(diff)}$ are capacitances defined for the odd-differential, and the even-differential mode, while $C_{o(comm)}$, $C_{e(comm)}$ are for the odd-common, and the even-common modes.

For homogeneous substrates, the modal impedances for each of the modes can be found by calculating the expression:

$$Z_x = (vC_x)^{-1} \tag{1.67}$$

where *x* is the index defining each mode: odd, even, differential, common.

1.4. Compensation Methods Utilized in Coupled-Line Sections

In the theoretical model of coupled-line sections, the problem related to high return losses or small directivity does not exist. However, from a practical point of view, such issues can be observed due to imperfection of used medium. In Fig. 1.13 the scattering parameters of a 3-dB coupled-line section are presented which has been designed with the microstrip technique consisting of a substrate of height $h = 1$ mm, and dielectric permittivity of $\varepsilon_r = 3.38$. As can be noticed, values of isolation, and return losses increase together with frequency. Such behavior is a crucial issue, especially in broadband applications.

In general, the coupled-lines section has to be considered as either a symmetric or an asymmetric structure. In the first, the even e and odd o modes can be defined, while in the second - the two modes are called c and π. The main idea of compensation methods is related to the equalization of phase velocities (in symmetric structures) or coupling coefficients (in asymmetric ones). Such an approach can be obtained using strategies which have been proposed in the literature:

1. the proper arrangement of a stack-up, introducing some specific compensation layers [147], [62],[40], [117],[120], [113],[116],[52],[157],[49]

2. additional lumped or quasi-lumped elements connected to a coupled-line section [36], [91],[31],[74],[20],[78],[98],[105],[16],[161],[7],[17]

3. periodic modification of a coupled-lines section [108],[146],[39],[53]

4. other methods such as the utilization of delay lines [22], stepped-impedance sections [97] or corrugated ground planes [92].
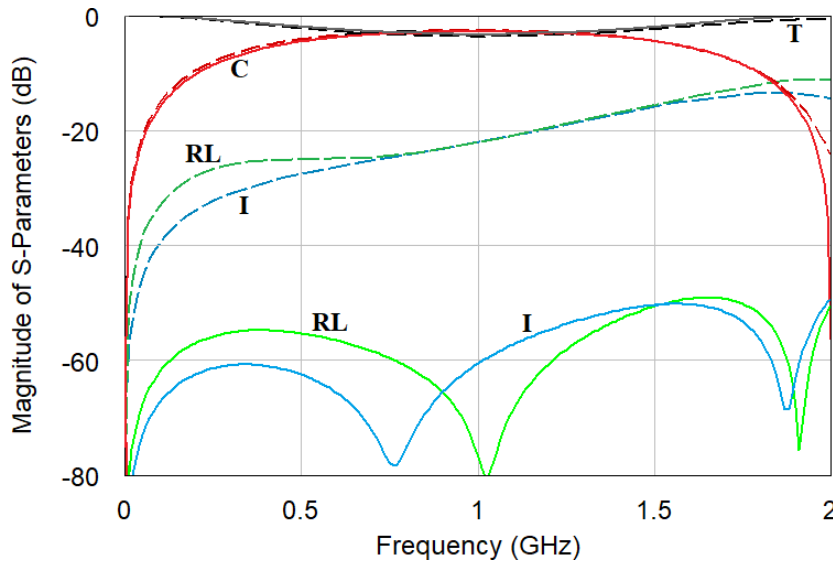
Figure 1.13: Graph presenting the effects of compensation of a 3-dB coupled-line section. RL - return losses, C - coupling, I - isolation, T - transmission.

In [48] the authors conducted comprehensive studies of compensation methods for different relations between inductive and capacitive coupling coefficients, where a novel method based on the mentioned techniques was introduced. In general, the coupled-line section can be divided in to *n*-subsection circuits. Moreover, such subsections are characterized by inductive matrices $[C]$ and $[L]$. Basically, compensation can be achieved by utilizing additional capacitances connected in a proper manner between the coupled-lines by mutual capacitance C_m, and ground C_1 and C_2. Three different cases of coupled-line geometry can be distinguished.

A) Symmetric Coupled-Line Section $(k_L > k_C)$

The simplest form of a symmetric coupled-line structure can be realized as an edgewise configuration using the microstrip technique, in which inductive coupling coefficient k_L is greater than the capacitive coefficient k_C by definition. It is intuitive that, in cases where $k_L > k_C$, the mutual capacitance has to be increased to compensate for the coupling coefficient. As has been mentioned in the previous Section 1.3.1, the capacitive model of the coupled-line section assumes some relation between capacitances. Thus, by changing the value of the capacitance C_m the overall response of the coupler can be improved in terms of return losses and isolation. Therefore, a method which is based on an iterative procedure can be utilized [156]. However, in [48] the authors proposed a method which utilized additional inductance L_k,

and capacitance C_k. A schematic of the proposed solution is presented in Fig. 1.14 where the mentioned elements are placed periodically between coupled-line subsections.
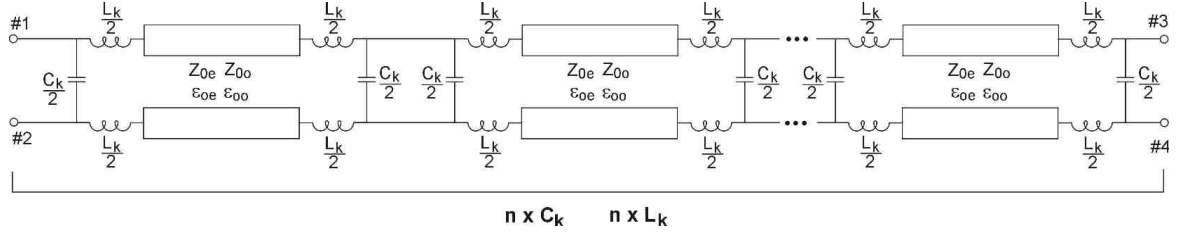
Figure 1.14: Schematic diagram of the symmetric coupled-line section compensated with n equally spaced lumped compensating capacitances C_k and inductances L_k. [48]. (Copyright © 2011, IEEE)

Such an approach enables the design of an ideal coupled-line section having arbitrarily, chosen coupling and particularly a dielectric structure, the condition which is met is:

$$Z_{0e}Z_{0o} = Z_0^2. \tag{1.68}$$

For such a relation, modal capacitances can be found in which characteristic impedances, and odd-even effective permittivities are used i.e.:

$$C_e = \frac{\sqrt{\varepsilon_{eff(e)}}}{Z_{0e}c} \tag{1.69}$$

$$C_o = \frac{\sqrt{\varepsilon_{eff(o)}}}{Z_{0o}c} \tag{1.70}$$

Whereas, self capacitance C_1 and the mutual C_m which are per unit length values can be found as follows:

$$C_1 = C_e \tag{1.71}$$

$$C_m = \frac{C_o - C_e}{2} \tag{1.72}$$

For the compensated case, the coupling coefficients k_C and k_L can be calculated as

$$k_L = \frac{L_m}{L_{11} + L_d} \tag{1.73}$$

$$k_C = \frac{C_m}{C_{11} + C_d} \tag{1.74}$$

where L_d and C_d are correcting per unit length inductance and capacitance values. With 1.73 and 1.74 we can get:

$$\frac{L_m}{L_{11} + Ld} = \frac{C_m + C_d}{C_{11} + C_d} \tag{1.75}$$

$$\frac{L_{11} + L_d}{C_{11} + C_d} = Z_0^2. \tag{1.76}$$

By transforming the above equations, the correcting inductance and capacitance can be calculated as follows:

$$L_d = Z_0^2 \left(C_{11} + \frac{L_m}{Z_0^2} - C_m \right) - L_{11} \tag{1.77}$$

$$C_d = \frac{L_m}{Z_0^2} - C_m. \tag{1.78}$$

As has been shown in previous research [156], the compensating elements per unit length can be realized as lumped inductors and capacitors periodically placed along the coupled-line section. The values of compensating elements can be calculated as follows:

$$L_k = \frac{L_d l}{n} \tag{1.79}$$

$$C_k = \frac{C_d l}{n} \tag{1.80}$$

B) Asymmetric Coupled-Line Section $(k_L > k_C)$

Figure 1.15 presents a concept view of a compensated asymmetric section, in which coupling coefficients are not equal i.e. $k_L > k_C$. For such a geometry, the initial inductive and capacitive matrices of the coupled-line subsection are denoted as $[L]^a$ and $[C]^a$. Furthermore, the additional assumption related to the coupling coefficients is taken into account as $k_L > k > k_C$, where k is a required, resultant coupling coefficient.

It can be seen, that for an ideal coupled-line section, the following set of equations can be found:

$$\begin{cases} Z_{T1}^2 = \frac{L_{11}^a}{C_{11}^a} \\ Z_{T2}^2 = \frac{L_{22}^a}{C_{22}^a} \\ k_L = \frac{L_m^a}{\sqrt{L_{11}^a L_{22}^a}} = k \\ k_C = \frac{C_m^a}{\sqrt{C_{11}^a C_{22}^a}} = k \end{cases} \tag{1.81}$$

Due to the assumed inequality of coupling coefficients, additional correcting parameters are introduced L_{11}^d, L_{22}^d, L_m^d, and C_m^d. Moreover, capacitance C_m is understood as $-C_{12}$ of the corresponding capacitive matrix obtained for the considered structure. Therefore, equations for the compensated structure can be derived from the following formulas:

$$\begin{cases} Z_{T1}^2 = \frac{L_{11}^a + L_{11}^d}{C_{11}^a + C_m^d} \\ Z_{T2}^2 = \frac{L_{22}^a + L_{22}^d}{C_{22}^a + C_m^d} \\ k_L = \frac{L_m^a + L_m^d}{\sqrt{\left(L_{11}^a + L_{11}^d\right)\left(L_{22}^a + L_{22}^d\right)}} = k \\ k_C = \frac{C_m^a + C_m^d}{\sqrt{\left(C_{11}^a + C_{11}^d\right)\left(C_{22}^a + C_{22}^d\right)}} = k \end{cases} \tag{1.82}$$

which after some transformations, give:

$$L_{11}^d = Z_{T1}^2 \left(C_{11}^a + C_m^d \right) - L_{11}^a \tag{1.83}$$

$$L_{22}^d = Z_{T2}^2 \left(C_{22}^a + C_m^d \right) - L_{22}^a \tag{1.84}$$

$$L_m^d = k \sqrt{\left(L_{11}^a + L_{11}^d \right) \left(L_{22}^a + L_{22}^d \right)} - L_m^a \tag{1.85}$$

$$C_m^d = \frac{- \left(k^2 C_{22}^a + k^2 C_{11}^a - 2 C_m \right) \pm \sqrt{\Delta}}{2 \left(k^2 - 1 \right)} \tag{1.86}$$

where $\Delta = \left(k^2 C_{22}^a + k^2 C_{11}^a - 2 C_m^a \right)^2 - 4 \left(k^2 - 1 \right) \left(k^2 C_{11}^a C_{22}^a - C_m^a{}^2 \right)$.
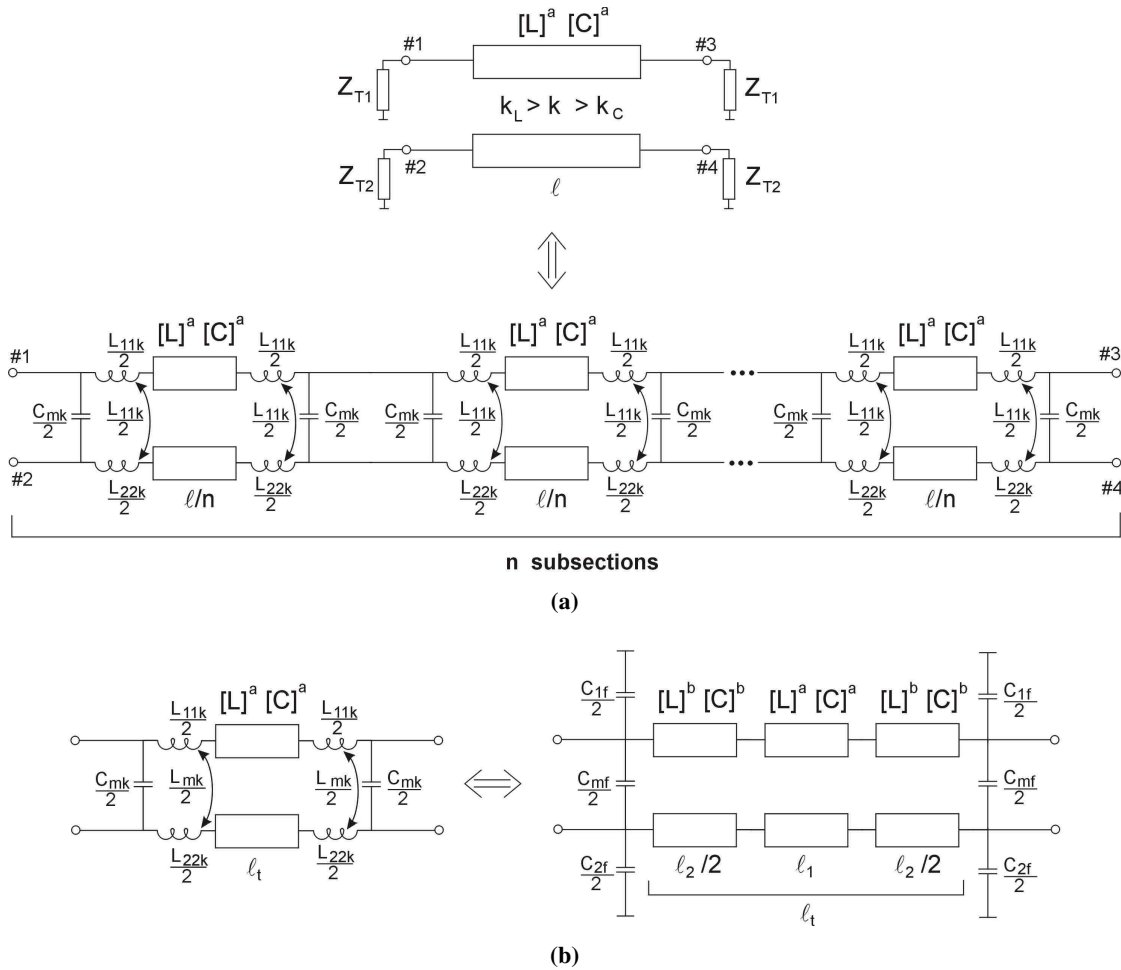
Figure 1.15: Compensated section of asymmetric coupled lines divided into n subsections (a), and equivalent circuit of a single compensated subsection. [48]. (Copyright © 2011, IEEE)

Additional mutual capacitance, calculated from equation (1.86) needs to have a positive value. Thus, only such values are considered during the following calculations. Since the coupling k is arbitrarily chosen between k_L and k_C, the calculated value of L_m^d can be either positive or negative. Thus, to find a physical realization regardless of L_m^d, it is necessary to divide the considered subsection in to two

subcircuits which in general are defined by L_{11k}, L_{22k}, and L_{mk}. To derive the inductance matrix $[L]^b$ of the compensating section, the following equations can be used:

$$L_{11}^b = \frac{\left(L_{11}^a + L_{11}^d\right) l_t - L_{11}^a l_1}{l_2} \tag{1.87}$$

$$L_{22}^b = \frac{\left(L_{22}^a + L_{22}^d\right) l_t - L_{22}^a l_1}{l_2} \tag{1.88}$$

$$L_m^b = \frac{\left(L_m^a + L_m^d\right) l_t - L_m^a l_1}{l_2} \tag{1.89}$$

where l_1 is the length of the shortened coupled-line section defined by $[L]^a$, and $[C]^a$, whereas l_2 is the length of the compensating coupled-lines section described by $[L]^b$, and $[C]^b$ matrices. Moreover, the sum of l_1 and l_2 gives the initial length of the coupled-lines section described by the $[L]^a$, and $[C]^a$, which is denoted as l_t.

Defining parameters of the compensating section is one of the most crucial steps in the design process. First, the compensating inductive matrix $[L]^b$ has to be found. For such a step, numerical software such as Linpar [28], can be used. Having, $[L]^b$ the coupling matrix $[C]^b$ can easily be calculated. Shortening the main section described by $[L]^a$ and $[C]^a$ has decreased the total capacitance, which has been increased by the capacitance of the compensating section. Nonetheless, the balance of the total capacitance is positive, thus some additional capacitance must be found according to

$$[C]^f = \left([C]^a + [C]^d\right) l_t - [C]^a l_1 - [C]^b l_2 \tag{1.90}$$

where $[C]^d$ is the compensating matrix which can be found by using 1.86, and it has the form:

$$[C]^d = \begin{bmatrix} C_m^d & -C_m^d \\ -C_m^d & C_m^d \end{bmatrix}. \tag{1.91}$$

The compensating capacitances defined by $[C]^f$ can be realized by lumped or quasi-lumped elements connected to the coupled-line sections. Values of such elements can be found as follows:

$$C_{1f} = C_{11}^f + C_{12}^f \tag{1.92}$$

$$C_{2f} = C_{22}^f + C_{12}^f \tag{1.93}$$

$$C_{mf} = -C_{12}^f. \tag{1.94}$$

C) Asymmetric Coupled-Line Section $(k_L < k_C)$

It is intuitive, that in the case where a capacitive coupling coefficient k_C is greater than an inductive one k_L, the additional elements with a capacitive character (C_{11}^d, C_{22}^d, C_m^d, L_m^d) have to be added, where

C_m^d has a negative value. However, such an approach is not applicable in physical structures. Thus, by fulfilling condition $k = k_L$, three variables can be considered C_{11}^d, C_{22}^d, and positive C_m^d.
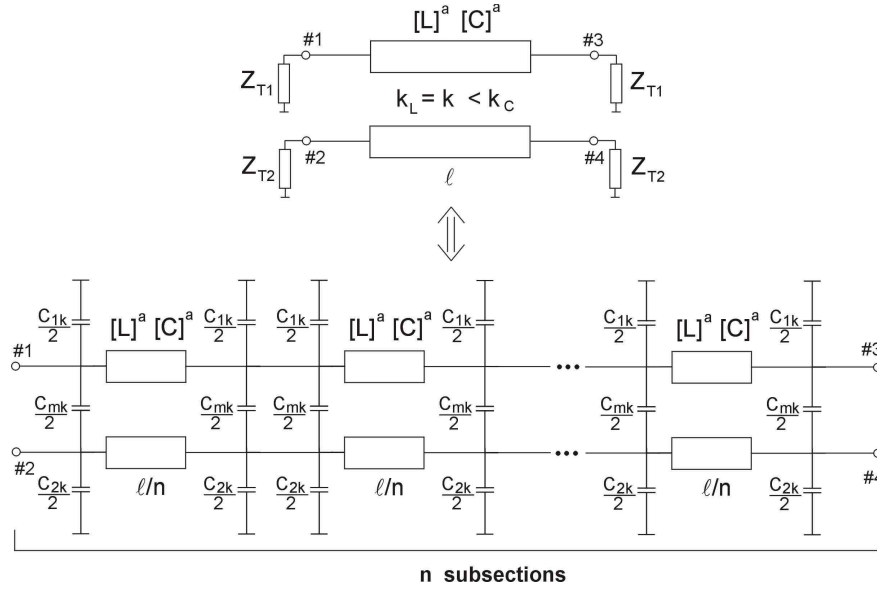
Figure 1.16: Generic schematic of the compensated section of asymmetric coupled lines divided into n subsections in which $k_L < k_C$. [48]. (Copyright © 2011, IEEE)

First, the following conditions have to be fulfilled during the coupled-line section design:

$$k_L = k < k_C \tag{1.95}$$

$$Z_{T1}, Z_{T2} > Z_0 \tag{1.96}$$

$$Z_{T1} Z_{T2} > \frac{k_C}{k_L} Z_0^2 \tag{1.97}$$

where Z_0 is the termination impedance of both lines of the designed coupled-line section. It should be noted, that if conditions (1.95) and (1.96) are meet, then all compensating capacitances have positive values, and thus the structure can be fabricated. If $Z_{T1} = Z_{T2}$, then (1.97) can be transformed in to:

$$Z_{T1,2} = \sqrt{\frac{k_C}{k_L}} Z_0. \tag{1.98}$$

When having a coupled section designed according to the mentioned circumstances ($k = k_L$), and meeting equations (1.96) and (1.97), the compensating capacitances can be calculated as follows:

$$C_1^d = \frac{L_{11}^a}{Z_0^a} - C_{11}^a - \frac{k}{Z_0^2} \sqrt{L_{11}^a L_{22}^a} + C_m^a \tag{1.99}$$

$$C_2^d = \frac{L_{22}^a}{Z_0^a} - C_{22}^a - \frac{k}{Z_0^2} \sqrt{L_{11}^a L_{22}^a} + C_m^a \tag{1.100}$$

$$C_m^d = \frac{k}{Z_0^2}\sqrt{L_{11}^a L_{22}^a} - C_m^a. \tag{1.101}$$

In Fig. 1.16 the general schematic of the compensated coupled-line section is presented. Having values of capacitances calculated according to equations (1.99) - (1.101), the quasi-lumped compensating capacitors C_{1k}, C_{2k}, and C_{mk} can be found by using equation (1.80).

1.5. Aim and Organization of the Thesis

The thesis presents design methodologies, analysis and results related to the directional couplers utilized in planar PCB and monolithic technologies. To design high-performance component, the main issues have been collected, and formulated into the following theses:

1. The equalization of inductive and capacitive coupling coefficients in asymmetric planar low-loss directional couplers is possible and can improve directivity.

2. The equalization of inductive and capacitive coupling coefficients increase directivity in monolithic directional couplers.

3. The modification of classic directional coupler topologies allows impedance transformation in broader operational bandwidths and increase impedance transformation ratio.

4. High-performance directional couplers may be utilized as components of radio frequency circuits designed using the monolithic technology.

Each of the presented goals is discussed in four chapters showing detailed analysis, and experimental results of the designed solutions.

Chapter 2 is fully devoted to the improvement of broadband coupled-line directional couplers by utilizing a proper compensation methodology based on additional compensating elements or by a proper substrate stack-up arrangement. The chapter includes two main sections. In the first, compensation methods utilized in single-ended low-loss planar and monolithic directional couplers are discussed. In the second section, the improvement of the electrical parameters of differentially-fed couplers is studied.

In Chapter 3, impedance transforming directional couplers are presented. The chapter begins with a brief introduction to a simple impedance transforming coupled-line section. In the next sections, the author proposes novel approaches and modifications of known topologies such as rat-race couplers and tandem configurations consisting of coupled-line sections. It has been proven that rat-race topology can be adopted as an impedance-transforming component with a theoretically unlimited impedance-transforming ratio. Moreover, in such a topology, the operational bandwidth is obviously narrow. However, it has been shown that the bandwidth can be enhanced by utilizing additional coupled-line sections connected to proper ports of the classic ring structure. Such an idea of broadband impedance-transforming rat-race coupler has been also utilized using the stripline technique to verify the possibility of its implementation as a low-loss component. Furthermore, a tandem-connected directional

coupler is also proposed. It is proven that in such a structure, the impedance-transforming ratio can be significantly increased in comparison to other couplers composed of coupled-line sections. Moreover, its bandwidth is comparable to the classic tandem couplers.

Chapter 4 is focused on applications of high-performance directional couplers in MMIC technology based on gallium arsenide. Three complex circuit designs are discussed. The first is a 24 GHz monolithic sensor which is intended for measurements of the dielectric permittivities of materials. In the design, miniaturized branch-line couplers proposed by the author are utilized. The second design is a balanced amplifier consisting of differentially-fed miniaturized branch-line couplers proposed by the author. Finally, a FMCW radars' front-end operating in the automotive frequency band has been presented in which a compensated directional coupler composed of a three-coupled-line section is utilized.

The dissertation ends with Chapter 5, in which the main conclusions are presented together with further research directions.

2. Improved Broadband Directional Couplers

In this chapter, improved broadband directional couplers composed of coupled-line sections are presented. Section 2.1 focuses on low-loss single-ended directional couplers designed with the suspended microstrip technique. Two topologies are proposed by the author and investigated: an asymmetric two-coupled-line section, and a four-strip Lange structure. Section 2.2 focuses on compensation methods utilized in single-ended monolithic directional couplers. The author presents a comprehensive proof-of-application of compensation method applied in different coupler topologies based on the gallium arsenide PH25 process, provided by *United Monolithic Semiconductors* (UMS). Section 2.3 describes compensation methods utilized in differentially excited directional couplers based on homogeneous and inhomogeneous substrate stratification.

In this chapter, the author cites his investigation on improved broadband compensated directional couplers published in [126], [122], [65], [44],[128], [45].

2.1. Coupling Coefficient Equalization Methods in Planar Single-Ended Low-Loss Directional Couplers

In this section, compensation methods utilized in single-ended low-loss directional couplers designed with suspended microstrip technique are presented. The considered cases are characterized by an inequality of capacitive and inductive coupling coefficients. The author shows, that compensation elements such as open stubs and a proper stack-up arrangement can equalize the mentioned coefficients in low-loss structures and therefore, the entire electrical performance of a coupler can be improved. The section is divided into two subsections. In the first, the author proposes a compensation methodology, which can be utilized in low-loss, asymmetric two-coupled-line directional couplers. In the second, low-loss four-coupled-line section in the Lange topology is presented.

2.1.1. Low-Loss Asymmetric Coupled-Line Directional Couplers

In Section 1.4, the introduction to compensation methods based on equalization of coupling coefficients is presented. It has been shown that for asymmetric coupled-line geometry, the coupling coefficients k_C and k_L can be different, thus the entire performance of the directional coupler can deteriorate. The return losses and isolation in such a coupler can be significantly improved by utilizing additional capacitances periodically placed in the coupled-line section [48].

One of the most crucial issues in microwave engineering is related to the reduction of total losses in components. In the case of passive elements fabricated using microstrip and stripline techniques, some solutions are presented in the literature [147], [87], [11], [53]. To obtain good electrical performance in stripline structures, an air layer is commonly introduced. However, the suspended microstrip technique can be also utilized, and moreover it can be used for high-power applications.
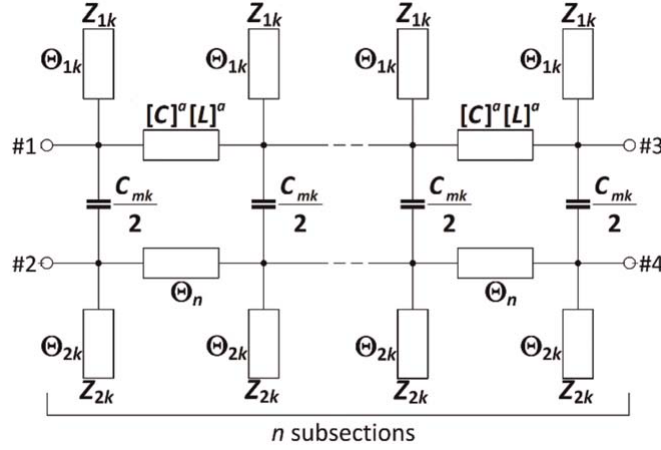
Figure 2.1: Circuit diagram presenting compensated coupled-line directional coupler in which additional open stubs are utilized to improve electrical performance [122]. (Copyright © 2017, Wiley)

Let us assume, that the relation $k_C < k_L$ holds for a considered asymmetric geometry. Thus, the capacitive compensation method presented in Section 1.4 can be implemented to equalize both coupling coefficients. However, additional capacitances in the form of lumped elements are quite problematic in the fabrication process, especially in the suspended microstrip technique. Quasi-lumped elements can occupy large area, which makes the design process much more difficult particularly during electromagnetic simulations. Thus, such elements can be replaced by distributed elements such as open-stubs structures, which has been proposed by the author [122]. A compensated low-loss directional coupler is presented in Fig. 2.1. With reference to Fig. 1.16 it can be noticed that, capacitances C_{1k} and C_{2k} are replaced by stubs. Electrical parameters of such compensating elements can be easily derived by well-known equations for open-ended transmission-lines as:

$$Z_{in} = -jZ_{1k,2k} \cot \Theta_{1k,2k} \tag{2.1}$$

$$Z_{in} = -j \frac{1}{2\pi f_0 C_{1k,2k}} \tag{2.2}$$

where f_0 is the operational frequency, Z_{in} is the input impedance of the open-ended stub and is directly related to capacitances C_{1k}, C_{2k}. Having such equations, the characteristic impedances and electrical lengths of compensating stubs can be derived from the following:

$$Z_{1k,2k} = \frac{1}{2\pi f_0 C_{1k,2k} \cot \Theta_{1k,2k}} \tag{2.3}$$

$$\Theta_{1k,2k} = \arctan 2\pi f_0 C_{1k,2k} Z_{1k,2k}. \tag{2.4}$$

Two low-loss directional couplers operating at the center frequencies 890 MHz (*Coupler no. 1*) and 1.1 GHz (*Coupler no. 2*) have been developed using the suspended microstrip technique. A cross-sectional view of the utilized susbstrate composition for both components is presented in Fig. 2.2, where $h_1 = 0.3$ mm, $h_2 = 1.35$ mm, $\varepsilon_{r1} = 3.38$. Due to the fact, that the laminate is suspended over the ground plane, ε_{r2} is equal to unity.
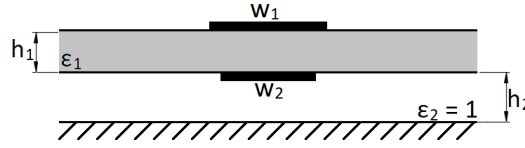
Figure 2.2: Cross-sectional view of suspended microstrip structure utilized in low-loss compensated coupled-line directional couplers. (Copyright © 2017, Wiley)

For such a stratification, the capacitive coefficient is greater than the inductive one. Therefore, the proposed method was used, in which the overall coupling k is equal to inductive one $k_L = 0.75$, whereas the capacitive coupling coefficient $k_C = 0.89$. For such values, the terminating impedances were found wich are $Z_{T1} = 55.64$ Ω, and $Z_{T2} = 56.19$ Ω what corresponds to physical line widths of $w_1 = 1.3$ mm, $w_2 = 1.1$ mm, and an offset between them equal to $s = 0.1$ mm. The parameters of calculated compensation elements for both coupled-line directional couplers are presented in Table 2.1. The designed couplers are divided in to five subsections which have equal electrical lengths of 18 °.

Table 2.1: Electrical parameters of compensating elements utilized in low-loss directional couplers operating at 890 MHz and 1.1 GHz respectivelly. The compensated coupled-lines section is characterized by inductive and capacitive coupling coefficients $k_L = 0.73$, $k_C = 0.89$. Moreover, impedances of terminating lines are $Z_{T1} = 55.6$ Ω and $Z_{T2} = 56.2$ Ω.

Parameter	Coupler no. 1 (890 MHz)	Coupler no. 2 (1.1 GHz)
C_{1k} (pF)	0.174	0.138
Z_{1k} (Ω)	88.2	96.1
Θ_{1k} (°)	4.89	5.31
C_{2k} (pF)	0.206	0.185
Z_{2k} (Ω)	83.5	88.3
Θ_{2k} (°)	5.48	6.45
C_m (pF)	0.044	0.044

The layout of the first designed directional coupler operating at the center frequency of 890 MHz is presented in 2.4a; the second, operating at 1.1 GHz, is shown in 2.4b. As can be observed, the difference relies on the placement and number of compensating elements. In the first case, each of the coupled-line subsections has the same number of compensating open-ended stubs which have the same length for each strip. In the second coupler, two additional compensating elements are added which are connected to the center of the directional coupler. Both elements facilitate the final tuning of the structure, and have values of $C_{q1} = 0.088$ pF, $C_{q2} = 0.129$ pF. To compensate the resulting discontinuity between the coupled-line

sections and the 50 Ω signal lines, lumped capacitances C_i, and C_j have been added. The calculated values for directional coupler no. 1 are $C_i = 0.328$ pF, $C_j = 0.331$ pF, whereas for no. 2, the values are $C_i = 0.193$ pF, and $C_j = 0.238$ pF.
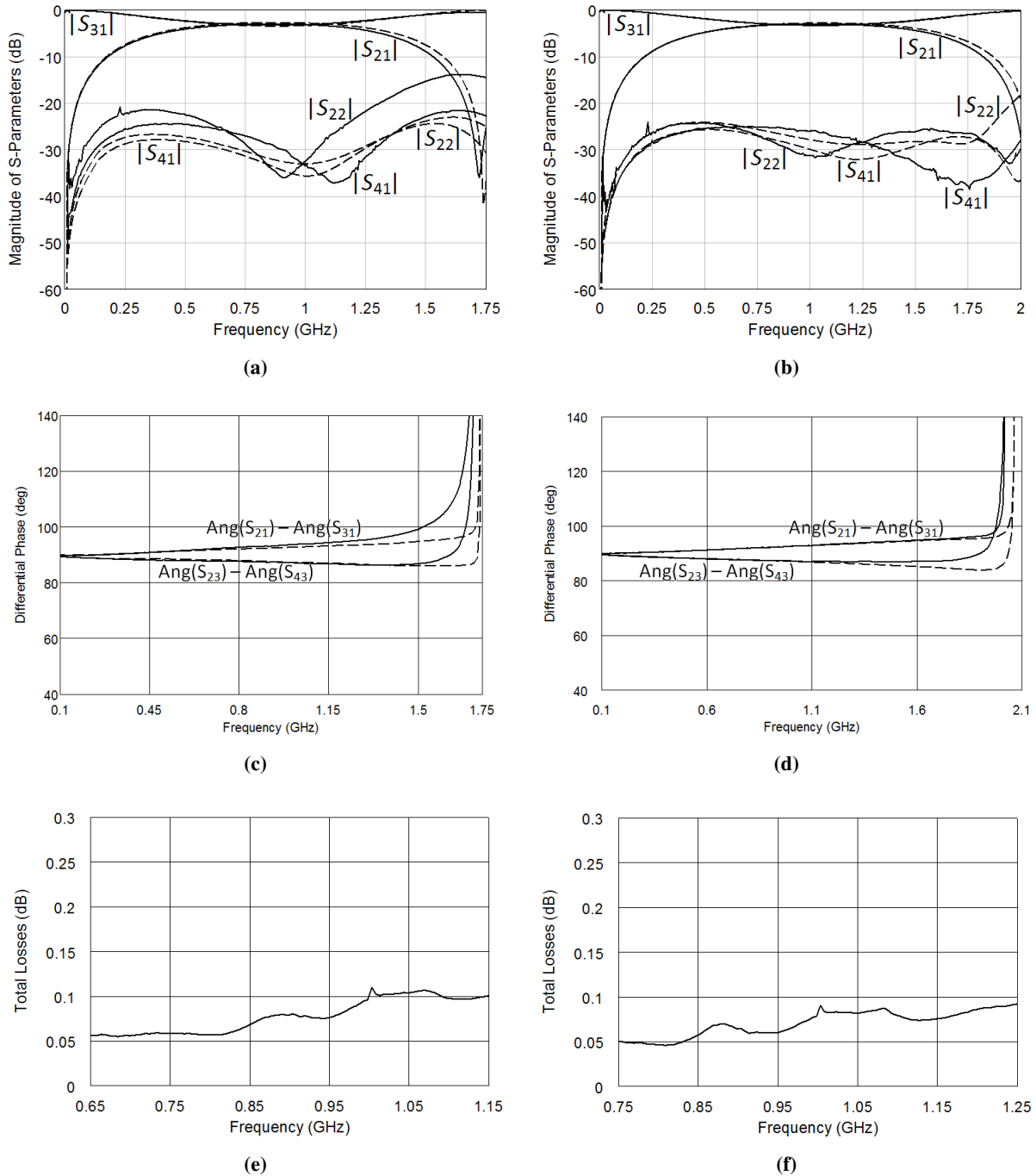
Figure 2.3: Results obtained during simulations (dashed lines) and measurements (solid lines) of designed directional coupler no. 1 operating at 890 MHz central frequency (a), (c), (e) and no. 2 which operates at 1.1 GHz central frequency (b), (d), (f). (Copyright © 2017, Wiley)

Both directional couplers have been simulated electromagnetically and the results are presented in Fig. 2.3. The results obtained during measurements of fabricated low-loss directional couplers are also shown on the same figures. As can be noticed, the obtained measurements are in good agreement with

simulations. Figures 2.3a and 2.3b show, that in both cases the isolation is greater than 24 dB and return losses are not lower than 21.7 dB. Moreover, according to the results presented in Figs. 2.3c and 2.3d, the obtained phase impbalance is not greater than 7°. Finally, the calculated total losses presented in Figs. 2.3e and 2.3f show that the fabricated directional couplers feature losses that do not exceed 0.11 dB for coupler no. 1 and 0.08 dB for coupler no. 2.

(a) **(b)**
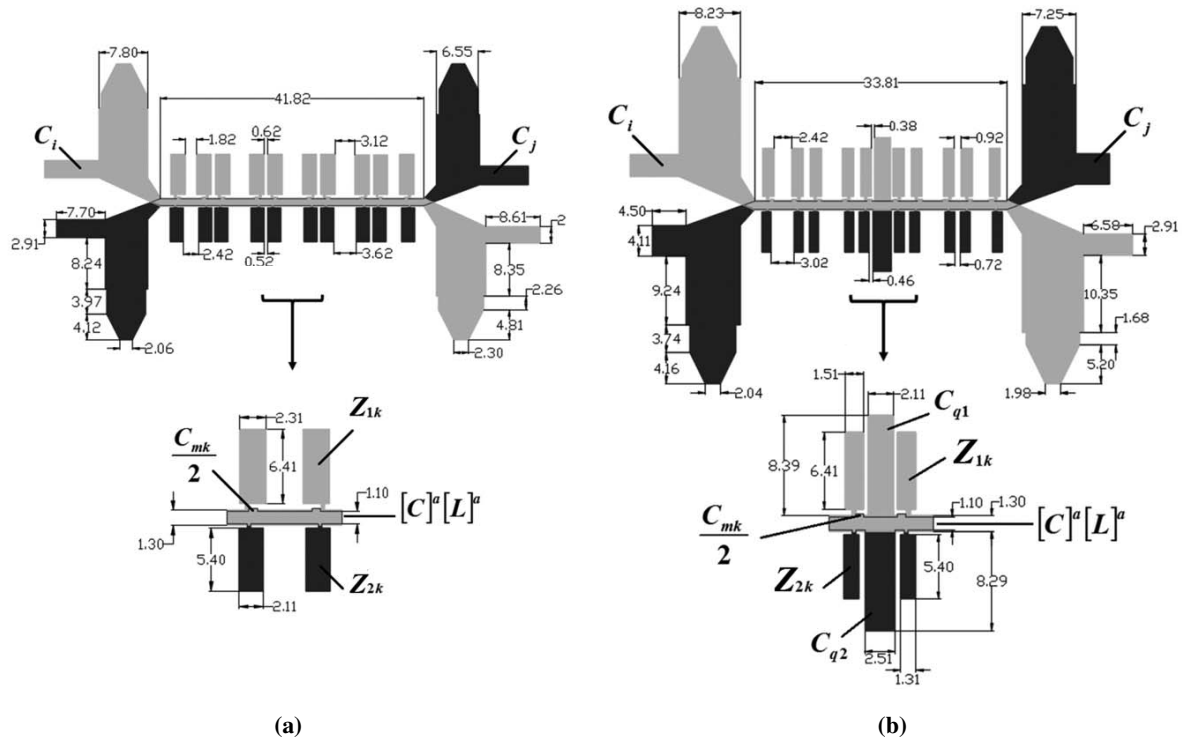
Figure 2.4: Layouts of the designed directional coupler no. 1 (a) and coupler no. 2 (b) with marked capacitances (top metallization layer - light grey; bottom - dark grey). (Copyright © 2017, Wiley)

(a) **(b)**
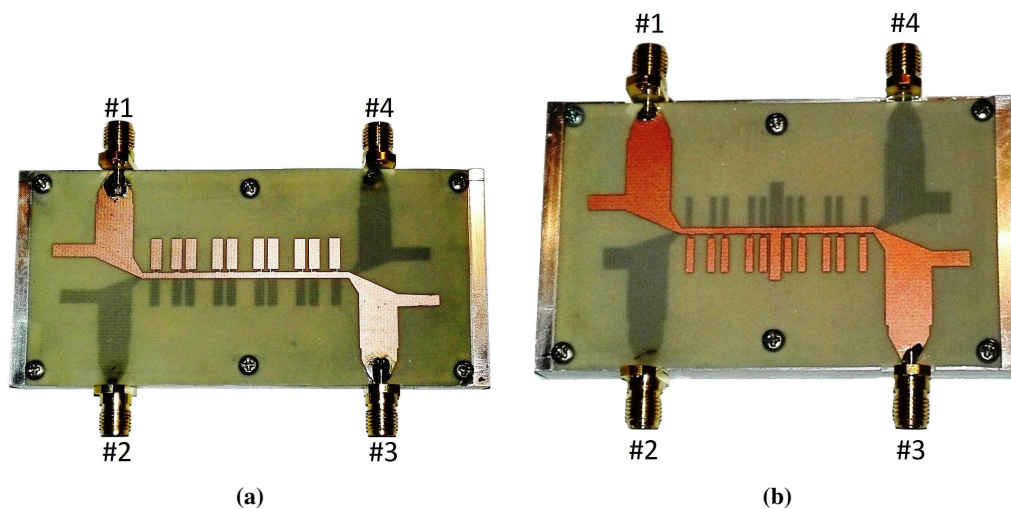
Figure 2.5: Pictures presenting fabricated low-loss coupled-line directional coupler no. 1 (a) and no.2 (b). (Copyright © 2017, Wiley)

2.1.2. Low-Loss Lange Directional Couplers

The method proposed in Subsection 2.1.1 is recommended for two coupled-line directional couplers in which the gap between the coupled conductors allows the connection of additional compensating elements. One of the most popular structures is based on the idea of interdigitated coupled-lines which, connected in the proper manner, can achieve the required strong coupling. Such a concept was proposed by Lange in [80].
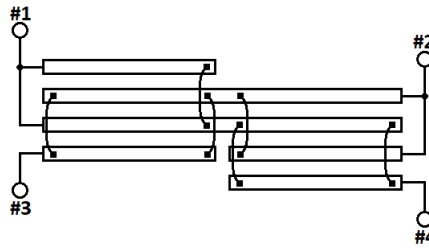
Figure 2.6: The considered Lange structure consisting of an even number of coupled-transmission-lines [65]. (Copyright © 2017, IEEE)

In [65], the author investigated such topology utilized in suspended microstrip technique to achieve low total losses. The proposed Lange directional coupler consisting of an even number of coupled transmission-lines is presented in Fig. 2.6. It has to be underlined that in such a case, the usage of lumped or quasi-lumped elements is quite difficult due to the small gap between the lines and the interconnection between transmission-lines. Thus, another compensation method has been developed to improve electrical parameters which is based on the arrangment of the substrate stack-up. In Fig. 2.7, the cross-sectional view of the stack-up is presented. In general, three dielectric layers can be seen: primary, upon which traces of Lange coupler are etched α_1 having dielectric constant ϵ_1 and height h_1; a spacing air layer which is responsible for decreasing of total losses (defined by ϵ_2 equal to unity and h_2) and a compensation layer having dielectric constant ϵ_3 and height h_3, which is responsible for equalization of the coupling coefficients.
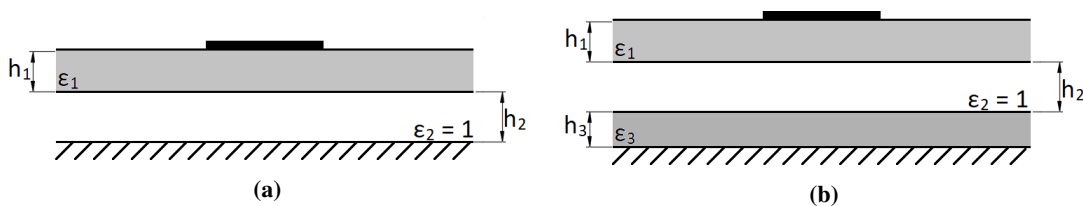
Figure 2.7: Cross-sectional view of uncompensated suspended microstrip structure(a), and stratification utilized for compensation technique (b).

For analysis purposes, an uncompensated four-line Lange configuration is used in which initial values of substrate stack-up are as follows: $h_1 = 0.15$ mm, $\varepsilon_1 = 3.38$, $h_2 = 1.35$ mm. To achieve 3-dB power split, the calculated geometry of coupled-lines needs to be $w = 0.93$ mm, and $s = 0.1$ mm. For this structure, the S-parameter frequency response has been calculated and is presented in Fig. 2.8. As can be observed, the isolation and return losses obtained for an uncompensated directional coupler deteriorate with frequency.

Such an effect is a result of an inhomogeneous dielectric medium in which capacitive k_C and inductive k_L coupling coefficients are not equal. To improve the electrical parameters of the directional coupler, the compensation method proposed for multilayer structures [65] can be used during the design process.

The research focused on the influence of the dielectric constant of the compensating layer and has been investigated for 3-dB Lange coupler. The calculated characteristics presented in Fig. 2.9a show that for small values of dielectric constant ε_3, high values of capacitive coupling can be obtained. Moreover, it can be noticed that at some point, the dependence is less significant, and the value of k_C asymptotically approaches k_L. Secondly, similar calculations have been obtained in which the influence of height h_3 on coupling coefficients is investigated; this is shown in Fig. 2.9b. Finally, for such a structure, the influence of width w and gap s between coupled-lines on coupling coefficients has been identified and the results are shown in Fig. 2.10. In these calculations, the width w of the strips has been modified to keep the terminating impedance equal to 50 Ω. As can be seen, the geometry compensates for strong coupling of around 3-dB and for lower couplings, the additional compensating layer needs to be adjusted.
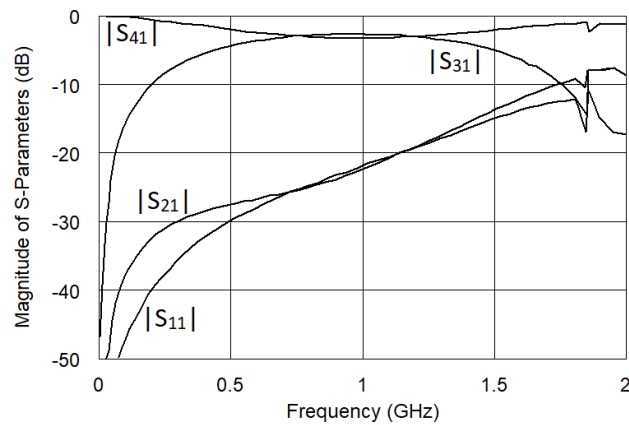
Figure 2.8: Calculated response of uncompensated Lange directional coupler [65]. (Copyright © 2017, IEEE)

(a)

(b)
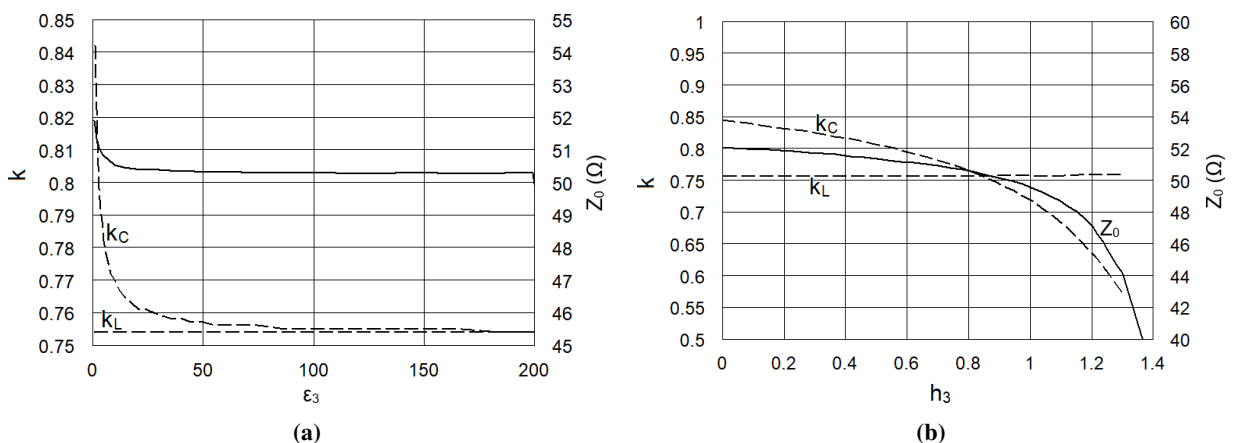
Figure 2.9: Graphs presenting the influence of dielectric permittivity ε_3 (a), and height h_3 (b) of the compensation layer on coupling coefficients k_L and k_C, and characteristic impedance Z_0. The dashed lines represent inductive and capacitive coupling coefficients; the solid line show the behavior of characteristic impedance. The obtained calculations assume that: $w = 0.93$ mm, $s = 0.1$ mm, $h_1 = 0.15$ mm, $\varepsilon_1 = 3.38$, $h_2 = 0.59$ mm, and $h_3 = 0.76$ mm for (a); $h_2 + h_3 = 1.35$ mm, $\varepsilon_3 = 10.1$ for (b) [65].(Copyright © 2017, IEEE)
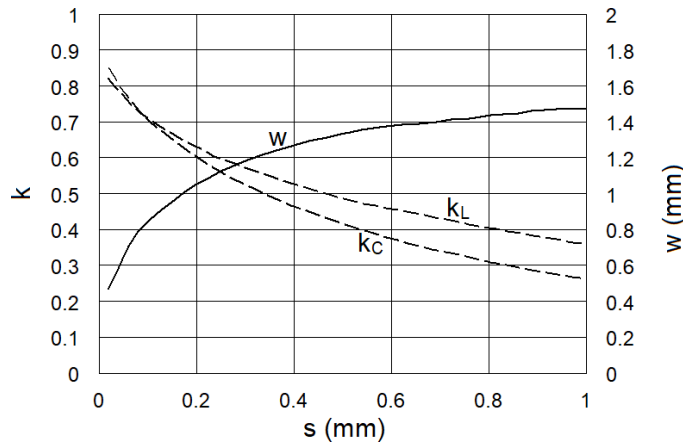
Figure 2.10: Influence of spacing between coupled-lines on coupling coefficients and strip width. The obtained calculations assume that: Z_0 ($h_1 = 0.15$ mm, $\varepsilon_1 = 3.38$, $h_2 = 0.59$ mm, $h_3 = 0.76$ mm and $\varepsilon_3 = 10.1$) [65]. (Copyright © 2017, IEEE)

The results obtained for the calculated compensated Lange structure are presented in Fig. 2.11. In comparison to results obtained for the uncompensated structure, it can be seen that isolation and return losses significantly increased after utilizing the proposed compensation method.
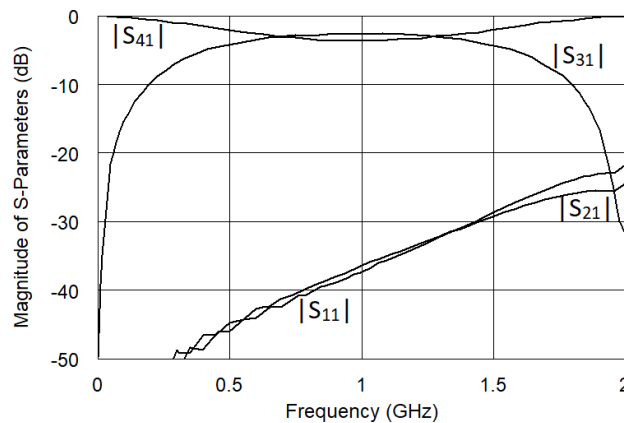
Figure 2.11: Calculated frequency response of the compensated Lange directional coupler. Results obtained for the following geometry of the structure: $w = 0.68$ mm, $s = 0.06$ mm, $h_1 = 0.15$ mm, $\varepsilon_1 = 3.38$, $h_2 = 0.59$ mm, $\varepsilon = 1$, $h_3 = 0.76$ mm, $\varepsilon = 10.1$ [65]. (Copyright © 2017, IEEE)

To verify the applicability of the proposed compensation method, a low-loss 3-dB Lange coupler was designed. The utilized stratification is presented in Fig. 2.12. The substrate layers have the following parameters: $h_1 = 0.15$ mm, $\varepsilon_1 = 3.38$, $h_2 = 1.59$ mm, $\varepsilon_2 = 1$, $h_3 = 0.76$ mm and $\varepsilon_3 = 10.1$ and the geometry of four-coupled lines are: $w = 0.68$ mm and $s = 0.06$ mm.
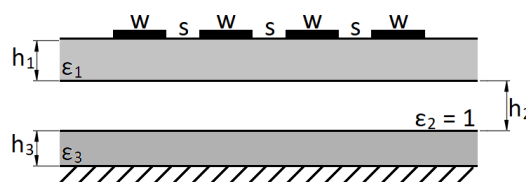
Figure 2.12: The susbstrate stratification utilized in low-loss Lange coupler. (Copyright © 2017, IEEE)

The considered geometry was simulated electromagnetically in AWR Microwave Office software. It should be mentioned that the Lange structure was connected to the ports using 50 Ω signal lines. The resulting connections create discontinuity regions which deteriorate the performance of the coupler. Therefore, to imptove the parameters, additional compensation capacitances have been added. The obtained simulations results together with measurements are presented in Fig. 2.13.
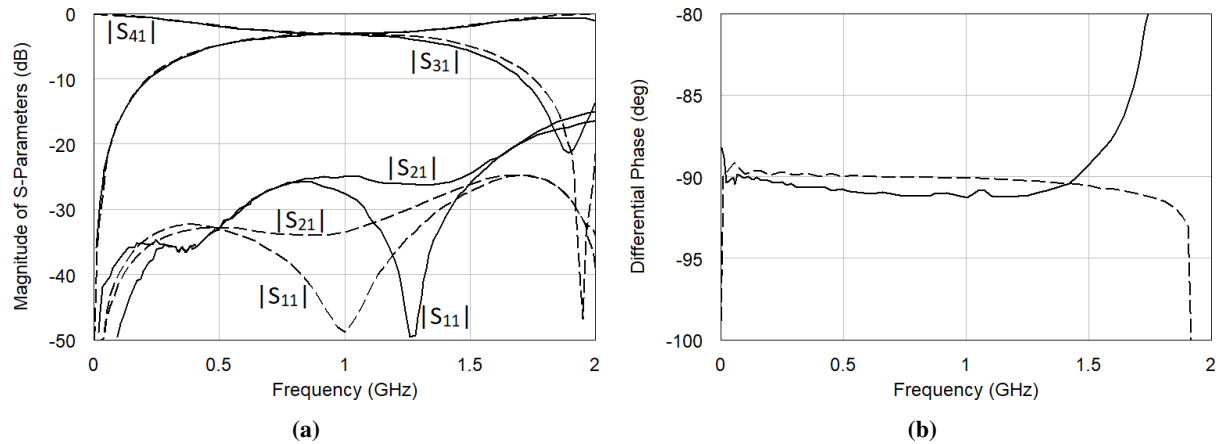
Figure 2.13: Results obtained during electromagnetic simulations (dashed lines) and measurements (solid lines) of the designed low-loss Lange directional coupler. (Copyright © 2017, IEEE)
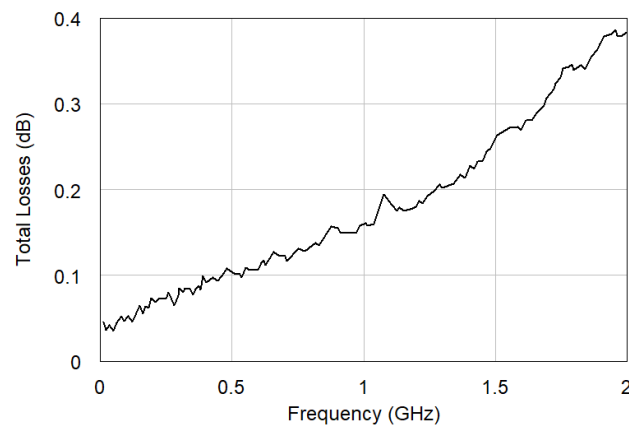
Figure 2.14: Measured total losses of manufactured low-loss Lange directional coupler. (Copyright © 2017, IEEE)

According to the collected measurements, the isolation and return lossses are not worse than 25 dB and the phase imbalance of the coupler is not greater than 1°. Moreover, the total losses of the compensated Lange coupler do not exceeded 0.16 dB at the center frequency, which can be noticed in Fig. 2.14. This result is comparable to the directional coupler utilized in the stripline technique [113], where losses are at a level of 0.1 dB. However, the proposed approach is easier to integrate in complex applications such as power amplifiers. A fabricated compensated Lange directional coupler is shown in Fig. 2.15.
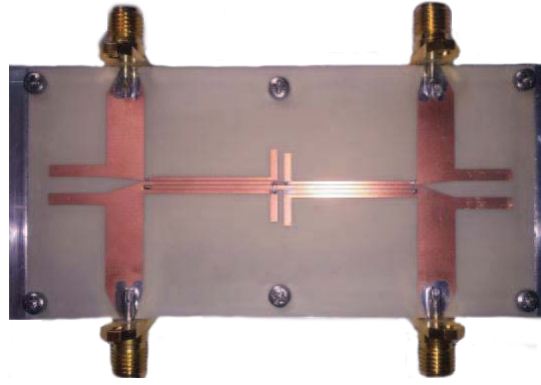
Figure 2.15: Fabricated low-loss Lange directional coupler. (Copyright © 2017, IEEE)

2.2. High-Performance Directional Couplers in Monolithic Technology

Monolithic applications such as balanced networks, are commonly composed of directional couplers [8], [69], [67], [99], [82]. Compact sizes of designed circuits are obtained by using lumped elements instead of distributed ones [94], [38], [8]. Notwithstanding this fact, the obtained frequency response of such couplers is narrow and the imbalance between transmission and coupling can be large, which limits their applicability in broadband solutions. The coupled-line sections can be used to achieve broader operational bandwidth [137], [75], [155]. However, the design of such components is commonly difficult due to the physical limitations of the considered technological process.

In this section, a novel compensation method improving the performance of the chosen monolithic couplers is presented. The applicability of the proposed method has been verified by utilizing the improved Lange coupler, a three-coupled-line section and a structure composed of symmetric two-coupled-line and left-handed sections.

2.2.1. A Short Brief on PH25 Process by UMS Monolithic Semiconductors

Monolithic circuits presented in this dissertation are based on the PH25 gallium arsenide process from *United Monolithic Semiconductors* (UMS). The substrate stack-up is presented in Fig. 2.16 and it can be seen that the stratification is composed of three main dielectric layers. The base substrate is gallium arsenide (GaAs) which has a thickness of 100 μm and a dielectric constant equal to $\varepsilon_r = 12.8$. On top of GaAs, two layers (passivation layer and nitride layer) are placed which are respectively 0.23 μm, and 0.21 μm thick. The dielectric permittivity of both layers is equal to $\varepsilon_r = 7.2$. The chosen technology has two metallization layers which can be used in designs. The first layer ($M1$) is placed on the top of the structure and it is made of gold. It must be mentioned that this is the main layer for utilizing signal routing. By contrast, $M2$ is a buried, thin layer which has higher resistivity than $M1$ and is commonly used to form electrodes of MIM capacitors.

For the process stratification presented in Fig. 2.16, four commonly utilized coupled-line geometries were investigated in terms of the modal dielectric constant and coupling coefficient variations. During the calculations, physical constraints collected in Table 2.2 were taken into account.
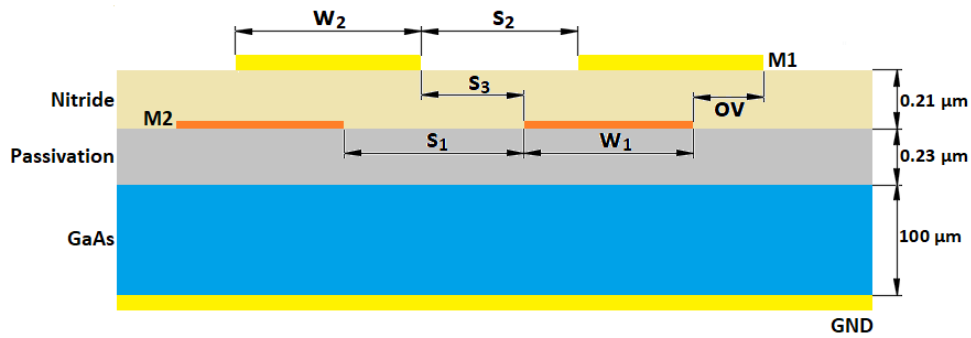
Figure 2.16: The simplified stack-up of the PH25 process from UMS.

Table 2.2: Physical limitations of the UMS PH25 process.

Dimmension	w_1	w_2	s_1	s_2	s_3	ov
Layout Constraint (μm)	>4	>5	>4	>8	>4	>2

2.2.2. Analysis of the Realization of the Coupled-Line Section in the UMS PH25 Process

A) Symmetric Edge-Coupled Lines

The symmetric coupled-line section is one of the most fundamental structures. The maximum coupling between conductors is mainly limited by the minimum gap s_2 between two coupled strips located on top of the metallization layer $M1$, which has an affect upon the maximum available coupling coefficient k. For a minimum distance equal to 8 μm, coefficient $k_{max} = 0.545$, assuming that characteristic impedance $Z_0 = 50$ Ω. Figure 2.17a presents the calculated relation between the coupling coefficient and gap s_2; Figure 2.17b shows the calculated even and odd mode dielectric constants. It can be seen that such a geometry can be commonly used for weakly-coupled directional couplers.
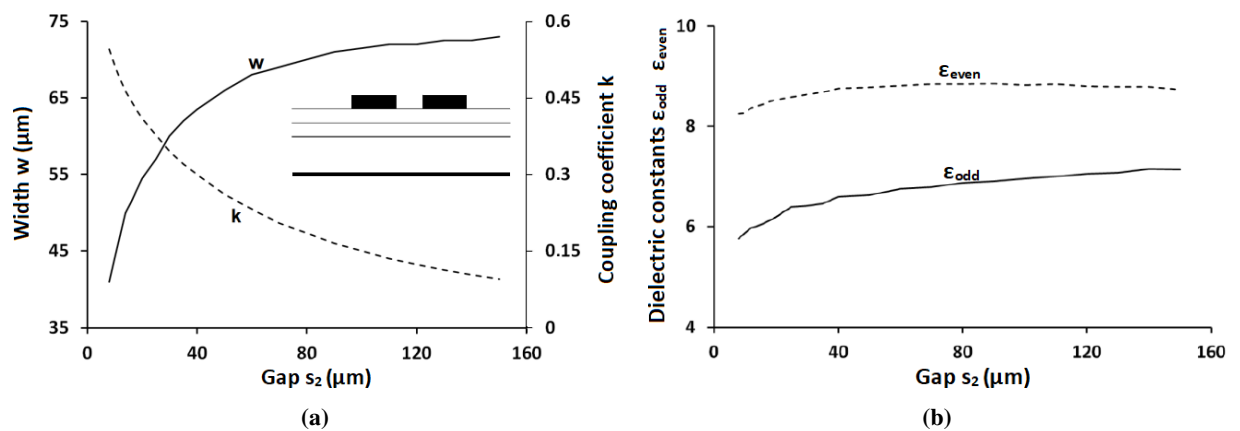
Figure 2.17: Calculated strip widths and coupling coefficient (a) and even and odd relative dielectric constants (b) for edge coupled-line geometry. [44]. (Copyright © 2019, MDPI)

B) Two-Strip Asymmetric Coupled-Lines

The second configuration of coupled lines is commonly known as two-strip broadside geometry, and in PH25 technology, it can be fabricated using two metallization layers $M1$ and $M2$. In such a structure, two strips have to be separated by the minimum gap $s_3 > 4\ \mu m$.

In general, both layers are utilized to form structures called bridges (or cross sections). Moreover, the minimum overhang ov of crossed $M1$ and $M2$ conductors has to be greater than $2\ \mu$m. The calculated capacitive and inductive coupling coefficients and strip widths vs. the gap between the lines s_3 are presented in Fig. 2.18. It must to be mentioned that calculations have been done for the 50 Ω standard. According to the obtained calculations, the maximum available coupling coefficient k is not greater than 0.6.
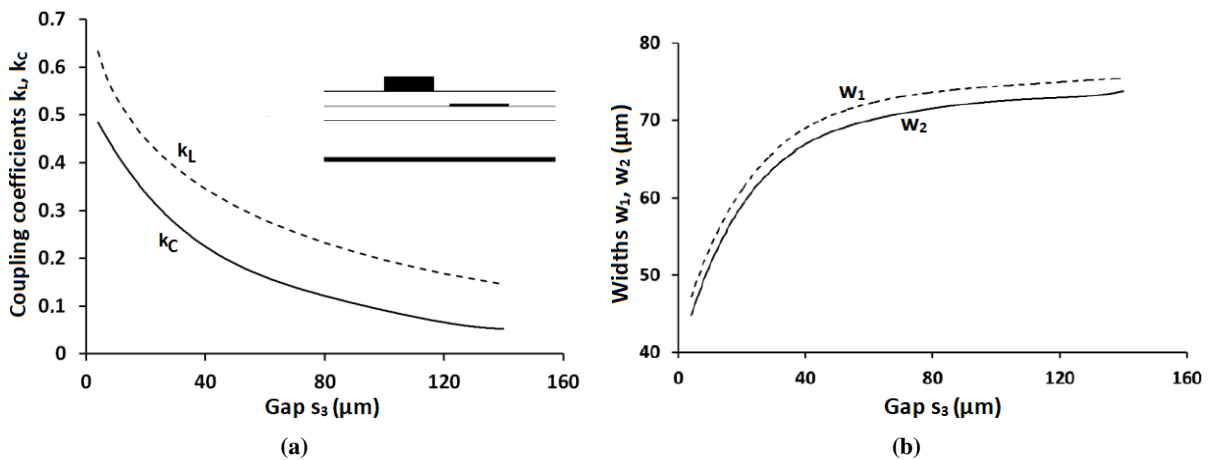
Figure 2.18: Calculated inductive and capacitive coupling coefficients (a) and strip widths (b) for the two-strip asymmetric coupled-line geometry [44] . (Copyright © 2019, MDPI)
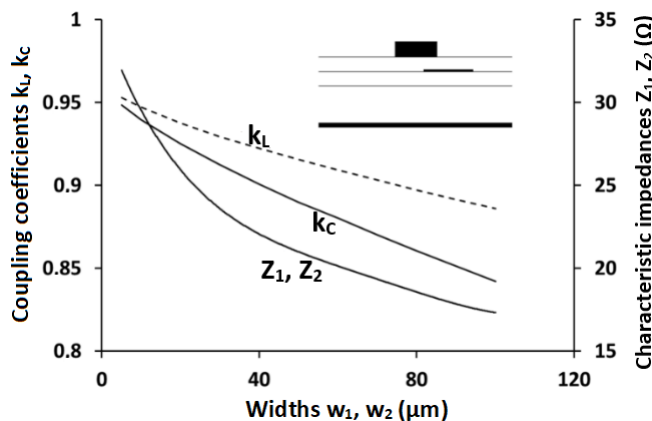
Figure 2.19: Calculated inductive and capacitive coupling coefficients and characteristic impedances of the coupled conductors for the two-strip asymmetric coupled-line geometry with an overlap between the conductors [44]. (Copyright © 2019, MDPI)

Similar characteristics are presented in the case of over hanged strips in Fig. 2.19. In this case, due to the very small thickness of the separating nitride layer, and thus a high mutual capacitance between the strips, the achievable coupling is very high. However, in this case there is a problem with the characteristic impedance, which is always much lower than 50 Ω and is also limited by the minimum widths of the conductors. To conclude, the two-strip configuration can also be practically used for the

realization of weakly coupled lines, as is the case with the geometry described in the previous subsection.

C) Three-Strip Asymmetric Coupled-Lines

The three-strip coupled-line geometry can be utilized to achieve the required strong coupling. Such a structure is presented in Fig. 2.20a. In this configuration, the two conductors placed on the $M2$ layer (#2, #3) are connected and treated as one conductor which is coupled to the conductor on the top metallization layer (strip #1). The calculated coupling coefficients and the strip widths are presented in Fig. 2.20. From the presented calculations, it can be seen that the mean coupling coefficient reaches $k = 0.71$ for the minimum gap between the conductors of $s_3 = 4$ um.
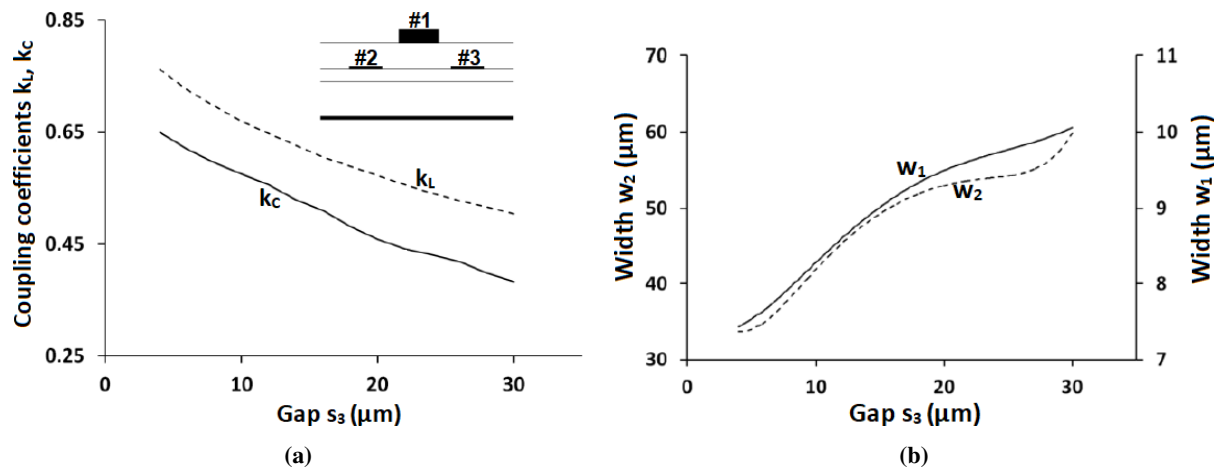
Figure 2.20: Calculated inductive and capacitive coupling coefficients (a) and strip widths (b) for the three-strip asymmetric coupled-line geometry [44]. (Copyright © 2019, MDPI)
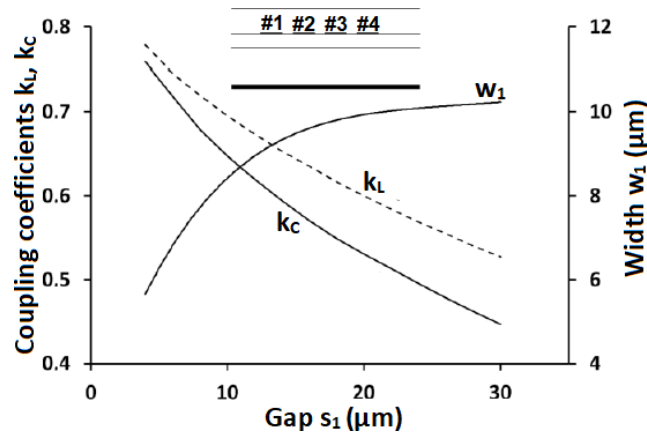
Figure 2.21: Calculated coupling coefficients and strip widths of coupled conductors for the four-strip coupled-line geometry, in which conductors #1 and #3 constitute the first coupled line and conductors #2 and #4 constitute the second coupled line [44]. (Copyright © 2019, MDPI)

D) Interconnected Four-Coupled-Lines

The last geometry which is considered is the four-coupled-strip configuration. Such an interdigitated structure is commonly utilized in Lange couplers, and is presented in Fig. 2.21. The calculated coupling coefficients and the strip widths are presented in the same figure. As can be noticed, the considered geometry enables a tight coupling realization of $k = 0.77$ with the constraints given in the UMS PH25

process. It is worth noting that the four-coupled-line geometry also features the inequality of coupling coefficients, as is the case with the three-strip geometry. The requirement for the realization of the four-strip Lange coupler is the necessity of the bonding connection of non-adjacent strips (#1 with #3 and #2 with #4). In the UMS PH25 process, such connections can be made by using bonds formed on the top metallization layer $M1$.

2.2.3. Capacitive Compensation Method For MMIC Technologies

All of the presented geometries can be used to design directional couplers. To achieve the strongest coupling between conductors, the most suitable are asymmetric coupled sections. However, for such structures, the problem of the inequality of inductive and capacitive couplings is met. Thus, a novel compensation method has been proposed. During calculations it was observed, that the inductive coupling coefficient is greater than the capacitive coefficient. According to Subsection 1.4 for such a case, three additional elements have to be added to the main coupled section to compensate for this inequality: mutual capacitance between lines C_m; self capacitances C_1, C_2; short compensating sections of coupled-lines defined by matrices: $[L]^b$, $[C]^b$. Such an approach can be difficult to implement in the case of the monolithic technique. Therefore, a novel compensation method has been proposed in which only additional compensating mutual capacitance C_m is used to equalize the coupling coefficients [44].

The schematic of the compensated coupled-line directional coupler is shown in Fig. 2.22. As can be observed, the considered structure is divided in to n-subsection as in the case investigated in the Introduction. For the considered case, the proposed methodology assumes that the following relation has to be fulfilled:

$$k_C = k_L = k_{Required}. \tag{2.5}$$

Assuming that most of the modern solutions are based on a 50 Ω standard, it should be mentioned that

$$Z_{T1} = Z_{T2} = 50\Omega. \tag{2.6}$$

The coupling coefficients can be calculated with the following equation:

$$k_{Required}^2 = k_C^2 = k_L^2 = \frac{(C_{12} + C_d)^2}{(C_{11} + C_d)(C_{22} + C_d)} \tag{2.7}$$

which can be used to find the value of the compensation capacitance C_d after solving the quadratic equation:

$$C_d^2 (1 - k_L)^2 + C_d \left[2C_{12} - k_L^2 (C_{11} + C_{22}) \right] + C_{12}^2 - k_L^2 C_{11} C_{22} = 0. \tag{2.8}$$

It has to be mentioned, that only positive solutions receive further consideration. The calculated value of compensation capacitance must be taken into account during calculations of strip impedances Z_{T1} and Z_{T2} due to the direct influence on them which is defined by the formula:

$$Z_{T1} = \sqrt{\frac{L_{11}}{C_{11} + C_d}}, \quad Z_{T2} = \sqrt{\frac{L_{22}}{C_{22} + C_d}}. \tag{2.9}$$

The derived value of capacitance C_d is treated as a distributed capacitance between coupled transmission-lines. In practice, C_d is realized as the number of lumped capacitors C_{cm} connected along the lines, and the capacitor values can be calculated as

$$C_{cm} = \frac{C_d}{n} l \tag{2.10}$$

where l is the physical length of the coupled lines and n is the number of lumped capacitors that have to be added to the circuit for the required capacitance C_d.
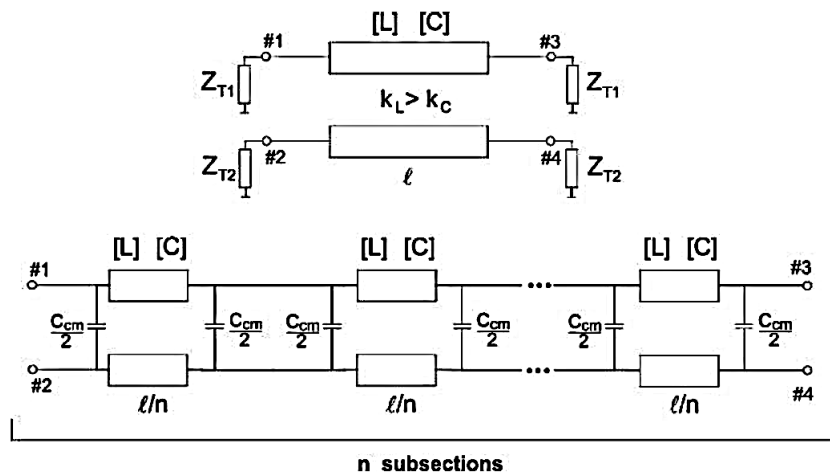
Figure 2.22: Schematic diagram of compensated coupled-line directional coupler [44]. (Copyright © 2019, MDPI)

In a practical sense, to design a coupled-lines section, one needs to iteratively modify the geometry and calculate equations 2.8 and 2.9 to meet the required impedances. The overall coupling will be equal to the inductive coupling coefficient that is not influenced by the compensation. The number of possible solutions is infinite. However, from the practical point of view, the idea is to obtain the values of C_{cm} that are as small as possible to make the practical realization possible. Furthermore, it should be mentioned that the presented analysis has been investigated for asymmetric coupled-lines sections. However, the proposed compensation method can be also used for the symmetric coupled sections, where equalization of the modal dielectric constants (ε_e and ε_o) has to be obtained.

2.2.4. Design of Coupled-Line 3-dB Directional Couplers using the UMS PH25 Process

A) Compensated Three-Strip Asymmetric Coupled-Line Directional Coupler

As presented in Subsection 2.2.2, three-coupled-line section (Fig. 2.23a) can be utilized in the UMS PH25 technology to achieve a coupling level reaching a value of 0.71. However, capacitive and inductive coupling coefficients are not equal i.e. $k_L > k_C$. Therefore, the obtained electrical parameters such as return loss and isolation degrades with increasing frequency, which can be seen in the response presented in Fig. 2.23b. The results were obtained for a coupled-line section operating at a center frequency of

24 GHz in which the coupling coefficient $k = 0.707$ (3 dB), and terminating impedances are 50 Ω. Inductive and capacitive coupling coefficients are respectively $k_L = 0.7632$, $k_C = 0.6497$, which corresponds to following geometry of the coupled section: $w_1 = 7.5\ \mu m$, $w_2 = 34.5\ \mu m$, $s_3 = 4\ \mu m$. For such a structure, the per-unit length matrices are calculated with equations 2.11, 2.12.

$$[L] = \begin{bmatrix} 605.7 & 459.3 \\ 459.3 & 579.9 \end{bmatrix} \begin{bmatrix} nH \\ \overline{m} \end{bmatrix} \tag{2.11}$$

$$[C] = \begin{bmatrix} 243.8 & -156.6 \\ -156.6 & 238.3 \end{bmatrix} \begin{bmatrix} pF \\ \overline{m} \end{bmatrix} \tag{2.12}$$
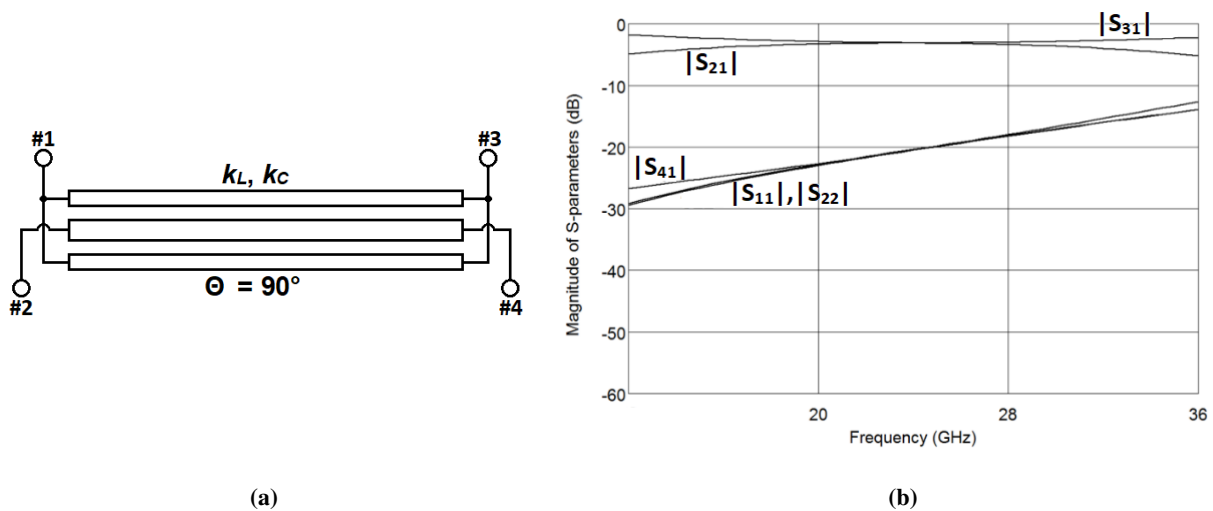
Figure 2.23: Three-strip coupled-line directional coupler (a), and calculated frequency response of uncompensated three-strip coupled-line section which is defined by the inductive coupling coefficient $k_L = 0.7632$, and the capacitive coupling coefficient $k_C = 0.6497$ (b). (Copyright © 2019, MDPI)

It is worth to underlining, that the presented results are strictly theoretical and do not include the impact of the necessary connection of the strips w_1 , the connection of the input/output transmission lines, and the manufacturing accuracy. Thus, in practice the overall performance of such a section would be worse than the presented results.

To illustrate the advantages of the proposed compensation method applied in monolithic technology, the considered structure has been redesigned and a new geometry has been found: $w_1 = 4\ \mu m$, $w_2 = 17\ \mu m$, and $s_3 = 4\ \mu m$. The obtained coupling coefficients of the uncompensated structure are as follows: $k_L = 0.7658$, $k_C = 0.6452$, and the reduced per-unit-length matrices are:

$$[L] = \begin{bmatrix} 725.9 & 773.7 \\ 553.7 & 720.1 \end{bmatrix} \begin{bmatrix} nH \\ \overline{m} \end{bmatrix} \tag{2.13}$$

$$[C] = \begin{bmatrix} 193.1 & -122.6 \\ -122.6 & 187.2 \end{bmatrix} \begin{bmatrix} pF \\ \overline{m} \end{bmatrix}. \tag{2.14}$$

The derived values have been calculated assuming that the terminating impedances are Z_{T1} = 61.31 Ω and Z_{T2} = 62.02 Ω. The value of the compensating capacitance which equalizes the coupling coefficients was calculated by solving equation 2.8. The compensating capacitance C_d = 97.92 pF/m for k_C = k_L = 0.7658, and terminating impedances Z_{T1} = 49.94 Ω, Z_{T2} = 50.26 Ω. The modified capacitance matrix of the compensated structure is:

$$[C] = \begin{bmatrix} 291.0 & -220.6 \\ -220.6 & 285.1 \end{bmatrix} \left[\frac{pF}{m} \right]. \tag{2.15}$$

The calculated response of the compensated three-conductor coupled-lines directional coupler is presented in Fig. 2.24a. It has to be mentioned that the derived results are obtained for a structure in which the compensating capacitance C_d was calculated according to equation 2.8, and is 97.92 pF/m. Electromagnetic simulations of the designed directional coupler are shown in Fig. 2.24b. For such a coupler, five additional compensating quasi-lumped capacitors C_{Cm} have been added. The value of capacitance calculated from equation 2.10 is C_{Cm} = 22 fF.
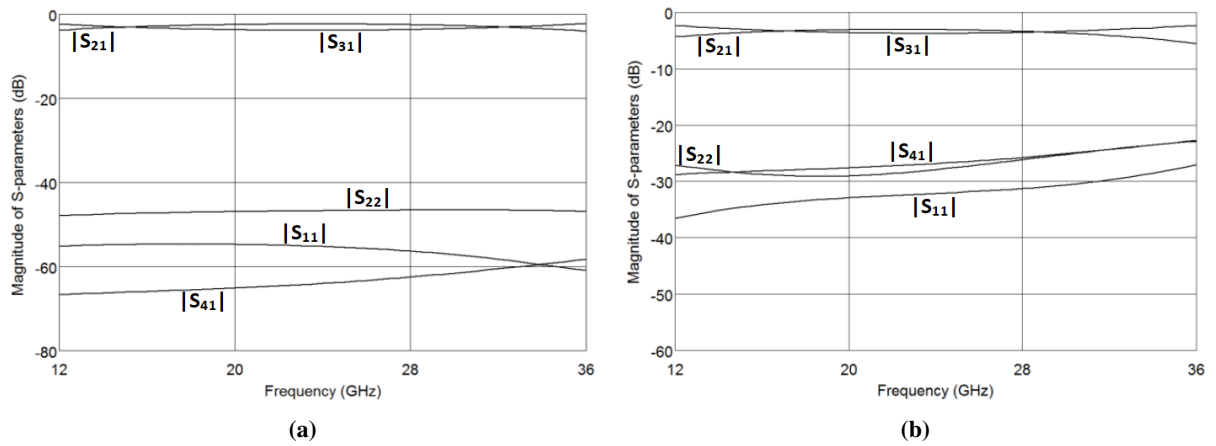
Figure 2.24: Results obtained during calculations (a), and electromagnetic simulations (b) of compensated three-coupled-line directional coupler in which coupling coefficients are equal k_L = k_C = 0.7658. (Copyright © 2019, MDPI)
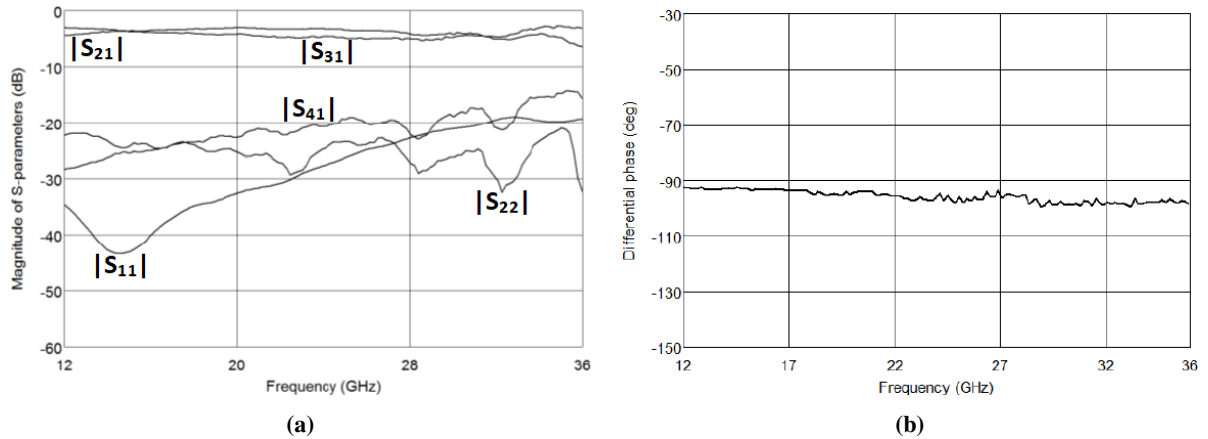
Figure 2.25: Results obtained during measurements of manufactured compensated three-strip coupled directional coupler. The S-Parameters of the coupler are presented in (a) and (b) shows the differential phase. (Copyright © 2019, MDPI)

Measurements of the fabricated directional coupler are presented in Fig. 2.25. As can be observed, the return losses are better than 24 dB, the isolation is greater than 20 dB and the phase imbalance does not exceed 5.5° at the 24 GHz center frequency. A picture presenting SEM photography of the fabricated component is presented in Fig. 2.26. The overall size of the designed coupler is 1.6 x 0.5 mm including the 50 Ω signal lines.
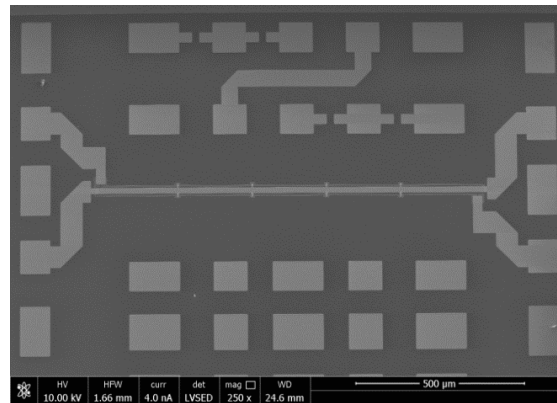
(a)
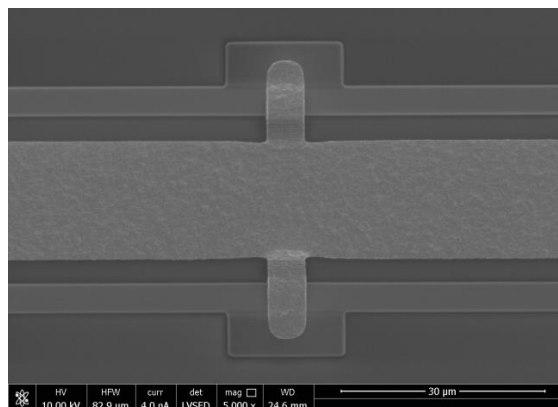
(b)

Figure 2.26: SEM photographs of the manufactured three-strip compensated directional coupler. Overall view (a) and a close-up view of one of the compensating capacitors between the coupled conductors (b).

B) Lange-Type Compensated Directional Coupler

The interconnected four-conductor coupled lines developed using the microstrip technique can be utilized to obtain strong coupling, which was investigated for the UMS PH25 process in Subsection 2.2.2. However, as in the case of the three-coupled-line coupler, the inequality of coupling coefficients exists. Therefore, the same compensation method can be utilized to improve the electrical performance of the coupled section. To verify the possibility of implementation of the proposed method, the Lange topology presented in Fig. 2.27a, which is a particular case of an interdigitated structure, was chosen. For such a structure, operating at the 24 GHz center frequency the following geometry has been found: $w_1 = 6.7\ \mu m$, and $s_1 = 6\ \mu m$, which corresponds to the electrical parameters: $k_L = 0.7447$, $k_C = 0.7165$, and $Z_{T1,2} = 50.04\ \Omega$. The frequency response of an uncompensated Lange directional coupler is presented in Fig. 2.27b.
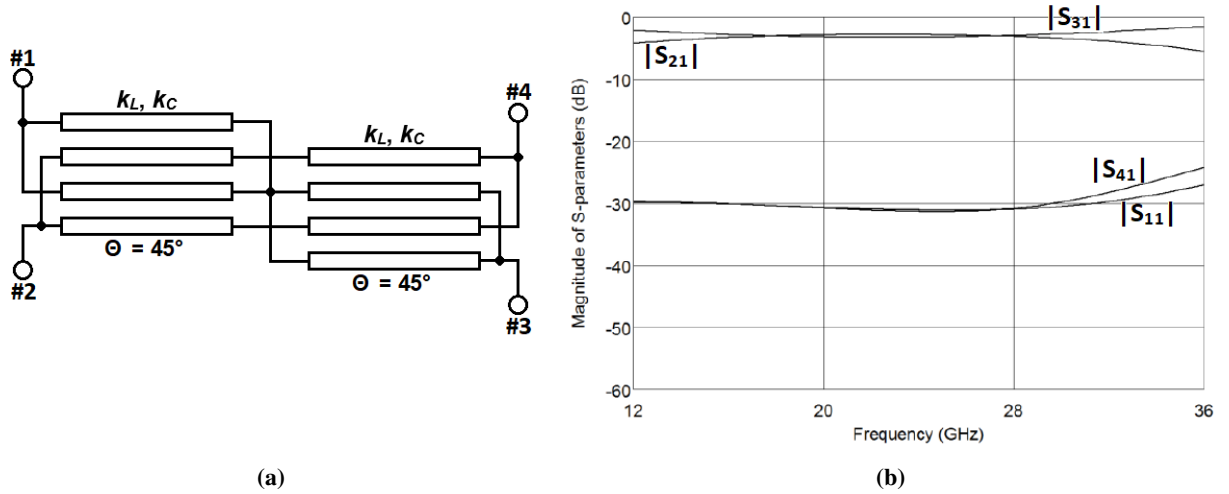
Figure 2.27: Concept view of Lange directional coupler used in the monolithic realization of the considered design (a), and calculated frequency response of an uncompensated interconnected-four-strip coupled section with coupling coefficients: $k_L = 0.7447$ and $k_C = 0.7165$ (b). (Copyright © 2019, MDPI)
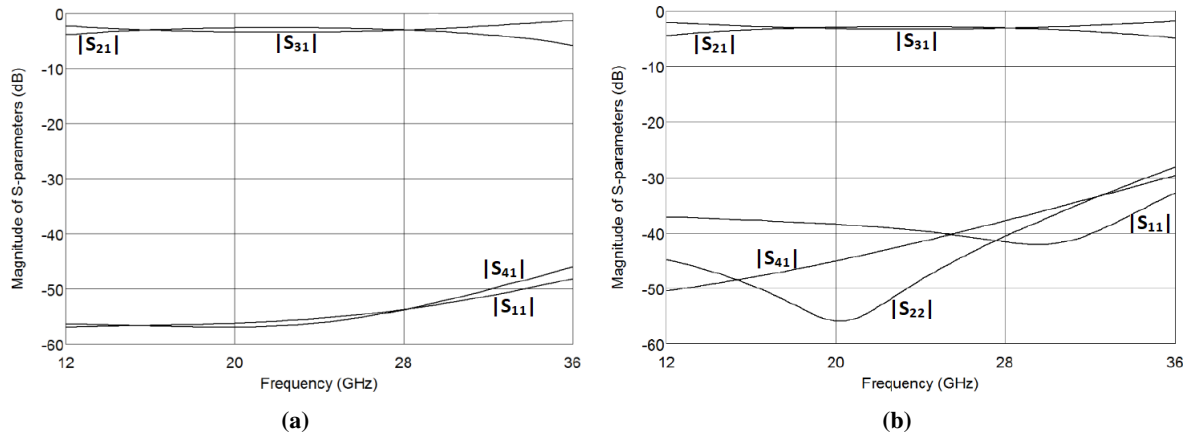
Figure 2.28: Calculated (a) and electromagnetically simulated (b) frequency responses of the compensated Lange directional coupler in which $k_L = k_C = 0.7411$. (Copyright © 2019, MDPI)

In comparison to the three-conductor coupled-line section presented in Subsection 2.2.4, the calculated response is better in terms of coupling imbalance, return losses and isolation. However, the electrical performance can be significantly improved by using the considered compensation method. The compensating capacitance C_d was found using the procedure applied in the previous subsection for which equalization of the coupling coefficients was obtained ($k_L = k_C = 0.7411$). The calculated response of the compensated interconnected-four-strip coupled section is presented in Fig. 2.28a, where the derived compensation capacitance is $C_d = 26.6$ pF/m. Having found C_d, C_{Cm} was calculated under the assumption that the coupled section was divided in to five subsections. The compensating capacitances C_{Cm} are equal to 5.9 fF. Such a small value was realized as quasi-lumped capacitors by proper formation of the bonding connections between lines. Physically, they were designed as 5 um-wide ribbons that bonded the conducting strips and were elevated 2 um above the surface of the chip (2 um

air spacing between the ribbon and the top layer of the chip). The electromagnetic simulations of the designed interconnected four-strip Lange directional coupler are shown in Fig. 2.28b.

(a)   (b)
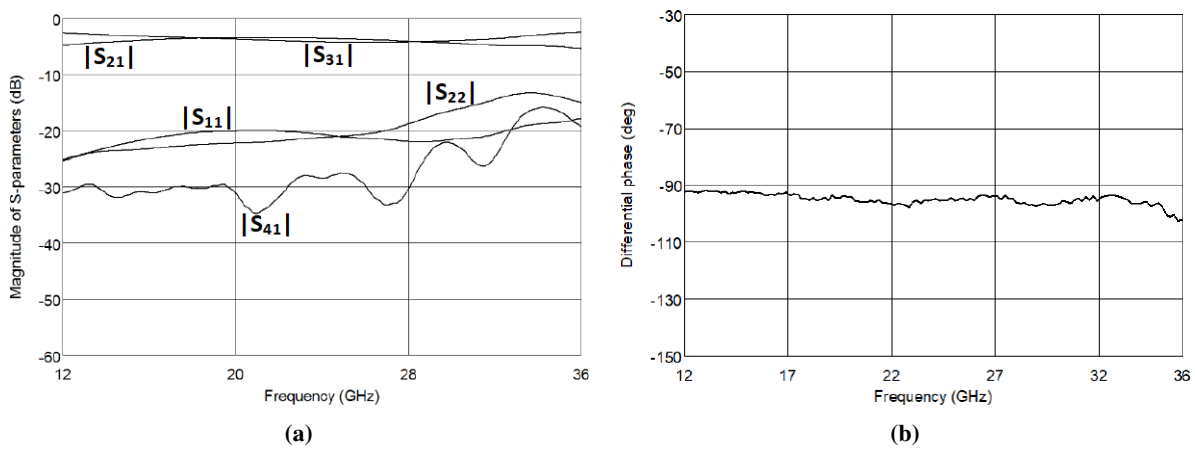
Figure 2.29: S-Parameters (a) and differential phase (b) obtained during measurements of the fabricated interconnected four-strip directional coupler. (Copyright © 2019, MDPI)

The compensated Lange directional coupler was fabricated using UMS PH25 technology and was then measured. The collected results are presented in Fig. 2.29. The obtained measurements are in good agreement with the simulated results. The measured isolation is not lower than 28 dB, and the phase imbalance is not greater than 5° at the center frequency. Figure 2.30 shows SEM photography of the fabricated compensated Lange coupler. The overall size of the manufactured chips is 74 x 1206 μm.

(a)   (b)
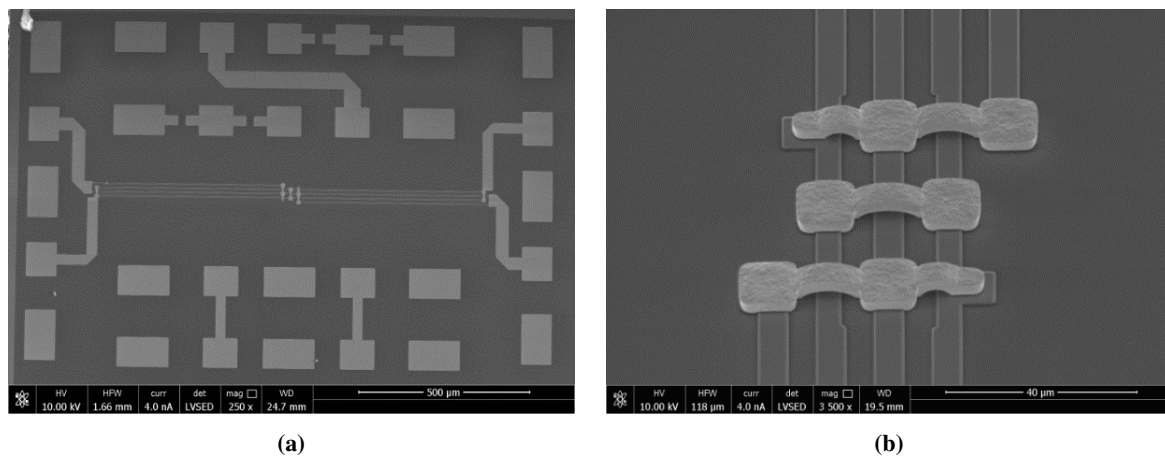
Figure 2.30: SEM photographs of the fabricated compensated Lange directional coupler utilized in the UMS PH25 process. Overall view of the manufactured chip (a) and magnified view of compensating bounding ribbons (b). (Copyright © 2019, MDPI)

C) Directional Coupler with Left-Handed Sections

Multi-conductor coupled sections are one of the most popular structures for the realization of directional couplers. However, left-handed structures can also be used to achieve a high coupling coefficient without the requirement for strong coupling in the coupled-line section [129], [131]. Thus, the directional coupler presented in [131] has been investigated in terms of its realization in monolithic technology.
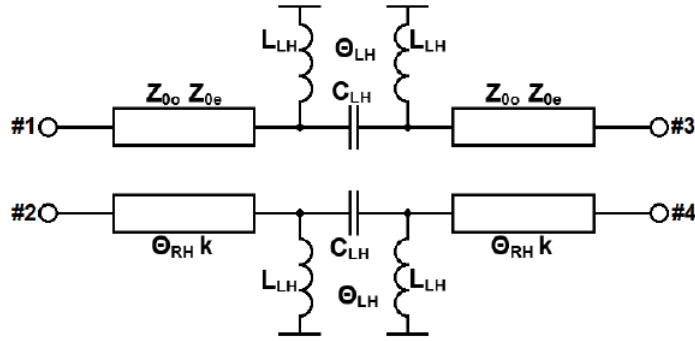
Figure 2.31: Concept view of directional coupler consisting of left-handed sections. (Copyright © 2019, MDPI)

Figure 2.31 shows the directional coupler utilizing a left-handed transmission line section. As can be seen, such a coupler consists of two symmetric coupled-lines and lumped elements in the center of the structure. As shown in the analysis conducted in Subsection 2.2.2, the symmetric edge-coupled-line section features maximum coupling of k = 0.566. Therefore, calculations of the ideal directional coupler operating at a 24 GHz center frequency have been performed assuming such a maximum value. The electrical parameters of the symmetric coupled-line section are as follows: Z_{0e} = 88.01 Ω, Z_{0o} = 28.40 Ω, Θ_{RH} = 55.4 $^\circ$ and the lumped elements have the values: L_{LH} = 0.97 nH, C_{RH} = 0.216 pF. For such parameters, the ideal response of the directional coupler is calculated in Fig. 2.32a.
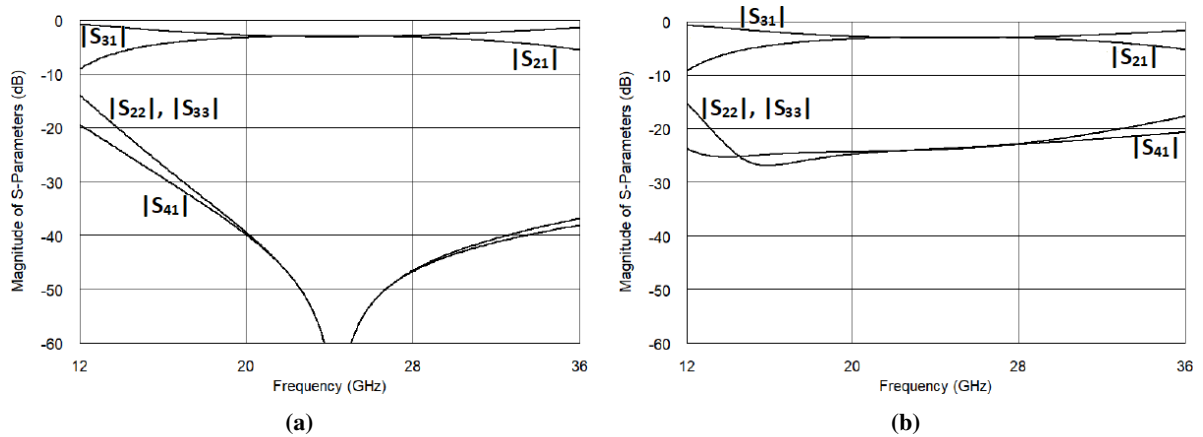
Figure 2.32: The frequency response obtained for the uncompensated left-handed directional coupler in which modal dielectric constants have not been taken into consideration (ideal assumption) (a), and a case in which even and odd modes are respectively ε_e = 8.507, ε_o = 6.645 (practical case) (b). (Copyright © 2019, MDPI)

The most crucial aspect which has to be considered in the case of symmetric coupled-lines is related to the equalization of modal dielectric constants ε_e, and ε_o. For the considered UMS PH25 technology, to obtain a 3-dB directional coupler, widths of edge-coupled lines have to have w_2 = 48 μm, and gap s_2 = 8 μm. Values of the left-handed structure were chosen for the best performance of the directional coupler: L_{LH} = 1.15 nH, and C_{LH} = 0.318 pF. For such a set of parameters, even and odd modes are respectively ε_e = 8.507 and ε_o = 6.645. The calculated frequency response of an uncompensated left-handed directional coupler in which modal dielectric constants are considered is presented in

Fig. 2.32b. As can be seen, an influence of inequality of the modal permittivities has a significant impact on the designed structure. Thus, it has to be taken into account during the design process.
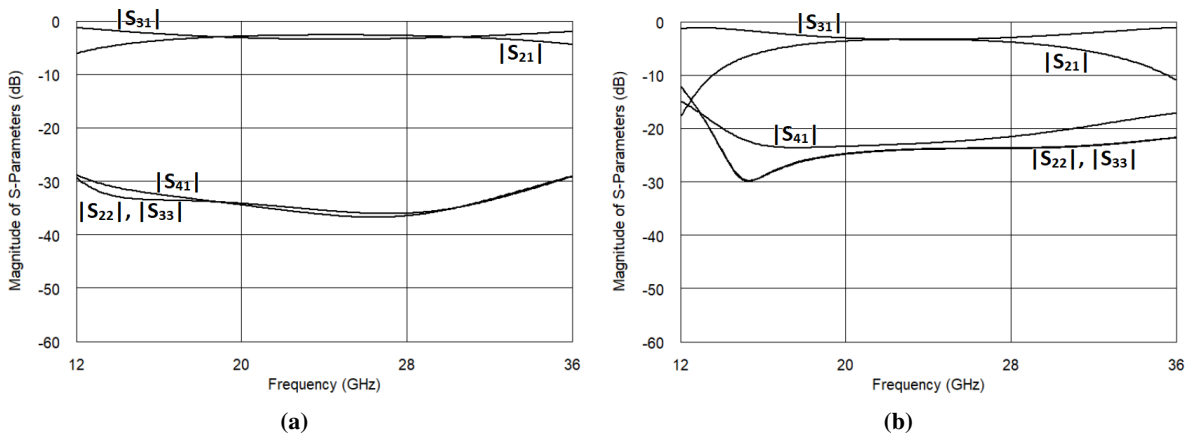
Figure 2.33: Frequency response of compensated left-handed directional coupler obtained during calculations (a) and electromagnetic simulations (b). (Copyright © 2019, MDPI)
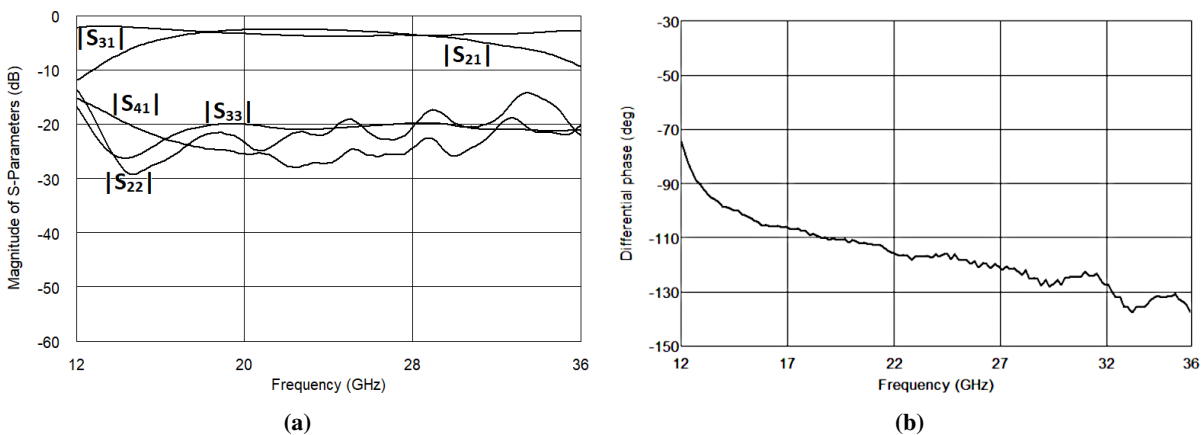
Figure 2.34: Measured S-Parameters (a) and differential phase (b) of fabricated compensated left-handed directional coupler. (Copyright © 2019, MDPI)

To improve the electrical performance of the considered left-handed directional coupler, the compensation method proposed in Subsection 2.2 has been utilized. The structure was recalculated, and the corrected geometry was found: $w_2 = 43$ μm, $s_2 = 8$ μm. The additional, compensating capacitance was also identified and is equal to $C_d = 37.74$ pF/m. The left-handed section was defined by the inductance $L_{LH} = 0.57$ nH, and capacitance $C_{LH} = 0.27$ pF. A calculated response of the compensated left-handed directional coupler is presented in Figure 2.33a and the electromagnetic simulations of the component are shown in Fig. 2.33b. It should be mentioned that compensating elements have been formed between two metallization layers ($M1$, and $M2$), which can be treated as *metal-insulator-metal* (MIM) capacitors. Values of the realized compensation capacitors are $C_{Cm} = 12.6$ fF.

The designed directional coupler was fabricated and was then measured. The obtained results are presented in Fig. 2.34. As can be seen, the measurements are in good agreement with the simulated response of the coupler. The return losses are lower than 20 dB, and the isolation is greater than

25 dB at the center frequency. The imbalance of the differential phase reaches $27°$ at the center frequency, which can be explained by the application of the left-handed section composed of distributed elements that distorted the phase response. Figure 2.35 presents SEM photography of the fabricated compensated left-handed directional coupler. The overall size of the die is 710 x 1216 μm.
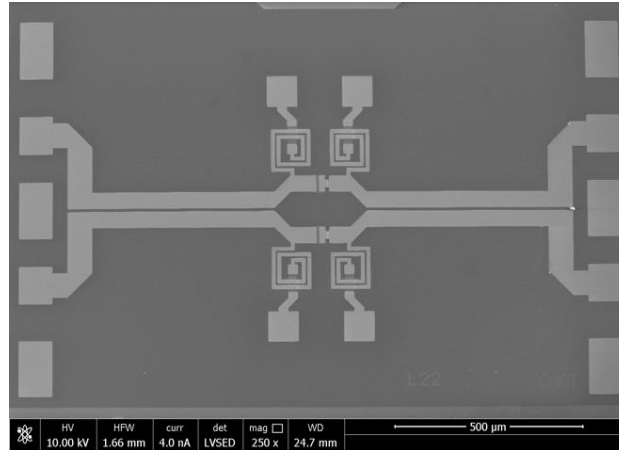
Figure 2.35: SEM photograph presenting fabricated compensated left-handed directional coupler. (Copyright © 2019, MDPI)

2.3. Compensation Methods for Differentially-Fed Directional Couplers Based on a Dielectric Stack-Up Arrangement

In this Section, compensation methods dedicated for differentially excited directional couplers are discussed. It is shown by the author that through the appropriate composition of a substrate stack-up, one can significantly improve the electrical performance of a coupler. Such an approach is in opposition to the methods proposed for single-ended couplers (Sections: 2.1 and 2.2), and for differential excited couplers [107] in which additional compensating elements have to be added. In the first case, a homogeneous medium is considered. It is shown that the equalization of odd and even dielectric permittivities is possible in tandem directional couplers. The second case is focused on an inhomogeneous substrate arrangement in which the equalization of coupling coefficients is achieved through the proper selection of dielectric layers.

2.3.1. Homogeneous Dielectric Stack-up

The simplest form of differentially-fed directional couplers can be realized with the homogeneous stripline technique. For such a case, utilized substrate layers are defined by the same thicknesses h and dielectric permittivities ε_r.

In the symmetric coupled-line section (having equal values of strip widths and the gap between them), the equalization of the modal phase velocities is fulfilled [29]. However, achieving a strong coupling between coupled-lines for 50 Ω impedance is quite difficult due to the geometry of the stack-up. Thus, in [126] the author proposed the use of tandem topology which is well known in single-ended solutions [58].
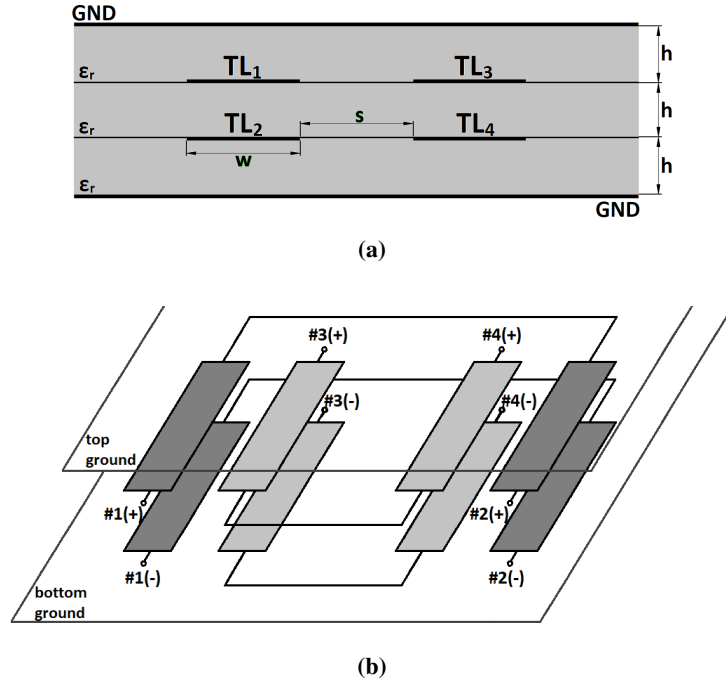
Figure 2.36: Cross-sectional view of homogeneous stripline structure (a), and simplified differentially-fed tandem directional coupler topology (b) [126]. (Copyright © 2019, IEEE)

Figure 2.36b presents a proposed differentially excited tandem coupler designed using the stripline technique. Assuming 3-dB overall coupling for the considered structure, each of the coupled sections has to have coupling of C = 8.34 dB. Differential pairs are formed in an edgewise configuration (corresponding to Fig. 2.36a: TL_1 with TL_2, and TL_3 with TL_4). Whereas coupled pairs operate in a broadside configuration (corresponding to Fig. 2.36a: TL_1 with TL_3 and TL_2 with TL_4). The balanced ports are marked as follows: #1 (+), and #1 (-), #2 (+), and #2 (-), #3 (+), and #3 (-), #4 (+), and #4 (-).

Considering the fact that the directional coupler consist of two identical symmetric coupled-line sections, the analysis presented in Subsection 1.3.2 can be utilized. Firstly, the 4 x 4 per unit-length capacitance matrix of a single coupled-line section has to be numerically found. In the next step, such a matrix has to be reduced to a size of 2 x 2 for optimizing the calculations. The reduced capacitance matrix for differential excitation can be found by using equations 1.62, 1.63 and 1.66. Having calculated such a 2 x 2 matrix representation of the coupled-line section, modal impedances

$$Z_{0e} = \frac{1}{c\sqrt{C_e C_{0e}}} \tag{2.16}$$

$$Z_{0o} = \frac{1}{c\sqrt{C_o C_{0o}}}. \tag{2.17}$$

and effective dielectric constants

$$\varepsilon_{eff(e)} = \frac{C_e}{C_{e0}} \tag{2.18}$$

$$\varepsilon_{eff(o)} = \frac{C_o}{C_{0o}}, \tag{2.19}$$

can be derived. Such a set of parameters is sufficient to design a four-coupled-line section. The last step is to obtain a proper connection between the designed coupled structure, according to the tandem configuration presented in Fig. 2.36b.

The considered differentially-fed 3-dB tandem-connected directional coupler operating at a 1 GHz center frequency was designed using the homogeneous stripline technique. First, the 8.34 dB coupled-line sections were designed. In Fig. 2.36a, a cross section view of the chosen homogeneous stack-up is presented. For such a stratification, the following geometry was identified: $h_1 = 1.5748$ mm, $\varepsilon_{r1} = 6.15$, $w = 0.52$ mm, and $s = 0.14$ mm, where w and s are width and distance between the coupled strips, respectively. Secondly, the designed sections were connected according to the tandem configuration which is presented in Fig. 2.36b. The designed tandem directional coupler has been simulated electromagnetically, and the obtained frequency responses for differential and common-differential modes are presented in Fig. 2.37. Figure 2.38 presents the obtained differential phases.
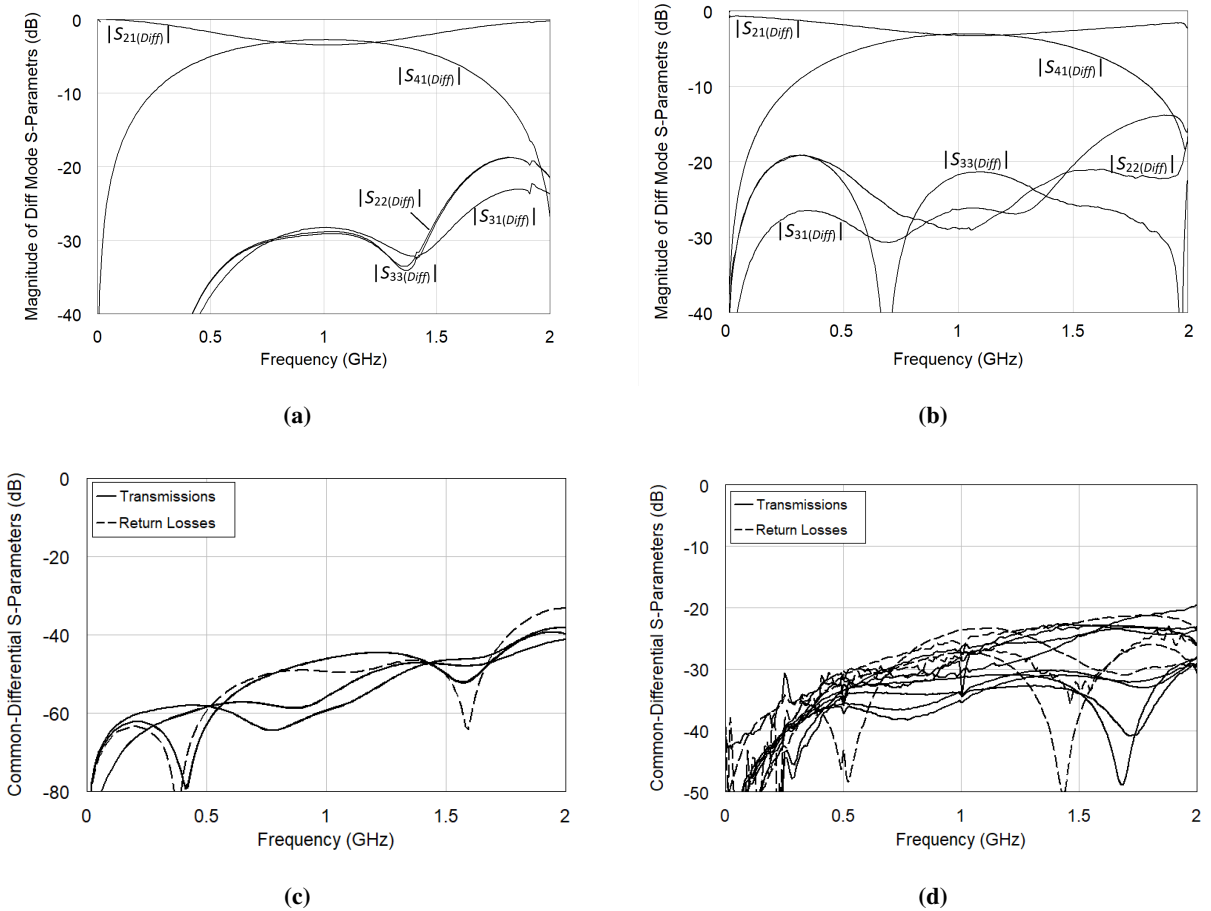
Figure 2.37: Results of electromagnetic simulations (a), (c) and measurements (b), (d) of the considered differentially-fed tandem directional coupler. (Copyright © 2019, IEEE)
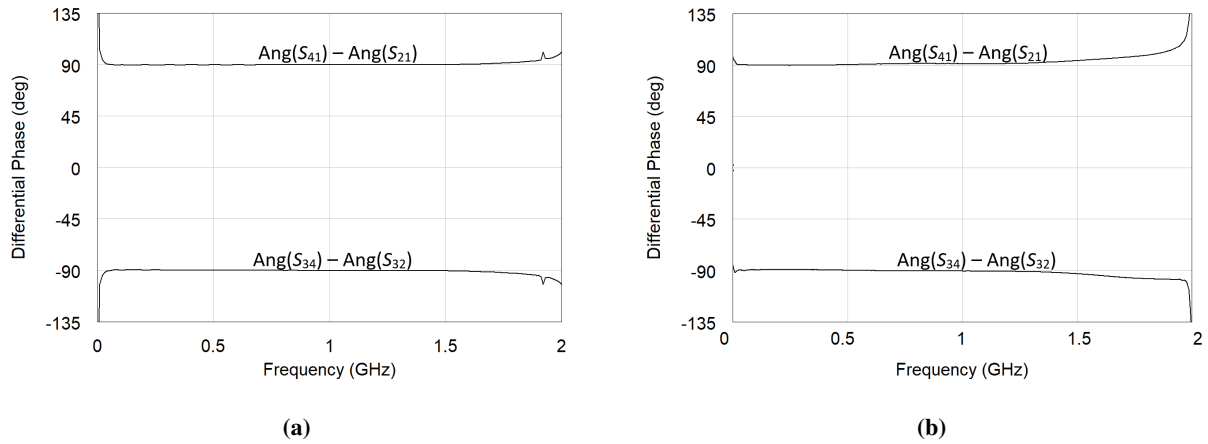
Figure 2.38: Differential phases of the differentially excited tandem directional coupler obtained during electromagnetic simulations (a), and measurements (b). (Copyright © 2019, IEEE)

As can be seen, the measurements are in good agreegment with the simulations results. The measured reflection coefficient is lower than -18.5 dB and the isolation is grearer than 28.7 dB at the 1 GHz center frequency. Moreover, common-to-differential mode conversion losses are lower than -20 in the operational bandwidth of the designed directional coupler. The observed differential phase imbalance does not exceed $1.5°$, which can be observed in Fig. 2.38. The layout and manufactured directional coupler is presented in Fig. 2.39.
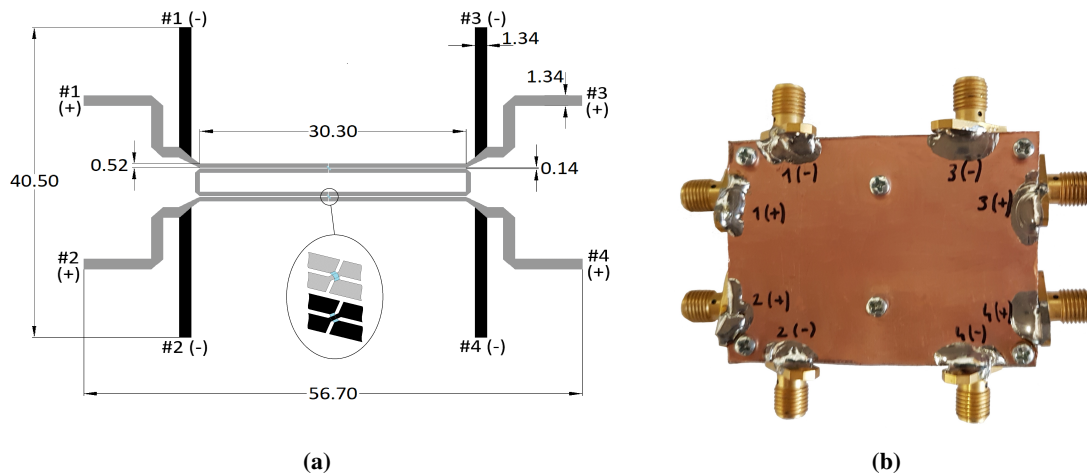
Figure 2.39: Layout of the considered tandem differentially-fed directional coupler (a) (top layer - grey color and bottom - black), and view of fabricated component (b). (Copyright © 2019, IEEE)

2.3.2. Inhomogeneous Dielectric Stack-up

A) Symmetric Differentially-Fed Directional Coupler Designed Using the Inhomogeneous Dielectric Stack-up

In practice, many structures are designed by utilizing an inhomogeneous stratifications of dielectric layers. This approach is often dictated by technological specification including mechanical and electrical

issues or the costs of fabrication. However, such structures feature inequality of modal phase velocities which have a direct impact on electrical performance. Therefore, the development of methods which allow to the design of improved directional couplers is crucial. In [128] the author proposed a novel compensation method which is based on the appropriate composition of substrate layers. Such an approach can be utilized directly in differentially-fed directional couplers to improve their electrical parameters. Furthermore, the developed method corresponds to the technique investigated in other research [9] which is commonly applied for single-ended coupled-line directional couplers.

(a)

(b)
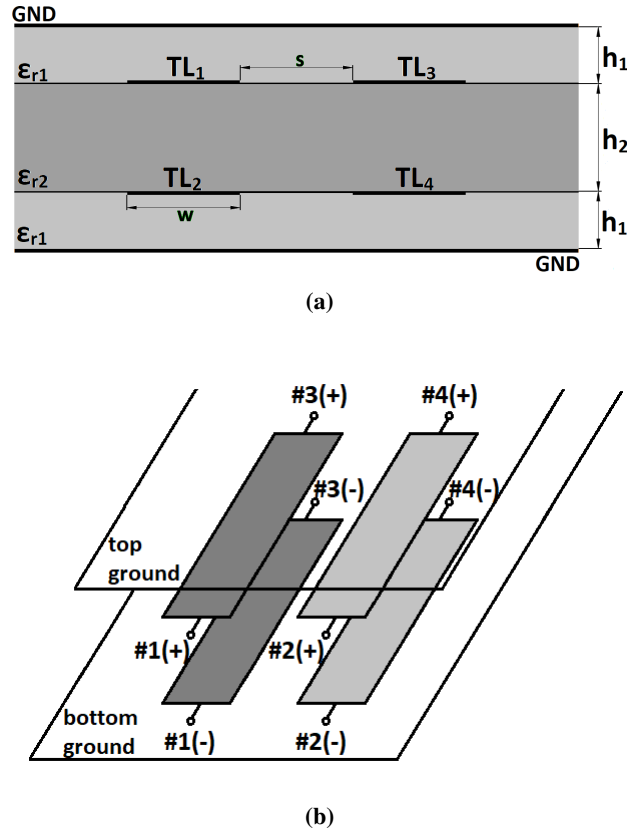
Figure 2.40: Cross-sectional view of inhomogeneous stripline structure (a), and simplified schematic of considered differentially-fed directional coupler (b) [128]. (Copyright © 2019, Wiley)

The stripline technique was chosen to achieve a symmetrical coupled structure. A cross-sectional view is presented in Fig. 2.40a. As can be seen, the top and bottom substrates are the same, and are characterized by the height h_1 and the dielectric permittivity ε_{r1}. The center layer is defined by the thickness h_2 and the dielectric permittivity ε_{r2}. Utilizing such a stack-up, the four-coupled-line section, which is differentially excited in a broadside configuration has been analyzed. A schematic of the considered directional coupler with marked ports is presented in Fig. 2.40b. For further analysis, a 8-dB coupler was chosen. The parameters of such a component i.e. odd, even characteristic impedances Z_{0o}, Z_{0e} and modal effective dielectric permittivities $\varepsilon_{eff(e)}, \varepsilon_{eff(o)}$ were numerically derived using the same method as that presented in Subsection 2.3.1. For such a case, the influence of even and odd effective permittivities for differential excitation in a wide range of dielectric layer thickness ratio h_2/h_1 has been calculated and is presented in Fig. 2.41.
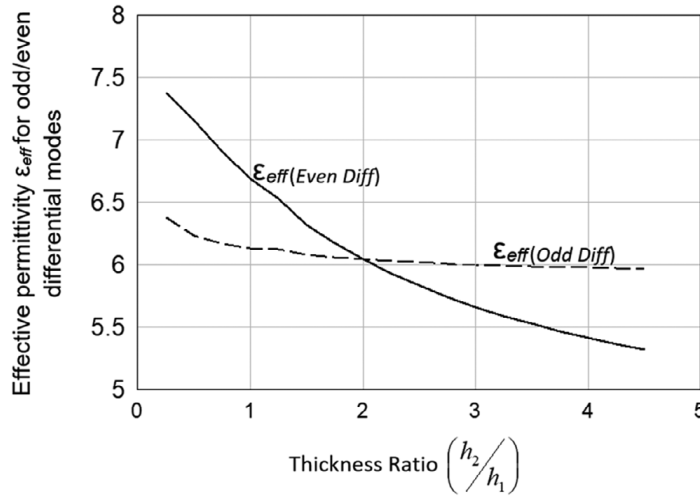
Figure 2.41: Characteristics of effective permittivity changes for odd and even differential mode vs. changes of thickness ratio h_2/h_1. Results obtained for a stripline 8-dB coupled-line section in which $\varepsilon_{r1} = 2.5$, and $\varepsilon_{r2} = 10.2$, $h_1 = 0.762$ mm [128]. (Copyright © 2019, Wiley)

From the obtained results, it can be seen that when the middle dielectric layer is thinner than the outer layers, the differential even-mode effective permittivity $\varepsilon_{eff(e)}$ is larger than the odd-mode effective permittivity $\varepsilon_{eff(o)}$. The observed difference decreases as the thickness of the middle layer increases. However, it can also be seen that when the middle layer is much thicker than the outer layers, the differential odd-mode effective permittivity is larger than the even-mode effective permittivity. Both permittivities are equal at the point in which $h_2/h_1 = 2$, which constitutes the condition for effective permittivity equalization, and therefore, for modal phase velocity equalization.

To verify correctness of the proposed compensation method, the differentially-fed 8.34-dB coupled-line section operating at the 1 GHz center frequency was designed. A cross-sectional view of the chosen substrate stack-up is presented in Fig. 2.40a. To obtain the compensation effect, thicknesses of the layers fulfill relation $h_2 = 2h_1$. The chosen stratification of a four-strip coupled-line section is: $h_1 = 0.762$ mm, $h_2 = 1.524$ mm, $\varepsilon_{r1} = 2.5$, $\varepsilon_{r2} = 10.2$, width $w = 0.37$ mm, and distance between coupled-strips $s = 0.1$ mm. The following 4 x 4 capacitance matrix of the considered structure is calculated:

$$[C] = \begin{bmatrix} 167.0 & -18.4 & -86.5 & -12.2 \\ -18.4 & 167.0 & -12.2 & -86.5 \\ -86.5 & -12.2 & 167.0 & -18.4 \\ -12.2 & -86.5 & -18.4 & 167.0 \end{bmatrix} \left[\frac{pF}{m}\right], \tag{2.20}$$

and the corresponding matrix calculated for the vacuum is

$$[C_0] = \begin{bmatrix} 27.6 & -1.52 & -12.7 & -1.01 \\ -1.52 & 27.6 & -1.01 & -12.7 \\ -12.7 & -1.01 & 27.6 & -1.52 \\ -1.01 & -12.7 & -1.52 & 27.6 \end{bmatrix} \left[\frac{pF}{m}\right]. \tag{2.21}$$

By using equations 1.62 and 1.63, the electrical parameters of the compensated coupled-line section were identified: $\varepsilon_{eff(e)} = \varepsilon_{eff(o)} = 6.35, Z_{0e} = 152$ Ω, $Z_{0o} = 64.8$ Ω which gives an overall coupling coefficient of the structure of $k = 0.4$ ($C = 7.92$ dB), and characteristic impedance $Z_0 = 99.24$ Ω.
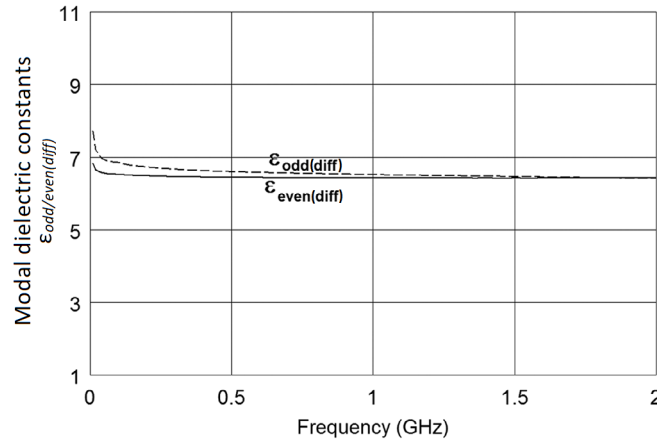
Figure 2.42: Calculated modal relative dielectric constants vs. frequency. (Copyright © 2019, Wiley)
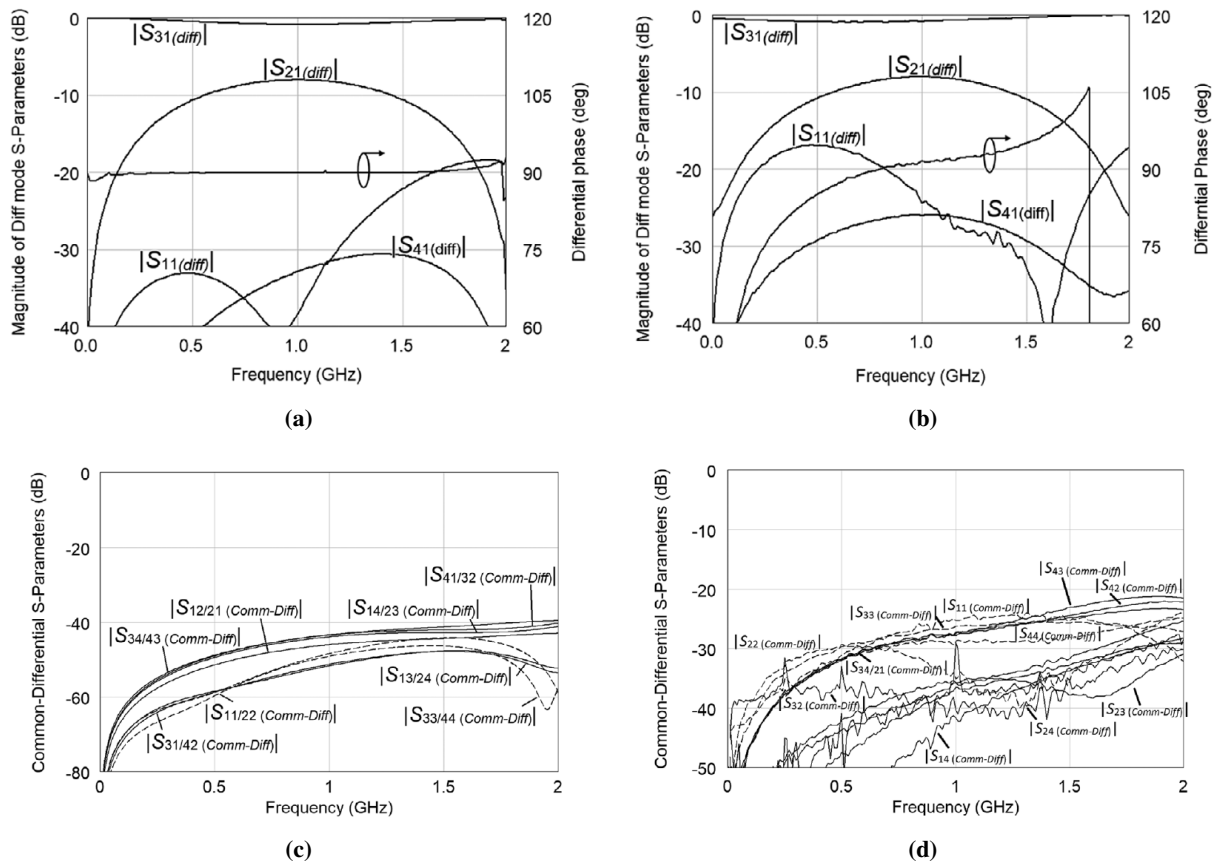
Figure 2.43: Results of electromagnetic simulations (a), (c) and measurements (b), (d) of the considered differentially-fed directional coupler designed with inhomogeneneous stratification. (Copyright © 2019, Wiley)

Figure 2.42 shows changes of modal permitivity in the frequency range calculated for an electromagnetic model of the considered directional coupler. It can be seen that the obtained values are

almost equal in the wide frequency range, and are nearly constant. Results of electromagnetic simulations are presented in Fig. 2.43.

(a)

(b)
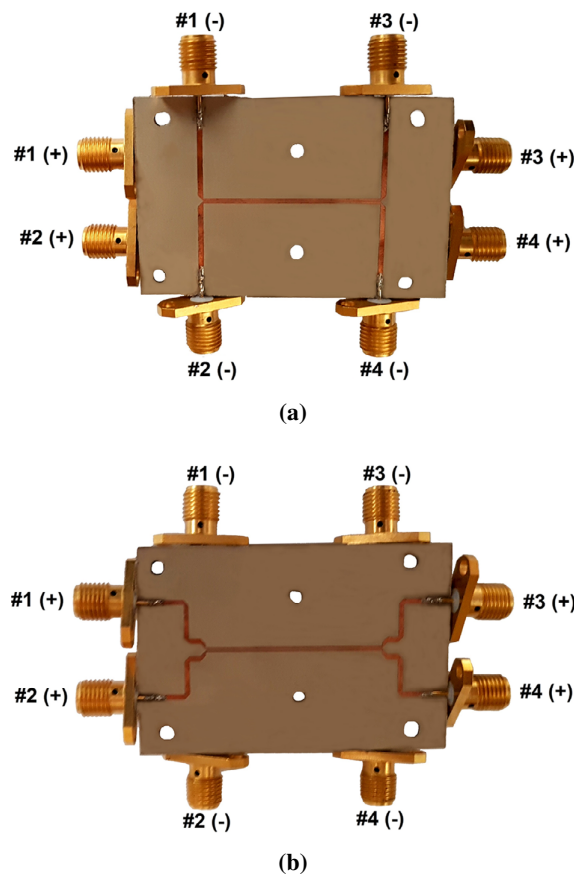
Figure 2.44: Top view (a), and bottom view (b) of the manufactured 8.34-dB differentially-fed directional coupler. (Copyright © 2019, Wiley)

The designed differentially-fed directional coupler has been manufactured and subsequently measured. The collected results of measurements are presented in Fig. 2.43, where they are compared with results of simulations. The observed isolation is greater than 26 dB in the operational bandwidth. The measured return losses are lower than 17 dB. The differential phase imbalance in not grater than 5° in the frequency range of 0.5 GHz to 1.5 GHz. The common-to-differential mode conversion losses are lower than -20 dB in the operational bandwidth. The pictures of the fabricated differentially-fed directional coupler are presented in Fig. 2.44.

B) Asymmetric Differentially-Fed Directional Coupler Utilized in a Inhomogeneous Structure

The investigation on the design of symmetrical differentially-fed directional couplers gives an answer as to how the stripline structures can be improved. However, in [45], the author proposed a method focusing on the equalization of inductive and capacitive coupling coefficients in a differentially excited directional coupler composed of asymmetric conductors. The stack-up utilized in the proposed solution is presented in Fig.2.45a. As can be observed, the stratification presents a multilayer microstrip structure in which four specific layers can be seen. At the very bottom, a base substrate with thickness h_4 and

dielectric permittivity ε_{r4} is used. The traces of the coupler are etched on a layer specified by h_2 and ε_{r2}. Moreover, two additional layers are present, among which, the layer with thickness h_3 and permittivity ε_{r3} is a technological layer bonding the two mentioned layers h_4 and h_2 together, while the top layer is a compensating layer.
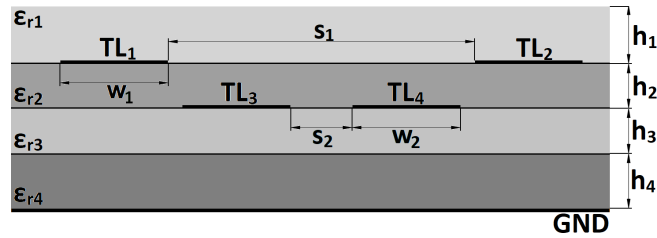
(a)
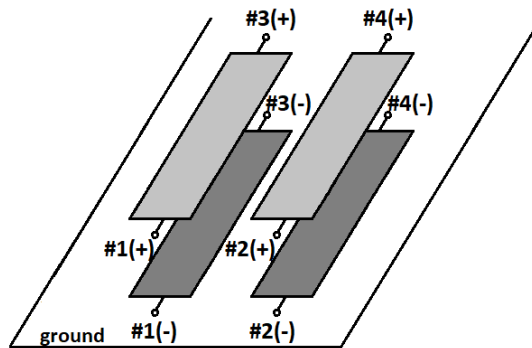
(b)

Figure 2.45: Cross-sectional view of multilayer microstrip stack-up (a), and conceptual circuit of differentially-fed directional coupler utilized in inhomogeneous stratification (b) [45]. (Copyright © 2020, MDPI)

(a)   (b)
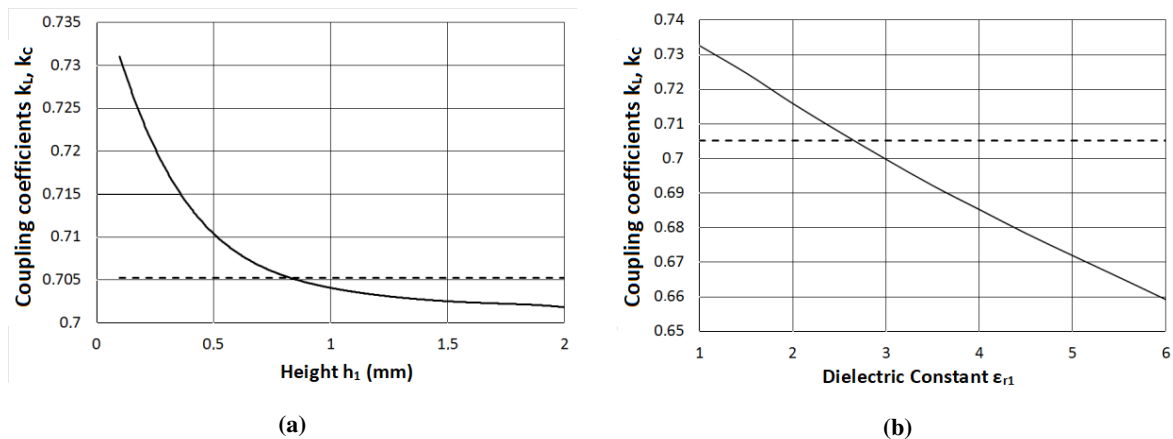
Figure 2.46: Calculated inductive k_L (dashed lines) and capacitive k_C (solid lines) coupling coefficients obtained for the considered 3-dB differentially-fed coupled section in which the following parameters were chosen: $h_4 = 0.76$ mm, $\varepsilon_{r4} = 4.5$, $h_3 = 0.09$ mm, $\varepsilon_{r3} = 3.38$, $h_2 = 0.05$ mm, $\varepsilon_{r2} = 3.4$. Calculations results obtained for changes of the thickness h_1 assuming dielectric constant $\varepsilon_{r1} = 2.5$ (a), and the dielectric constant ε_{r1} assuming that $h_1 = 0.787$ (b) [45]. (Copyright © 2020, MDPI)

The considered directional coupler consisting of four-coupled lines is differentially excited in an edgewise configuration. A simplified circuit schematic is presented in Fig. 2.45b. To verify the influence

of a compensating layer on the couplers' electrical performance, a 3-dB coupled section was investigated. The 4 x 4 per-unit-length inductive and capacitive matrices of a structure were found numerically. Subsequently, the obtained matrices were reduced to a size of 2 x 2 using the method presented in [64]. Finally, the geometry of the coupled structure was iteratively optimized to obtain the required coupling coefficients and characteristic impedances of the conductor pairs. For this case, changes of inductive and capacitive coupling coefficients k_L, k_C vs height h_1 and dielectric permittivity ε_{r1} have been calculated and are presented in Fig. 2.46. As can be seen, both the thickness and the dielectric constant of the compensation layer influences the capacitive coupling coefficient k_C. The inductive coupling coefficient k_L is not influenced by the thickness and the dielectric constant of the compensation layer because it depends only on the geometry of the conductor and can be calculated from the capacitive matrix of the homogeneous air-filled geometry (which is not dependent upon any dielectric properties). The application of the additional dielectric layer lowers the capacitive coupling coefficient and it is required to adjust the parameters h_1 and ε_{r1} to obtain equality of both inductive and capacitive coefficients.
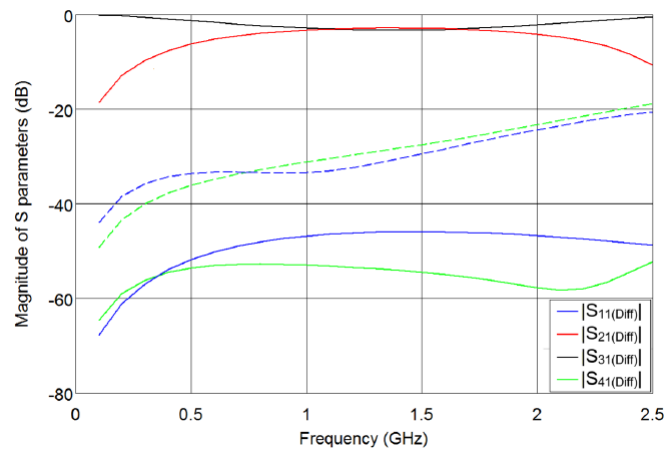
Figure 2.47: Calculated scattering parameters of a four-strip coupled-line section operating in a differential mode for two cases: uncompensated structure (dashed lines) and compensated one (solid lines). (Copyright © 2020, MDPI)
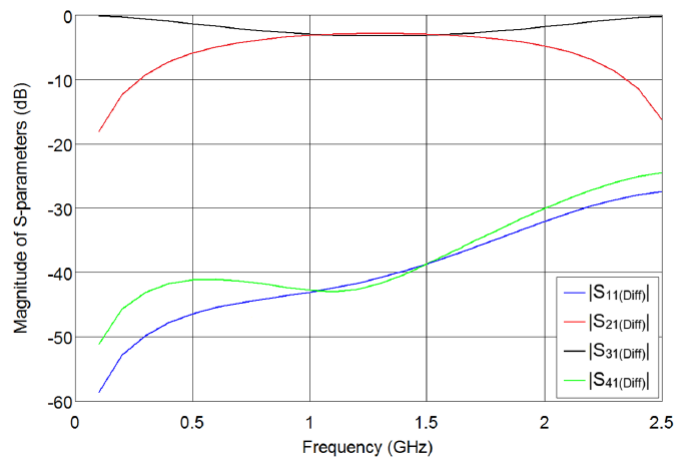
Figure 2.48: Results obtained during electromagnetic simulations of the 3-dB asymmetric differentially-fed directional coupler. (Copyright © 2020, MDPI)

For the investigated stratification, a 3-dB differentially-fed coupled-line directional coupler operating at the center frequency of 1.4 GHz was designed. Due to the fact that the considered topology consists of an asymmetric coupled-line section, the coupling coefficient has to be equalized to improve the overall electrical parameters of the directional coupler. The parameters of the stack-up and geometry of the structure are as follows: $h_4 = 0.76$ mm, $\varepsilon_{r4} = 4.5$, $h_3 = 0.09$ mm, $\varepsilon_{r3} = 3.38$, $h_2 = 0.05$ mm, $\varepsilon_{r2} = 3.4$, $w_1 = 0.345$ mm, $s_1 = 1$ mm, $w_2 = 0.315$ mm, $s_2 = 0.6$ mm. According to Fig. 2.46, the compensating layer has be 0.787 mm thick and have a dielectric constant of $\varepsilon_{r1} = 2.5$.

Calculations of the coupled section are presented in Fig. 2.47, where two cases are considered with and without the additional compensating layer. As can be seen, the compensating layer can significantly improve return losses, and isolation. Figure 2.48 shows electromagnetic simulations obtained for the entire compensated directional coupler in which additional signal lines between 50 Ω external ports, and the coupled section are taken into account.

(a) **(b)**
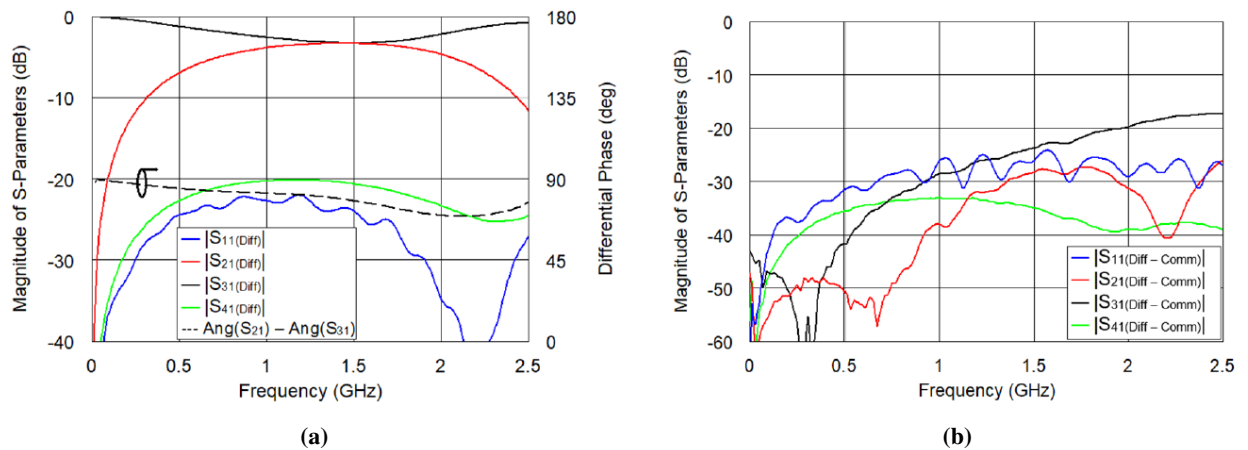
Figure 2.49: Measured magnitudes of scattering parameters (solid lines) and differential phase (dashed lines), and differential-to-common mode S-Parameters (b) of the considered 3-dB compensated asymmetric differentially-fed directional coupler. (Copyright © 2020, MDPI)
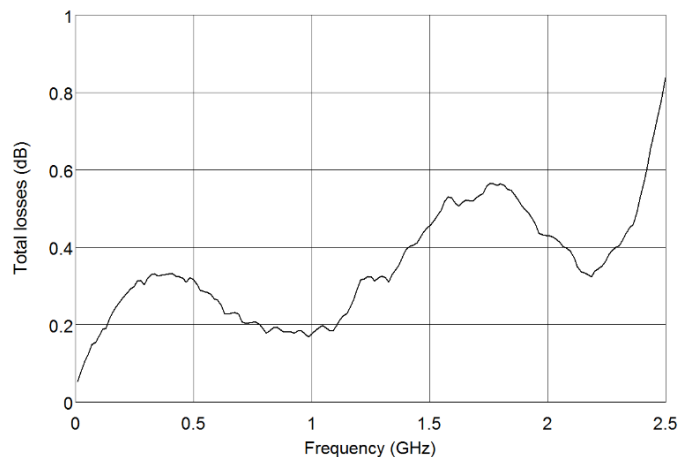
Figure 2.50: Calculated total losses obtained for the fabricated 3-dB differentially-fed asymmetric coupled-lines directional coupler. (Copyright © 2020, MDPI)

The designed 3-dB differentially-fed coupler has been fabricated and subsequently measured. The results are presented in Fig. 2.49. The obtained return losses are not greater than 22 dB, and isolation is better than 20 dB in the operational bandwidth of the directional coupler. The common-to-differential conversion losses are not greater than 25 dB at the center frequency. The obtained total losses do not exceed 0.4 dB at the center frequency. The fabricated 3-dB differentially-fed directional coupler is shown in Fig. 2.51.

(a)   (b)
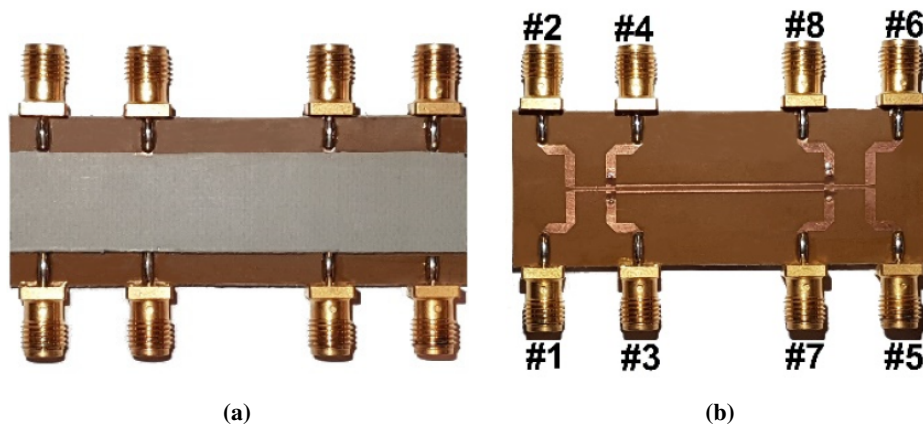
Figure 2.51: Fabricated compensated 3-dB differentially-fed directional coupler (a), and uncompensated version in which the top compensating layer has been removed (b). (Copyright © 2020, MDPI)

2.4. Conclusions

In this chapter, the compensation methods utilized in directional couplers based on symmetric and asymmetric coupled-line sections have been proposed. The proposed compensation methods are based on two strategies. The first strategy uses additional compensating elements such as lumped, quasi-lumped capacitors or open-ended stubs placed periodically along the coupled section. The second strategy is based on the proper stratification of a chosen substrate stack-up.

In Section 2.1, two compensation methods utilized in low-loss directional couplers have been presented. It has been proven, that in a simple coupled-line section consisting of strips which are at a relatively large distance from each other, the additional compensation open-ended stubs can improve electrical performance. However, in the case of microstrip structures in which a strong coupling coefficient is required (such as Lange configuration), the space between the lines is too small for compensating lumped or quasi-lumped capacitances. Therefore, a method based on a proper suspended microstrip stratification has been investigated in which an additional layer has been introduced.

In Section 2.2, a compensation method which can be utilized in monolithic directional couplers has been studied. The proposed strategy assumes the use of only additional mutual capacitances between coupled-lines. Such an approach significantly simplifies the design method and the physical realization, which is a crucial aspect in monolithic technologies. To verify the applicability of such compensation, three types of directional couplers were designed and measured: a three-strip coupled-line structure, Lange topology and a directional coupler consisting of a left-handed section.

Section 2.3 is fully dedicated to compensation methodologies utilized in differentially-fed directional couplers designed in homogeneous and inhomogeneous substrate stratifications. Furthermore, a compensation in symmetric and asymmetric coupled-line sections based on inhomogeneous substrate stack-ups have been investigated. It has been proven that a complex structure such as a tandem configuration can be utilized as a differentially excited directional coupler in homogeneous stratification. Furthermore, it has been shown that equalization of modal phase velocities in a symmetric coupled-line section using an inhomogeneous stripline technique can be fulfilled by achieving the proper ratio between the thicknesses of the substrate layers, which is equal to two. Finally, an additional compensation layer can equalize inductive and capacitive coupling coefficients in asymmetric differentially-fed couplers.

3. Impedance Transforming Directional Couplers

Ensuring the lowest possible return losses is crucial for achieving good electrical performance of the microwave components. Such an approach is fulfilled in systems composed of elements with the same port impedances. However, circuits such as balanced amplifiers or mixers consist of non-linear elements of different impedances than passive power combiners. Therefore, to achieve a proper impedance match, impedance matching networks and transformers are commonly utilized [109]. However, such an approach brings some disadvantages. First, the occupied area of the designed device increases with the number of additional matching elements. This is a crucial aspect in monolithic applications, where the dimensions of chips are limited by technological constrains. Moreover, matching networks based on lumped elements introduce additional insertion losses. Finally, the majority of known solutions feature a narrow-band frequency response and the synthesis of broadband networks can be difficult. Cristal [24] proposed a novel approach to an asymmetric coupled-line section which is an optimal solution to the a fore mentioned issues and it gave rise to a new class of directional couplers named impedance transforming couplers. However, most of reported solutions have a limited impedance-transforming ratio, limited operational bandwidths and are typically large.

This chapter begins with an introduction to impedance transforming directional couplers consisting of the single coupled-line section presented in Section 3.1. To reduce the required coupling and increase the impedance transforming ratio, a novel tandem coupler is proposed. In the second Section 3.2, a new design approach to rat-race couplers is shown. The author proposes two topologies featuring narrow and broadband responses. Moreover, a low-loss version of a broadband impedance-transforming rat-race coupler is also presented. The chapter ends with experimental verification of the proposed solutions.

In this part of the thesis, the author cites his investigation of impedance transforming directional couplers published in three papers [124], [123], [125].

3.1. Impedance-Transforming Directional Couplers Based on Coupled-Line Sections

In this section, impedance-transforming directional couplers based on coupled-line sections are shown. The first subsection is focused on a short introduction to a single coupled-line section featuring impedance transformation. In the second subsection, the novel tandem-connected coupler is presented, which is described in the literature [125]. It is shown, that the proposed structure features greater impedance transformation than existing solutions.

3.1.1. Single Impedance-Transforming Coupled-Line Section

The impedance transforming directional coupler was reported for the first time in [24] and was a simple coupled asymmetric two-transmission-line section as presented in Fig. 3.1. In the proposed idea, the transmission-lines have the same impedances as loads: $Z_{T1} = Z_{T3} = Z_{L1}$ and $Z_{T2} = Z_{T4} = Z_{L2}$. Such a concept was further developed in [3] and [4] where both transmission-lines were treated as quarter-wave transformers and were used to form a symmetric coupled-line section. For such a case, the following impedance relations between terminations are assumed: $Z_{T1} = Z_{T2}$ and $Z_{T3} = Z_{T4}$. However, in comparison with the work [24], the obtained frequency response is narrower.
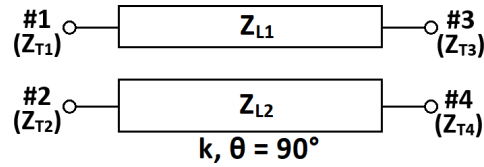
Figure 3.1: Concept view of asymmetric coupled-line section utilized as impedance-transforming directional coupler.

The impedance-transforming ratio R is a crucial factor defining the ratio between loads connected to the coupler and which has to be taken into account during the design of the considered type of directional coupler. For the asymmetric structure proposed by Cristal, such a factor is defined as:

$$R = \frac{Z_{T1}}{Z_{T2}} = \frac{Z_{T3}}{Z_{T4}} = \frac{Z_{L1}}{Z_{L2}}, \tag{3.1}$$

and depends upon coupling coefficient k of the coupled-line section:

$$R = \frac{1}{k^2}. \tag{3.2}$$

Therefore, according to equation 3.2, for the 3-dB directional coupler composed of such an asymmetric coupled-line section, the impedance ratio R is 2, which can be defined as the Cristal criterion. Another approach reported in the literature is focused on utilizing quarter-wave impedance transformers in an asymmetric structure [159]. In such a case, terminations Z_{T2} and Z_{T3} are equal, and Z_{T4} is related with R factor as follows:

$$Z_{T4} = \frac{Z_{T2}}{R}. \tag{3.3}$$

$$Z_{T1} = \frac{Z_{T3}}{R} \tag{3.4}$$

It has to be mentioned that the considered cases have one octave frequency response. To enhance the operational bandwidth, a multisection coupler as that reported in [160] can be utilized.

3.1.2. Impedance-Transforming Tandem Directional Coupler

The ideas mentioned in the previous subsection are focused on single-section structures in which the maximum impedance transforming ratio is limited by the Cristal criterion 3.2. To achieve a greater

value of the R factor, left-handed structures such as that presented in the literature [130] can be utilized. However, such an approach brings additional losses to the circuit and increases complexity of the design. Moreover, obtaining high coupling can be difficult. Such a situation is commonly meet in monolithic technology, where minimum gap between strips is limited and determines the maximum coupling between them. To reduce the required coupling coefficient of the coupled-line section and therefore, make it more realizable, the well-known tandem-connected topology can be utilized [59]. Such an approach was investigated in [125].
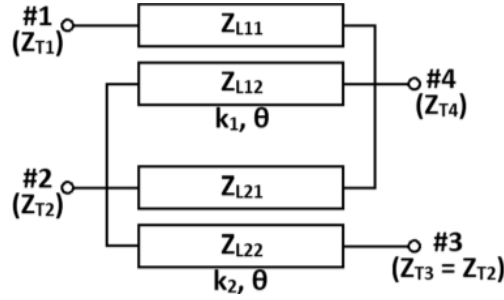
Figure 3.2: Concept of the impedance-transforming directional coupler based on the tandem connection of two asymmetric coupled-line sections with different couplings [125]. (Copyright © 2018, IEEE)

A view of the proposed impedance-transforming tandem directional coupler is presented in Fig. 3.2. It can be seen, that the proposed solution consists of two asymmetric coupled-line structures. Furthermore, it must to be assumed that the terminating impedances of ports: #2 and #3 are equal. Thus, the impedance transforming ratio can be defined as:

$$R = \frac{Z_{T1}}{Z_{T2}}. \tag{3.5}$$

Because both coupled-line sections have to transform the impedance in the same way, similarly as the networks described in [160], we have:

$$R^2 = \frac{Z_{T1}}{Z_{T4}}. \tag{3.6}$$

As can be seen in Fig. 3.2, the proposed solution can be treated as a two-section impedance transformer. Therefore, characteristic impedances $Z_{Li,j}$ $i,j = 1,2$ have to be found by using a well-known theory of two-section transformers, which has been cited, for example in [160]. It can be seen that terminating impedance Z_{T1} is transformed to Z_{T2} by the coupled-line of the first section having a value of Z_{L11}, and the second section with a value of Z_{L21}. Impedance Z_{T4} is transformed in to Z_{T3} (equal to Z_{T2}) by the transmission-lines Z_{L12}, and Z_{L22}. Moreover, both coupled-line sections are quarter-wave. Assuming that the hybrid directional coupler is considered ($k = 0.707$), and the coupler transforms high impedance into low impedance $Z_{T1} > Z_{T2}$ then the lines have to meet the following condition:

$$Z_{L11} > Z_{L21} > Z_{L22} > Z_{L12}. \tag{3.7}$$

Due to fact, that Z_{L11} and Z_{L12} form the first coupled-line section, and impedances Z_{L21} and Z_{L22} form the second section, there are two conditions which limit the achievable impedance transformation ratio:

$$\frac{1}{k_1^2} \geq \frac{Z_{L12}}{Z_{L11}} \qquad (3.8)$$

$$\frac{1}{k_2^2} \geq \frac{Z_{L22}}{Z_{L21}}. \qquad (3.9)$$

It can be seen that the relation 3.8 is harder to obtain. Thus, to maximize the transformation ratio R, the coupled-line section defined by coupling k_1 should operate at the maximum achievable transformation ratio, while the second coupled-line section with k_2 has to ensure the required, overall coupling k of the designed impedance transforming tandem coupler. Thus, coupling k_1 has to be calculated as:

$$k_1 = \frac{Z_{12}}{Z_{L11}}, \qquad (3.10)$$

whereas k_2 has to be calculated by using the equation derived for the tandem coupler:

$$k_2^2 - 2k\sqrt{1 - k_1^2}k_2 + k^2 - k_1^2 = 0. \qquad (3.11)$$

Having calculated values of characteristic impedances $Z_{Li,j}$, and couplings k_1 and k_2, both coupled-line sections can be designed as presented in the literature [158].

It should be mentioned that the maximum value of the R factor is achieved when the calculated coupling is as follows:

$$k_2 = \frac{Z_{L22}}{Z_{L21}}. \qquad (3.12)$$

The proposed tandem-connected directional coupler has been analyzed and the obtained calculations for the overall coupling $k = 0.75$ are listed in Table 3.1.

Table 3.1: Maximum achievable impedance-transforming ratio and coupling coefficients of the proposed impedance transforming tandem-connected coupler in terms of return loss variations. Values calculated for overall coupling $k = 0.75$ ($C = 3$ dB).

Return Losses	R	k_1	k_2
30	7.8	0.218	0.588
25	7.7	0.223	0.584
20	7.6	0.232	0.576
15	7.1	0.251	0.560
10	6.7	0.282	0.533

Analyzing Table 3.1 is clearly seen that factor R is directly related to the return losses of the coupler. Moreover, it can be seen that the calculated coupling coefficient of the coupled-line sections is relatively weak. Therefore, such a structure can be designed as a composition of simple two-coupled-line sections.

The proposed impedance-transforming tandem-connected coupler has been designed to verify the feasibility of the proposed solution. The coupler with coupling $k = 0.75$ has been matched to the terminating impedances $Z_{T1} = 50\ \Omega$ and $Z_{T2} = 10\ \Omega$, which corresponds to the transforming ratio $R = 5$. The utilized substrate stratification is presented in Fig. 3.3. The electrical parameters together with the geometry calculated in the Linpar software are presented in Table 3.2 and Fig. 3.4 shows the ideal response of the proposed tandem coupler.
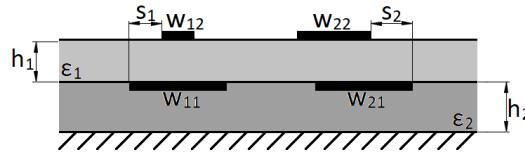
Figure 3.3: Cross-sectional view of substrate stratification utilized for the design of the proposed impedance-transforming tandem directional coupler [125]. (Copyright © 2018, IEEE)

Table 3.2: Calculated geometry and electrical parameters of the proposed impedance-transforming tandem-connected coupler with an overall coupling of $k = 0.75$.

Geommetry	Value	Electrical Parameter	Value
$w_{11}[mm]$	9.0	$Z_{L11}[\Omega]$	3.1
$w_{12}[mm]$	1.0	$Z_{L12}[\Omega]$	33.6
$s_1[mm]$	4.1	k_1	0.3
$w_{21}[mm]$	3.5	k_{L1}	0.31
$w_{22}[mm]$	3.1	k_{C1}	0.29
s_2	1.1	$Z_{L21}[\Omega]$	6.4
$h_1[mm]$	0.225	$Z_{L22}[\Omega]$	15.92
ε_r	3.38	k_2	0.507
		k_{L2}	0.503
		k_{C2}	0.512
		$Z_{T1}[\Omega]$	50
		$Z_{T2,T3}[\Omega]$	10
		$Z_{T4}[\Omega]$	2

Due to fact that transition regions between the coupled-line sections and signal lines introduce parasitic reactances which deteriorate its frequency response, additional lumped capacitors marked in Fig. 3.6 as C_1, C_2, C_3 and C_4 have been connected to improve the electrical performance of the coupler. The obtained simulations together with measurements are presented in Fig. 3.5. As can be noticed, the measurement results are in good agreement with the simulations. Isolation of the fabricated coupler is greater than 18.5 dB, and return losses are not less than -17.7 dB at the center frequency. Moreover,

insertion losses are at the level of 0.6 dB, whereas differential phase imbalance is not greater than 6.8° at the center frequency. The picture of the fabricated impedance-transforming tandem coupler is presented in Fig. 3.6.
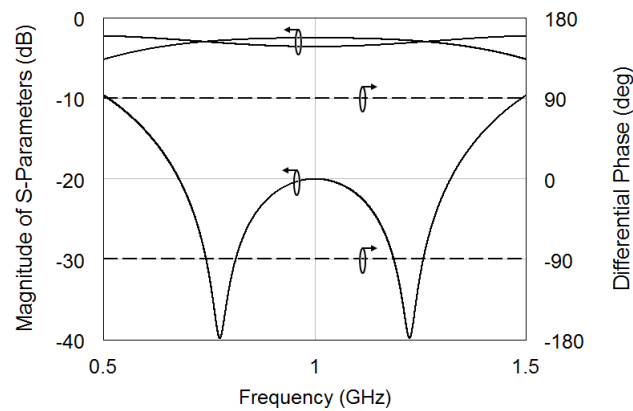
Figure 3.4: Frequency response of the ideal impedance-transforming tandem directional coupling with the electrical parameters presented in Table 3.2 [125]. (Copyright © 2018, IEEE).

(a)   **(b)**
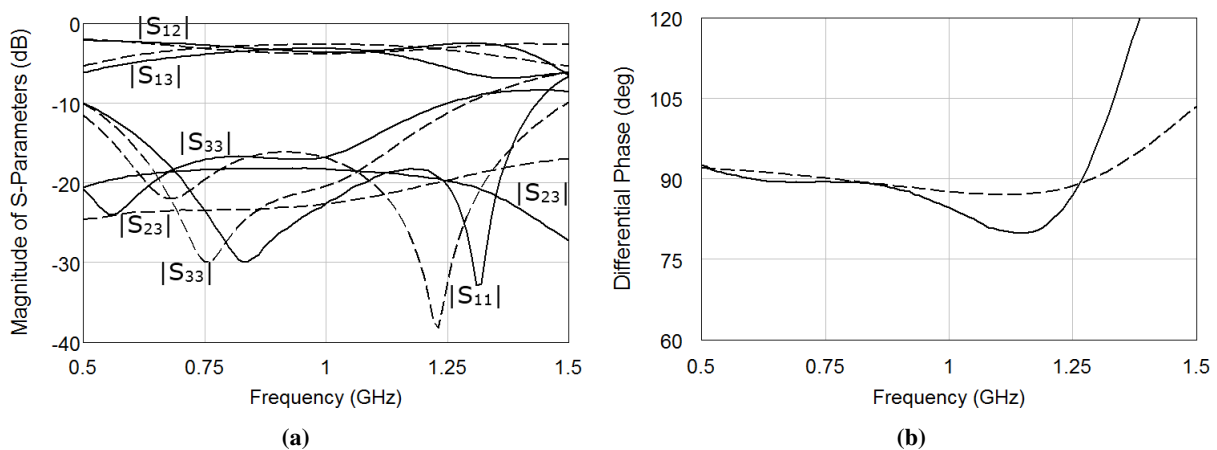
Figure 3.5: Results obtained during electromagnetic simulations (dashed lines) and measurements (solid lines) of the proposed impedance-transforming tandem-connected directional coupler [125]. (Copyright © 2018, IEEE).

(a)   **(b)**
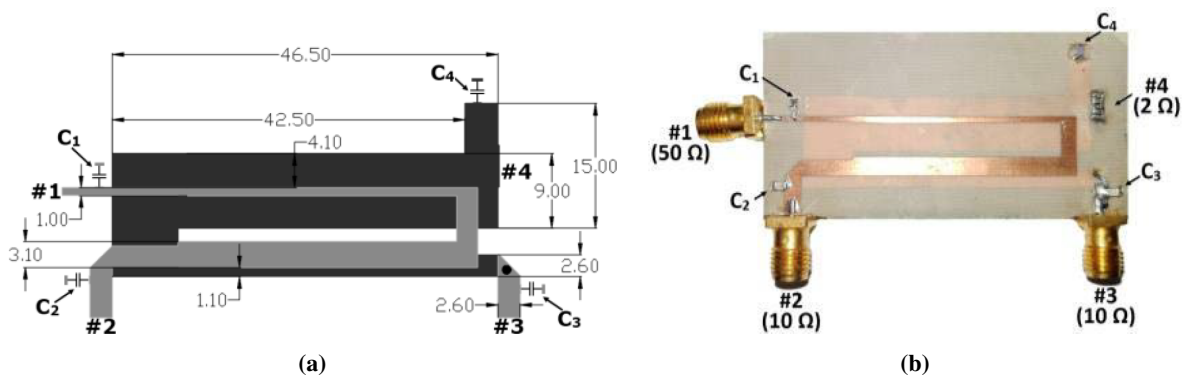
Figure 3.6: Layout (a) and photograph (b) of the fabricated impedance-transforming tandem directional coupler [125]. (Copyright © 2018, IEEE).

3.2. Impedance-Transforming Directly Connected-Line Couplers

In this section, impedance-transforming directional couplers based on directly connected topologies are presented. The first subsection presents a brief state-of-the-art review of solutions based on branch-line couplers. The second subsection describes novel impedance-transforming narrow and broadband rat-race couplers which were proposed in [124]. It is shown that the classic rat-race topology features a theoretically not-limited impedance transformation. Furthermore, to enhance its operational bandwidth, the broadband solutions are also shown. The last subsection presents a low-loss version of the broadband impedance-transforming rat-race coupler shown in Subsection 3.2.2, which has been proposed by the author in [123].

3.2.1. Impedance-Transforming Branch-Line Couplers

Obtaining a strong coupling of coupled-line sections can be difficult in some applications due to physical limitations, especially the minimum gap between transmission lines. Such an issue is commonly met in monolithic processes. Therefore, directly connected transmission-line topologies have to be considered. Due to the simplicity of the design, quadrature hybrid couplers featuring impedance transformation are commonly utilized as the combining element in balanced circuits such as microwave amplifiers [103], [114], [110]. The proposed solutions are based on the classic branch-line topology which significantly reduces the operational bandwidth of the devices. To enhance the frequency band, multisection circuits can be designed as shown in the literature [77], [76]. However, such approaches increase the overall size of the component. In terms of size reduction, three main ideas are known to have been reported. In first idea, all transmission-lines are replaced by sections composed of lumped elements [115]. The second method assumes the use of additional capacitances for shortening lines [103]. Finally, the quadrature hybrid can be miniaturized through its realization as a patch square resonator [70].

It can be seen that for commonly achieved impedance transformation in a classic branch-line coupler, transmission-line impedances have to be properly chosen depending on the considered design methodology. Moreover, in all mentioned solutions, impedance transforming ratio R is not greater than 2.5. A more complex solution which is composed of a impedance transformer and baluns is presented in the literature [84]. Such a circuit features an impedance-transforming ratio of $R = 6.5$; however, the obtained frequency response is narrow.

3.2.2. Impedance-Transforming Rat-Race Coupler

As has been presented in the literature [42], [93], [5], [56] the impedance-transforming ability can be achieved in the rat-race topology. The classic topology is modified by the impedance change of each transmission-line or by adding additional transforming sections. In [124], a narrowband impedance-transforming rat-race coupler has been investigated.
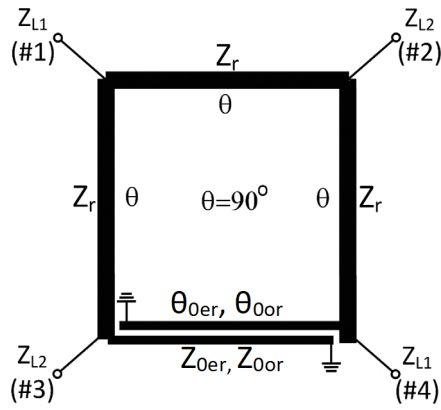
Figure 3.7: Narrowband impedance-transforming rat-race directional coupler [124]. (Copyright © 2018, Taylor & Francis)
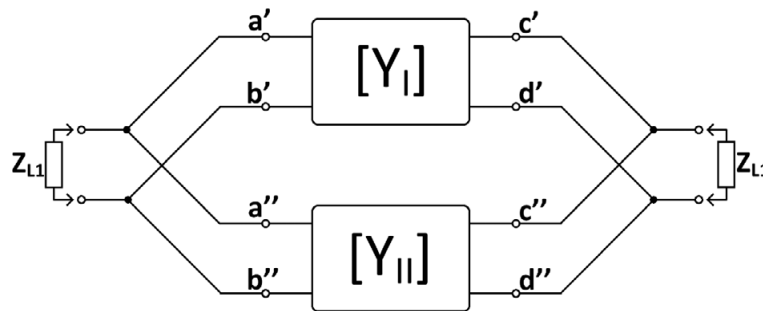
Figure 3.8: The diagram of narrowband impedance-transforming rat-race coupler [124]. (Copyright © 2018, Taylor & Francis)
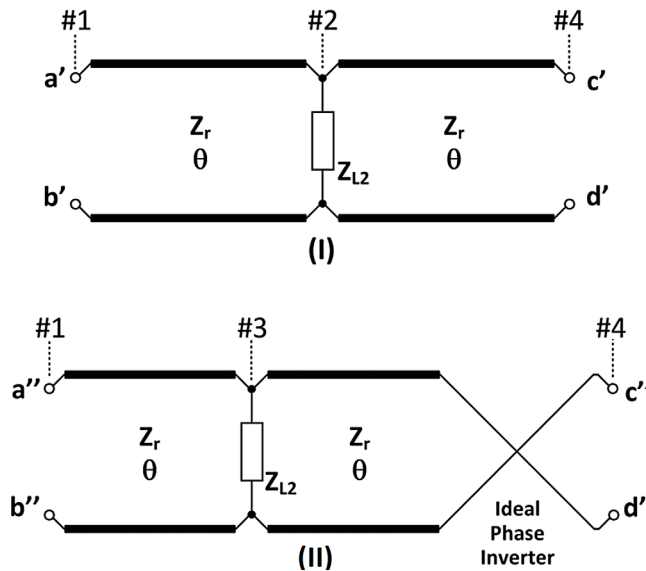
Figure 3.9: Subcircuits I and II defined by admittance matrices $[Y_I]$ and $[Y_{II}]$ [124]. (Copyright © 2018, Taylor & Francis)

The proposed structure with marked termination impedances is presented in Fig. 3.7. As can be observed, ports #1, and #4 are defined by the Z_{L1} impedance, while ports #2, and #3 have termination Z_{L2} impedance. Characteristic impedances of the entire rat-race ring is characterized by impedance Z_r. To reduce the size of the coupler, the $270°$ electrical length transmission-line has been replaced by a quarter-wave coupled-line section [90] with modal impedances defined as:

$$Z_{0er} = (\sqrt{2} + 1)Z_r \tag{3.13}$$

and

$$Z_{0or} = (\sqrt{2} - 1)Z_r. \tag{3.14}$$

The presented topology is not symmetrical, thus the odd-even mode analysis of such a structure is not possible. The rat-race coupler can be considered as a parallel connection of two subcircuits named *I* and *II*, which are defined by admittance matrices Y_I, Y_{II}. Such an approach is presented in Fig. 3.8 and a detailed view of subcircuits *I* and *II* is shown in Fig. 3.9 .

Each of the subcircuits can be defined by ABCD parameters; assuming that electrical length of transmission-lines is $\theta = 90°$, then:

$$[ABCD_I] = \begin{bmatrix} 0 & jZ_r \\ j\frac{1}{Z_r} & 0 \end{bmatrix} \cdot \begin{bmatrix} 1 & 0 \\ \frac{1}{Z_{L2}} & 1 \end{bmatrix} \cdot \begin{bmatrix} 0 & jZ_r \\ j\frac{1}{Z_r} & 0 \end{bmatrix} = \begin{bmatrix} -1 & -\frac{Z_r^2}{Z_{L2}} \\ 0 & -1 \end{bmatrix} \tag{3.15}$$

$$[ABCD_{II}] = \begin{bmatrix} 0 & jZ_r \\ j\frac{1}{Z_r} & 0 \end{bmatrix} \cdot \begin{bmatrix} 1 & 0 \\ \frac{1}{Z_{L2}} & 1 \end{bmatrix} \cdot \begin{bmatrix} 0 & jZ_r \\ j\frac{1}{Z_r} & 0 \end{bmatrix} \cdot \begin{bmatrix} -1 & 0 \\ 0 & -1 \end{bmatrix} = \begin{bmatrix} 1 & \frac{Z_r^2}{Z_{L2}} \\ 0 & 1 \end{bmatrix}. \tag{3.16}$$

Due to the parallel connection of the subcircuits, the calculations of the coupler response have been simplified through the conversion of the obtained ABCD parameters into admittance parameters by utilizing equations derived in [37]. Having both admittance matrices, the overall matrix $[Y]$ has been calculated as

$$[Y] = [Y_I] + [Y_{II}] = \begin{bmatrix} \frac{Z_{L2}}{Z_r^2} & \frac{Z_{L2}}{Z_r^2} \\ \frac{Z_{L2}}{Z_r^2} & \frac{Z_{L2}}{Z_r^2} \end{bmatrix} + \begin{bmatrix} \frac{Z_{L2}}{Z_r^2} & -\frac{Z_{L2}}{Z_r^2} \\ -\frac{Z_{L2}}{Z_r^2} & \frac{Z_{L2}}{Z_r^2} \end{bmatrix} = \begin{bmatrix} 2\frac{Z_{L2}}{Z_r^2} & 0 \\ 0 & 2\frac{Z_{L2}}{Z_r^2} \end{bmatrix} \tag{3.17}$$

Finally, the admittance matrix has been converted into matrix S to derive the impedance-matching condition. For such a case, parameter S_{11} has been found by using the equation [37]:

$$S_{11} = \frac{(1 - Y_{11}Z_{L1})(1 + Y_{22}Z_{L1}) + Y_{12}Y_{21}Z_{L1}^2}{(1 + Y_{11}Z_{L1})(1 + Y_{22}Z_{L1}) - Y_{12}Y_{21}Z_{L1}^2}, \tag{3.18}$$

which can be presented in a simpler form:

$$S_{11} = 1 - \frac{4Z_{L1}^2 Z_{L2}^2}{Z_r^4}. \tag{3.19}$$

Assuming that for ideal match, the condition $S_{11} = 0$ has to be meet, formula 3.19 can be presented as:

$$Z_r = \sqrt{2Z_{L1}Z_{L2}} \tag{3.20}$$

which corresponds to the results obtained in the literature [93], [6], and defines the main condition which has to be obtained for the ideal impedance match in the 3-dB transforming narrowband rat-race coupler. In terms of the impedance-transforming ratio R, the derived formula takes the form:

$$Z_r = Z_{L2}\sqrt{\frac{2}{R}} \tag{3.21}$$

where

$$R = \frac{Z_{L2}}{Z_{L1}}. \tag{3.22}$$

Equation 3.19 can be expressed as a fraction of electrical length θ:

$$S_{11}(\theta) = -\frac{2Z_r^2\sin^2(\theta) - 2jZ_rZ_{L2}\sin(2\theta)}{2Z_{L1}Z_{L2}\cos(2\theta) - Z_r^2\sin^2(\theta) + jZ_r(Z_{L1}+Z_{L2})\sin(2\theta)} - 1. \tag{3.23}$$

Based on the derived equation, the frequency response for different values of the impedance-transforming ratio have been calculated; the obtained results are presented in Fig. 3.10. It has been proven in the literature [93] that by increasing the R coefficient, the operational bandwidth of the rat-race coupler decreases. According to the calculated response, the same situation has been observed in the considered component.
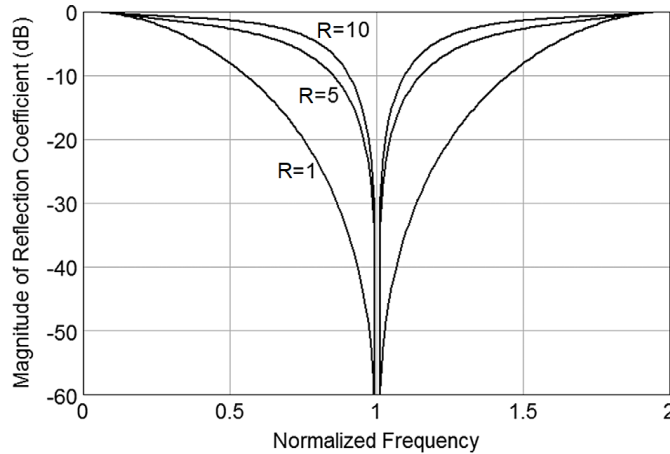
Figure 3.10: Reflection coefficients of a narrowband rat-race directional coupler calculated from (3.23) for impedance-transforming ratio $R = 1$, 5 and 10 [124]. (Copyright © 2018, Taylor & Francis)

The considered 3-dB impedance-transforming rat-race coupler featuring a narrow operational bandwidth has been developed using the microstrip technique to verify the correctness of the proposed design methodology. The coupler has been matched to the terminating impedances $Z_{L1} = 10$ Ω and $Z_{L2} = 50$ Ω which corresponds to $R = 5$ and operates at a 1 GHz center frequency. A cross-sectional view of the used stack-up is presented in Fig. 3.11, while the geometry and electrical parameters of the structure are collected in Table 3.3. The width of the transmission-lines with impedance Z_r is equal to w_1. To obtain appropriate coupling in the coupled-line section having impedances Z_{0er} and Z_{0or}, a modified Lange structure consisting of five strips has been utilized. Such a section is composed of five strips with widths w_2 and a gap between the lines of s_2.
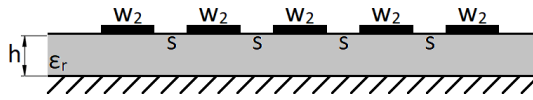
Figure 3.11: A cross-sectional view of dielectric stratification utilized for the proposed impedance-transforming rat-race coupler [124]. (Copyright © 2017, Taylor & Francis.)

Table 3.3: Electrical parameters and calculated geometry of the impedance-transforming rat-race directional coupler.

Geometry	Value	Electrical Parameter	Value
$w_1[mm]$	4.77	$Z_r[\Omega]$	31.62
$w_2[mm]$	0.65	$Z_{0e}[\Omega]$	76.34
$s_2[mm]$	0.12	$Z_{0o}[\Omega]$	13.09
$h[mm]$	1.57		
ε_r	6.15		
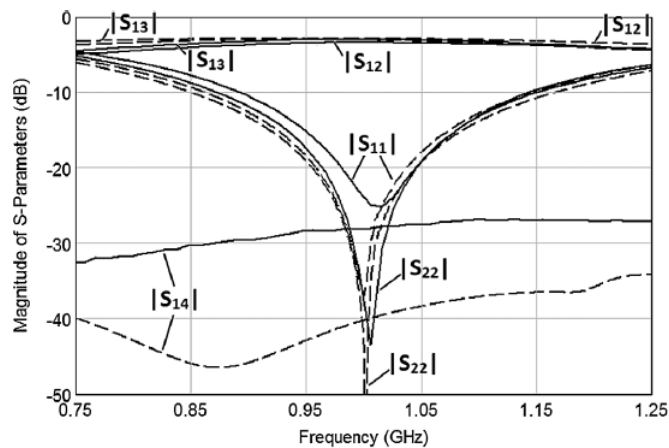
(a)
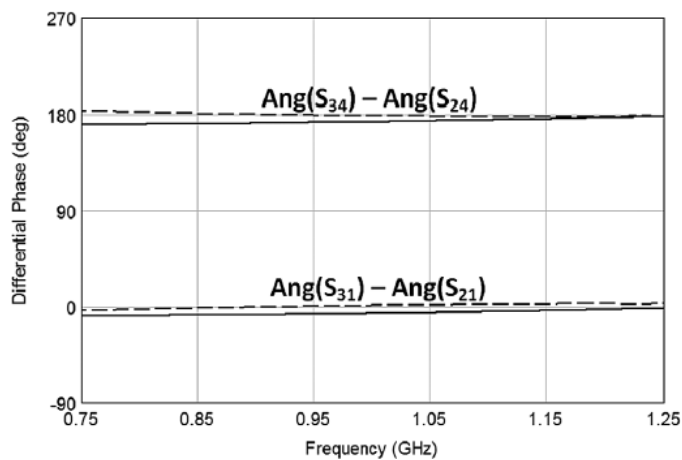
(b)

Figure 3.12: Obtained S-parameters (a) and differential phases (b) of the designed narrowband rat-race coupler. Results of electromagnetic simulations (dashed lines) and measurements (solid lines) [124]. (Copyright © 2017, Taylor & Francis.)

The proposed impedance-transforming narrowband rat-race coupler has been fabricated and subsequently measured. The results have been compared with the simulations and are shown in Fig. 3.12. The obtained isolation of the directional coupler is greater than 28 dB, the reflection coefficient seen from the 50 Ω port is greater than 23 dB, while for the 10 Ω port, it is greater than 37 dB. The measured phase imbalance did not exceed 8.2°. All of the mentioned values were measured at a 1 GHz center frequency. The layout and photograph presenting the manufactured impedance-transforming rat-race coupler are shown in Fig. 3.13.

(a)

(b)
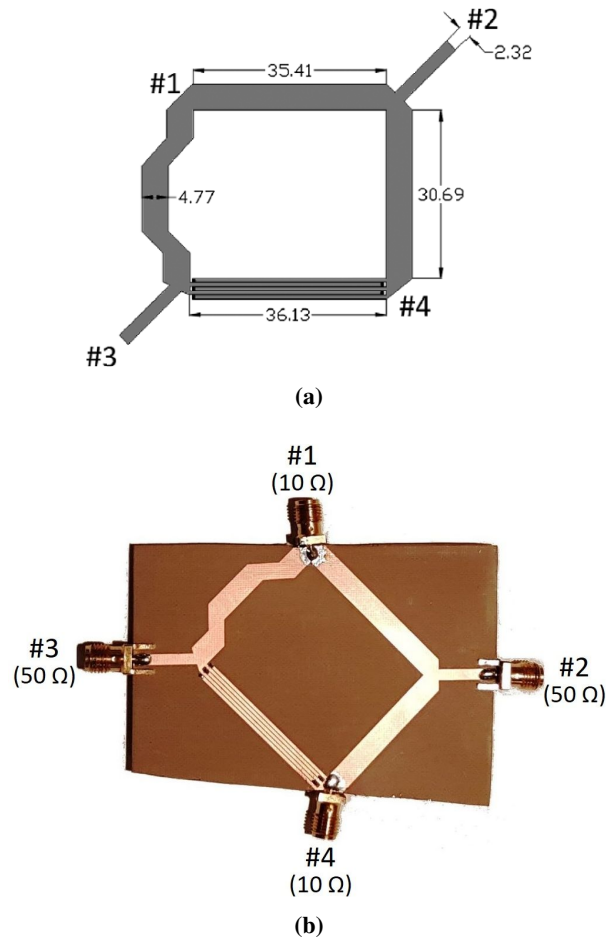
Figure 3.13: Layout (a) and photograph (b) of the fabricated 3-dB narrowband impedance-transforming rat-race directional coupler with a transformation ratio of $R = 5$ [124]. (Copyright © 2017, Taylor & Francis.)

To enhance the operational bandwidth of the impedance-transforming rat-race coupler, the additional transformers connected to the ports of the rat-race ring have been utilized [124]. It should be mentioned, that such an approach is similar to the ideas presented in the literature [47] and [21]. In comparison to the mentioned solutions, the proposed coupler has additional coupled-line sections connected only to one pair of ports, and the transformation ratio of such coupled-line sections is equal to unity (1:1) which reduces the overall size of the coupler and simplifies the design process. The concept view of the proposed enhanced-bandwidth impedance-transforming rat-race coupler is shown in Fig. 3.14. Additional components in the form of quarter-wave coupled-lines sections are characterized by modal

impedances Z_{0oT}, Z_{0eT} and coupling coefficient C_T connected between the rat-race ring and external ports #2, and #3.
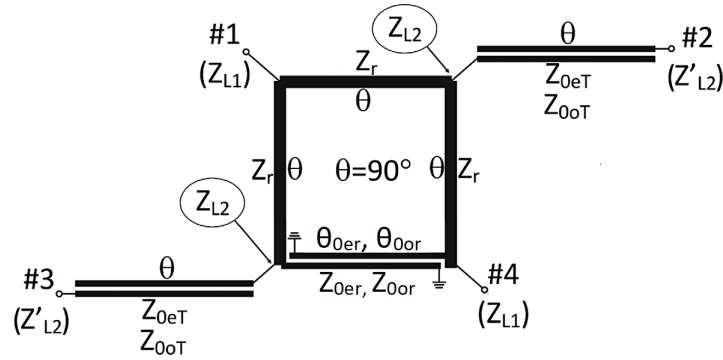
Figure 3.14: Enhanced-badwidth impedance-transforming rat-race coupler [124]. (Copyright © 2018, Taylor & Francis)

As previously mentioned, the connected transformers do not transform the ring impedance, thus $Z_{L2} = Z'_{L2}$. The external, terminating impedance Z'_{L2} in terms of electrical length changes can be calculated as follows [66]:

$$Z'_{L2}(\theta) = -0.5j \cot(\theta) \left(Z_{0eT} + Z_{0oT}\right) - \frac{[0.5j \left(Z_{0eT} - Z_{0oT}\right)]^2}{\sin^2(\theta) \left(0.5j \cot \left(Z_{0eT} + Z_{0oT}\right)\right)}. \tag{3.24}$$

Assuming that for the quarter-wave section $\theta = 90°$, modal impedances Z_{0eT} and Z_{0oT} can be derived as follows:

$$Z_{0eT} = \sqrt{\frac{Z_{L2}Z'_{L2}}{0.25}} + Z_{0oT}, \tag{3.25}$$

$$Z_{0oT} = Z_{0eT} - \sqrt{\frac{Z_{L2}Z'_{L2}}{0.25}}. \tag{3.26}$$

It can be observed, that by substituting equation 3.24 into 3.23, the reflection coefficient of the improved impedance-transforming rat-race coupler can be calculated.

A 3-dB impedance-transforming rat-race coupler featuring a broad operational bandwidth has been designed. The electrical parameters of the main ring structure are the same as those calculated for the narrowband coupler presented in Fig. 3.7. To enhance operational bandwidth, additional coupled-line sections with modal impedances Z_{0eT}, Z_{0oT} were connected to the opposite ports of the ring structure. To determine values of impedances, calculations based on equations 3.24 - 3.26 were conducted. Figure 3.15a shows relations between return losses and even impedance Z_{0eT} of the coupled-line sections, with the assumption that the considered coupler has a transformation ratio of $R = 5$, additional sections coupling of $C_T = 9$ dB and that loads are $Z_{L1} = 10 \ \Omega$ and $Z'_{L2} = 50 \ \Omega$. During iterative computations, optimal electrical parameters of the coupled-line sections were found and are $Z_{0eT} = 191.5 \ \Omega$ and $C_T = 9$ dB. It can easily be calculated that for such a pair of parameters, odd impedance $Z_{0oT} = 91.5 \ \Omega$. Additionally, the relationship between reflection losses and rat-race impedance Z_r which has a direct influence on transformation ratio R has been calculated and presented in Fig. 3.15b. It can be clearly seen, that when Z_r decreases, the return losses of the coupler deteriorate.
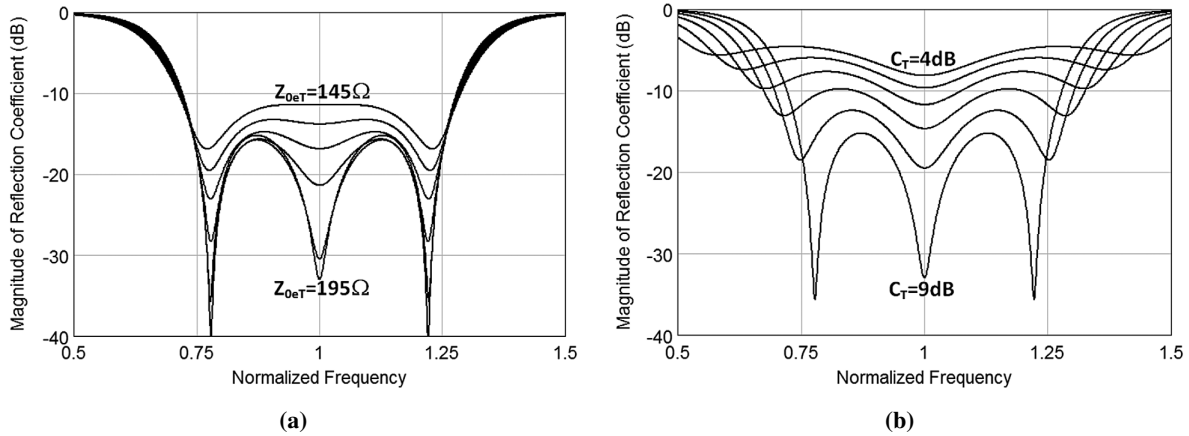
Figure 3.15: Reflection coefficient of enhanced-bandwidth rat-race coupler for several values of Z_{0eT} impedance assuming constant coupling coefficient of C= 9 dB (a) and several values of coupling C_T of the coupled-line sections assuming $Z_{0eT} =$ 191.5 Ω (b) [124]. (Copyright © 2017, Taylor & Francis.)
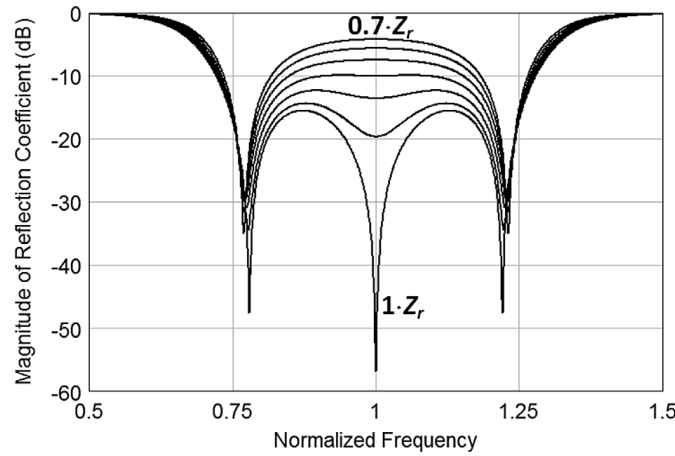
Figure 3.16: Reflection coefficient of enhanced-bandwidth rat-race coupler for several values of ring impedance Z_r assuming $Z_{0eT} = 191.5$ Ω and $Z_{0oT} = 91.5$ Ω [124]. (Copyright © 2017, Taylor & Francis.)
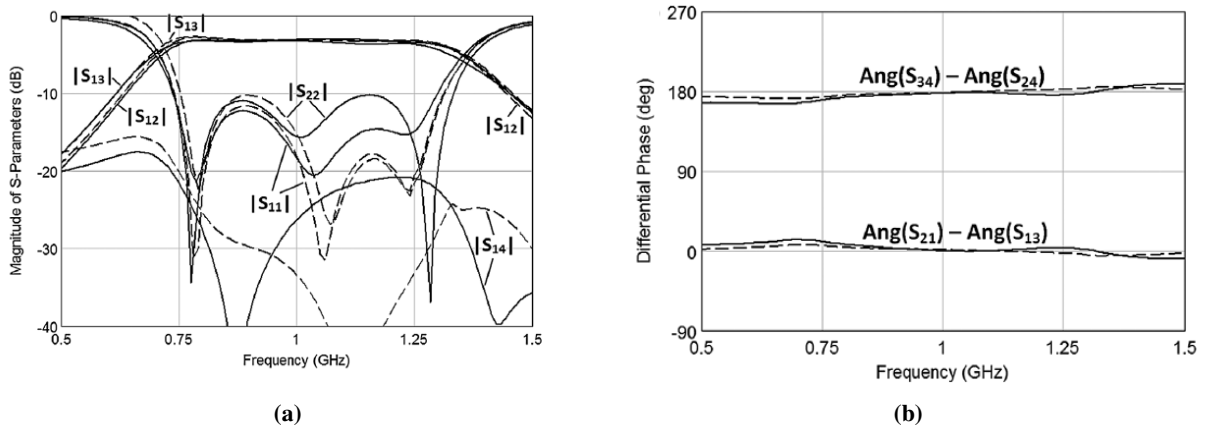
Figure 3.17: Obtained S-parameters (a) and differential phases (b) of the proposed enhanced-bandwidth rat-race coupler. Results of electromagnetic simulations (dashed lines) and measurements (solid lines) [124]. (Copyright © 2017, Taylor & Francis.)
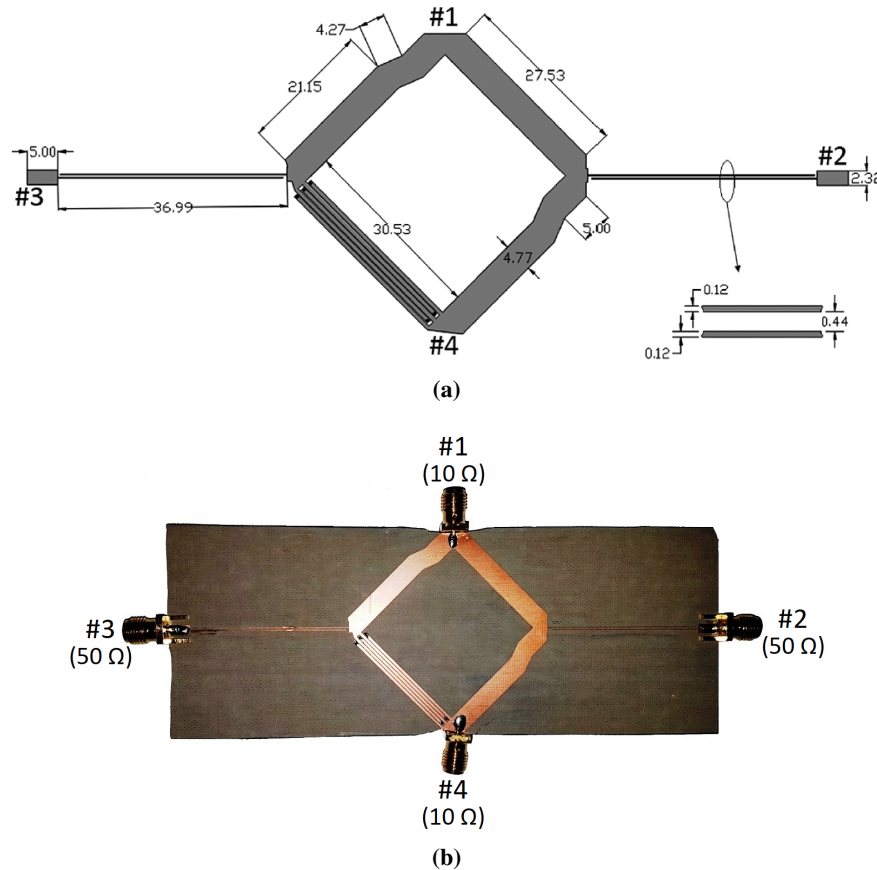
Figure 3.18: Layout (a) and photograph (b) of fabricated 3-dB enhanced-bandwidth impedance-transforming rat-race directional coupler with transformation ratio of $R = 5$ [124]. (Copyright © 2017, Taylor & Francis.)

The considered impedance-transforming enhanced-bandwidth rat-race coupler was designed, and simulated electromagnetically by using the AXIEM solver from Cadence AWR Microwave Office. The simulations together with results obtained from measurements of fabricated coupler are presented in Fig. 3.17. Measured return losses are not lower than 10dB and the isolation is greater than 21 dB in the operational bandwidth. Moreover, measured insertion losses are not greater than 0.38 dB, and the differential phase imbalance does not exceeded 7°. The layout and the fabricated directional coupler are presented in Fig. 3.18.
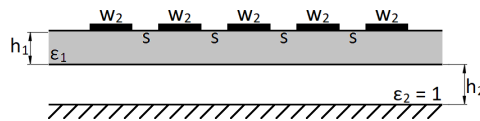
Figure 3.19: Cross-sectional view of a substrate stack-up utilized in the low-loss version of the impedance-transforming rat-race coupler with a transformation ratio of $R = 2$ [123]. (Copyright © 2018, IEEE)

The previous idea of an enhanced-bandwidth impedance-transforming rat-race coupler has been designed and fabricated utilizing the microstrip technique. To reduce total losses of such a structure, the same topology has been utilized in the suspended microstrip technique. A general view of the coupler is presented in Fig. 3.14 and a cross-sectional view of the utilized substrate stack-up is presented in Fig. 3.19. In such a stratification, the substrate with thickness h_1 and electric permitivity ϵ_{r1} is placed

above the ground plane at distance h_2. It has to be mentioned than air was used as the material filling the space between the layers $\epsilon_{r2} = 1$. The coupler was designed as a circuit which is matched to $Z_{L1} = 25\ \Omega$ and $Z_{L2} = 50\ \Omega$, which corresponds to the impedance-transforming ratio of $R = 2$. Computed geometry and electrical parameters of the component are collected in Table 3.4.

Table 3.4: Calculated values of geometry and electrical parameters of the low-loss impedance-transforming rat-race coupler with enhanced operational bandwidth and transformation ratio of $R = 2$ [123]. (Copyright © 2018, IEEE)

Geommetry	Value	Electrical Parameter	Value
$w_1[mm]$	1.74	$Z_r[\Omega]$	50
$w_2[mm]$	1.16	$Z_{0e}[\Omega]$	120.7
$s_1[mm]$	0.48	$Z_{0o}[\Omega]$	20.71
$s_2[mm]$	0.4	$Z_{0eT}[\Omega]$	131
$h_1[mm]$	0.508	$Z_{0eT}[\Omega]$	30.4
$h_2[mm]$	2	$Z_{L1}[\Omega]$	50
ε_r	3.38	$Z_{L2}[\Omega]$	25

To achieve strong coupling in the coupled-line section, a Lange structure consisting of five strips was utilized. Such a conception was proposed in the previous version of this coupler. Moreover, the coupled-line section with modal impedances Z_{0eT} and Z_{0oT} has been realized as three-strip sections. Simulations of the coupler are presented in Fig. 3.20 together with results obtained during measurements of the fabricated component. Moreover, Figure 3.21 shows calculated total losses of the manufactured coupler. The measured isolation is not lower than 19.5 dB and the reflection coefficient is lower than -9.5 dB. The insertion losses are not greater than 0.1 dB. Moreover, based on measurements, the total losses have been calculated and are presented in Fig. 3.21. As can be seen, measured losses are not greater than 0.24 dB in the operational bandwidth of the directional coupler. In Figure 3.22, the fabricated impedance-transforming rat-race coupler is presented. The overall size of the coupler is 11.5 x 24 cm.
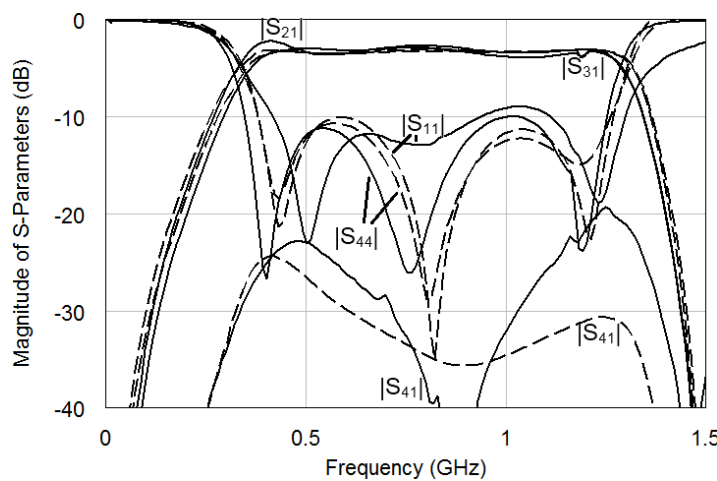
Figure 3.20: Scattering parameters obtained during simulations (dashed lines) and measurements (solid lines) of the low-loss impedance-transforming rat-race coupler [123]. (Copyright © 2018, IEEE)
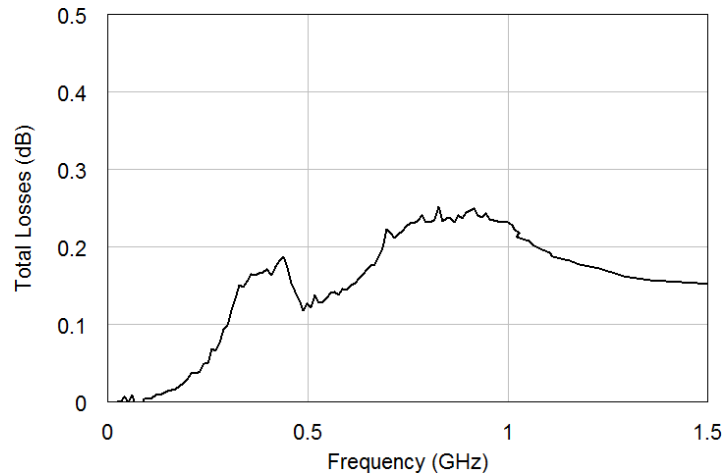
Figure 3.21: Measured total losses of the manufactured impedance-transforming rat-race coupler [123]. (Copyright © 2018, IEEE)
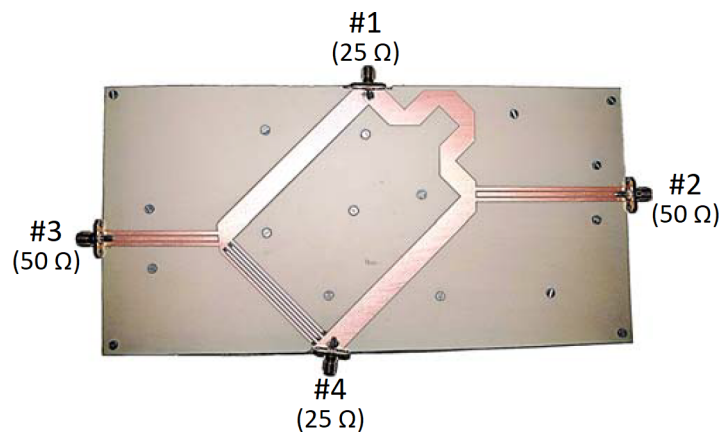
Figure 3.22: Photograph of fabricated low-loss impedance-transforming rat-race coupler [123]. (Copyright © 2018, IEEE)

3.3. Conclusions

In this chapter, novel impedance-transforming directional couplers based on coupled-line sections and directly-connected transmission-lines have been shown. Firstly, a short introduction to a simple asymmetric coupled-line section featuring impedance transformation was presented. It has been shown, that the maximum available transformation ratio R cannot exceed a value of 2, unless other topology such as a multisection structure is used. An alternative solution which has been proposed is based on tandem-connected topology. It has been proven, that the structure offers a substantially larger impedance transformation ratio than the asymmetric coupled-line section, due to the fact that the required coupling coefficient in tandem structures is lower. Moreover, tandem topology can be utilized to achieve return losses of the impedance-transforming directional couplers similar to those obtained for two-section impedance transformers. Therefore, the proposed couplers feature a wider bandwidth not limited by narrowband return loss characteristics in comparison to the existing solutions. To verify the applicability of the design method, an impedance-transforming coupler with $R = 5$ was designed and fabricated. Another solution presented in this chapter is based on rat-race topology which has been utilized for the first time as an impedance-transforming coupler. According to the conducted analysis, a classic rat-race

structure can theoretically infinite impedance transformation, which has been supported by the derived equations. Furthermore, a narrowband version based on classic topology has been improved in terms of operational bandwidth enhancement. The proposed narrowband and broadband impedance-transforming rat-race couplers with a transformation ratio of $R = 10$, were fabricated in a microstrip technique. Moreover, the broadband coupler with decreased total losses has been utilized using the suspended microstrip technique. In this case, the coupler has been designed to match 50Ω and 25Ω termination impedances, which corresponds to an impedance transforming ratio of $R = 2$.

4. Applications of Directional Couplers in Monolithic Microwave Integrated Circuits

In this chapter, three complex monolithic applications based on gallium arsenide consisting of directional couplers are presented. In Section 4.1, a single-ended compact branch-line coupler is presented. The application of two exemplary designs have been utilized in a 24 GHz monolithic integrated sensor which is briefly shown in the thesis. Section 4.2 describes a novel differentially-fed branch-line coupler in which a reduction of the overall size has been assumed by utilizing lumped elements together with transmission-line sections. Moreover, to verify applicability in balanced circuits, a differentially excited amplifier based on a gallium arsenide process has been designed and simulated. In the last Section (4.3), a monolithic FMCW radar front-end operating at a frequency of 24 GHz is shown. The compensated 3-dB three-coupled-line coupler presented in Subsection 2.2.2 has been utilized in the radar circuit.

In this chapter, the author cites his investigation of the differentially-fed branch-line coupler designed using the monolithic technology [46], which has been also utilized in a balanced amplifier. The second paper which has been cited is [121], in which an integrated sensor system operating at a frequency of 24 GHz is introduced.

4.1. Miniaturized Branch-Line Couplers in a Microwave Sensor with Built-in Calibration Capability

In this section the design of two miniaturized monolithic branch-line couplers is shown. The couplers are composed of lumped LC sections to decrease the overall size of the components. The designed couplers have been utilized in the 24 GHz integrated sensor which is dedicated for dielectric permittivity measurements and has been introduced in the literature [121]. The sensor is also briefly presented with an emphasis on presenting the design of particular functional blocks of the designed chip.

4.1.1. Miniaturized Lumped Branch-Line Couplers

The idea of branch-line topology has already been introduced in Section 1.2. Commonly utilized microwave solutions are composed of transmission-lines that have appropriate impedances related to the requested coupling factor. However, due to the relatively large occupied area, such circuits may not be applicable in monolithic processes. Therefore, two commonly used approaches can be considered.

The first approach assumes utilization of the meandered lines, which maintains their physical lengths [138], [142]. The other solution assumes that the transmission-lines can be replaced with lumped-element sections consisting of inductors and capacitors [63], [104]. In such a case, the reduction of the overall dimensions is significant, while the dimensions of the designed LC sections are smaller than the original transmission-lines.
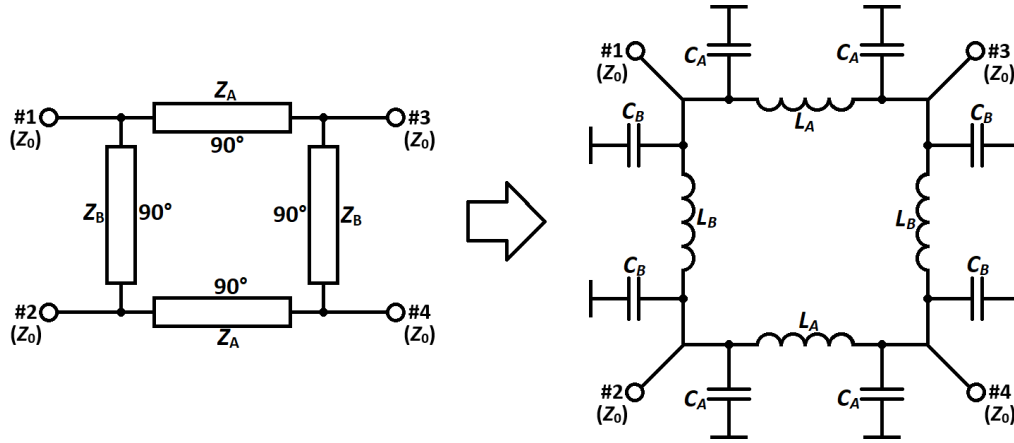
Figure 4.1: Transition between branch-line coupler consisting of quarter-wave lossy transmission-lines and lumped version of the coupler. The transmission-lines have been replaced by LC circuits in π topology.

The concept view of the compact branch-line coupler composed of lumped elements is shown in Fig. 4.1. On the left side of the picture, a classic branch-line coupler consisting quarter-wave transmission lines with impedances Z_A and Z_B is shown. It is worth mentioning, that the values of the impedances are directly related to the required coupling coefficient k of the considered coupler by the following formulas [127]:

$$Z_A = Z_0 \sqrt{1 - k^2}, \tag{4.1}$$

$$Z_B = Z_0 \sqrt{\frac{1}{k^2} - 1}. \tag{4.2}$$

Such transmission-lines can be replaced by appropriate lumped circuits which, in the considered case, are based on the Π topology. The values of inductors and capacitors can be calculated for the particular frequency f_0 as follows:

$$L_{(A,B)} = \frac{Z_{(A,B)}}{2\pi f_0} \tag{4.3}$$

and

$$C_{(A,B)} = \frac{1}{2\pi f_0 Z_{(A,B)}}. \tag{4.4}$$

Using the presented set of equations, two exemplary couplers with 3-dB and 4.77 dB couplings have been designed. Both components operate at the 24 GHz center frequency and the calculated electrical parameters are presented in Table 4.1. Furthermore, the computed frequency responses of the branch-line couplers are presented in Fig. 4.2.

Electrical Parameters	Coupling Factor	
	$C = 3$ dB	$C = 4.77$ dB
Z_A [Ω]	35.35	40.82
Z_B [Ω]	50.00	70.07
L_A [nH]	0.234	0.271
C_A [pF]	0.188	0.162
L_B [nH]	0.331	0.469
C_B [pF]	0.133	0.094
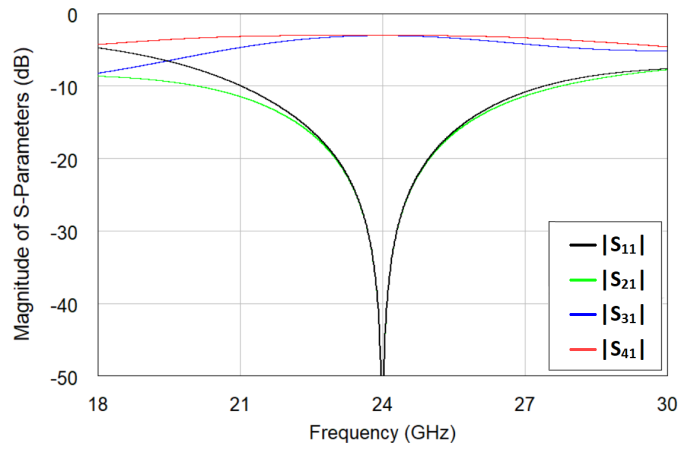
(a)
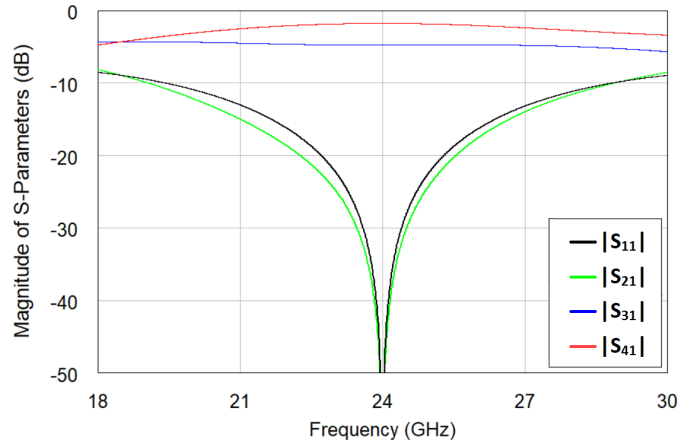
(b)

Figure 4.2: Calculated frequency response of the compact branch-line couplers composed of LC elements having 3-dB and 4.77-dB coupling factors.

The considered 3-dB and 4.77-dB branch-line couplers were designed using monolithic technology based on the gallium arsenide UMS PH25 process. Layouts are presented in Fig. 4.3 together with the obtained simulation results. As can be observed, the results are in good agreement with the calculations. The return losses of the 3-dB coupler at the center frequency are not greater than 20.7 dB and for the

4.77-dB version they are not greater than 27.2 dB. Furthermore, the isolation is better than 36.8 dB for the 3-dB branch-line, while the second features 30.4 dB of isolation. It is worth noting, that the designs have additional losses which result from the utilized materials and structures of lumped elements. The calculated insertion losses of both couplers do not exceed 1.05 dB.
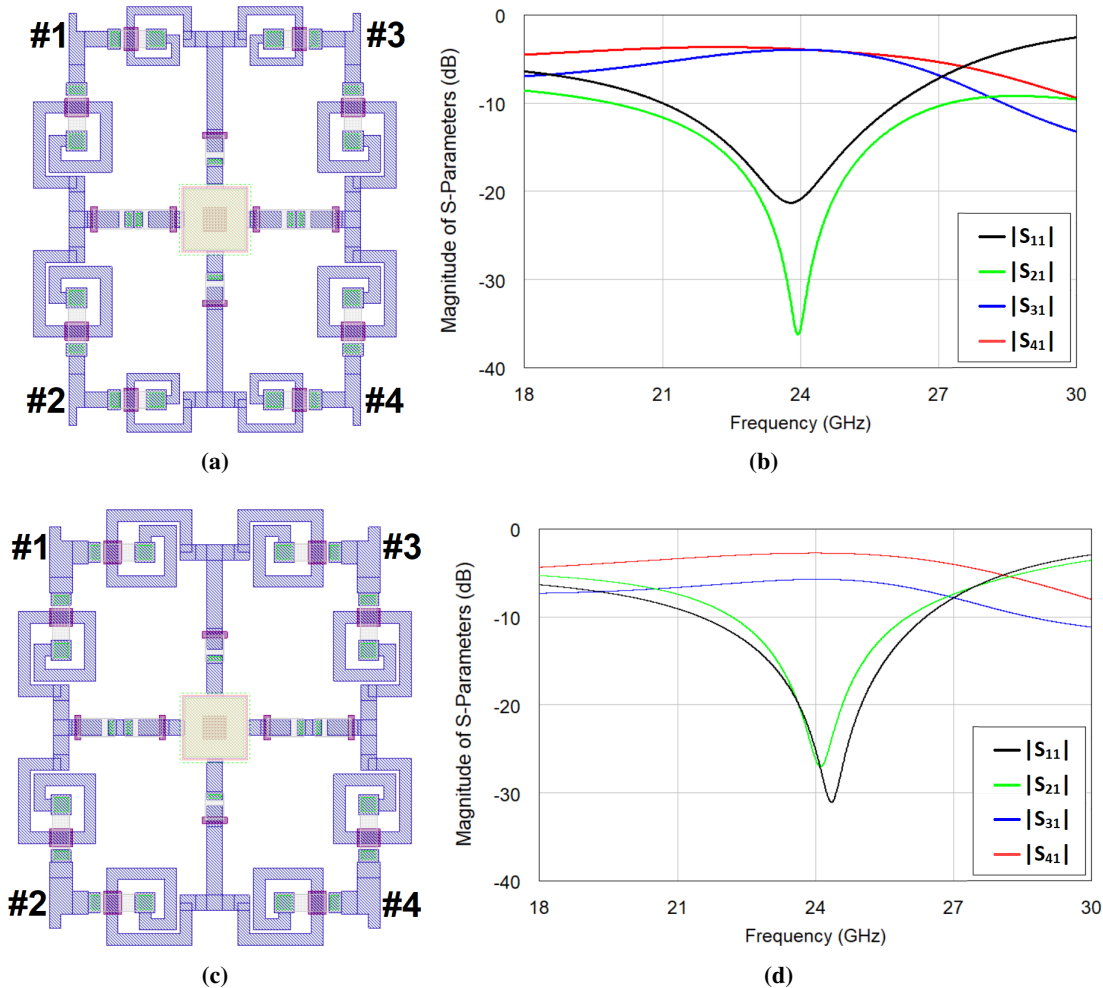
Figure 4.3: The layouts of the designed monolithic compact branch-line couplers with coupling of 3-dB (a) and 4.77-dB (c). Graphs (b) and (d) show simulation results obtained for the 3-dB and 4.77-dB couplers, respectively.

4.1.2. A Microwave Sensor Design with Built-in Calibration Capability

In the [121] a novel monolithic integrated sensor for permittivity measurements is introduced. The measurements of a material's dielectric permittivity can provide sufficient information about its properties. This idea has been utilized in many industrial and laboratory applications, where such measurements are used to analyze different substance contents such as the water content in food [144], [111], the glucose content in blood [101] or the fat content in milk [134], [54]. Moreover, by utilizing appropriate thin-film laminates which change permittivity under the influence of gas molecules, it is possible to measure, for example, the concentration of acetone in breath [132].

It has been mentioned that the sensor is a fully integrated circuit which means that the sensing element and measurement circuitry are placed on the same chip. Such an approach is a good alternative for measurements utilized by VNA in terms of cost reduction and the overall size of the necessary equipment.

To make measurements reliable, a classic calibration assuming external well-defined and known calibration standards cannot be utilized [73], [61]. Thus, the method in which calibration standards have unknown magnitudes and phases presented in the literature [133] has been implemented into the design. Moreover, to achieve the possibility of internal calibration, the proposed sensor has an integrated calibration tuner.
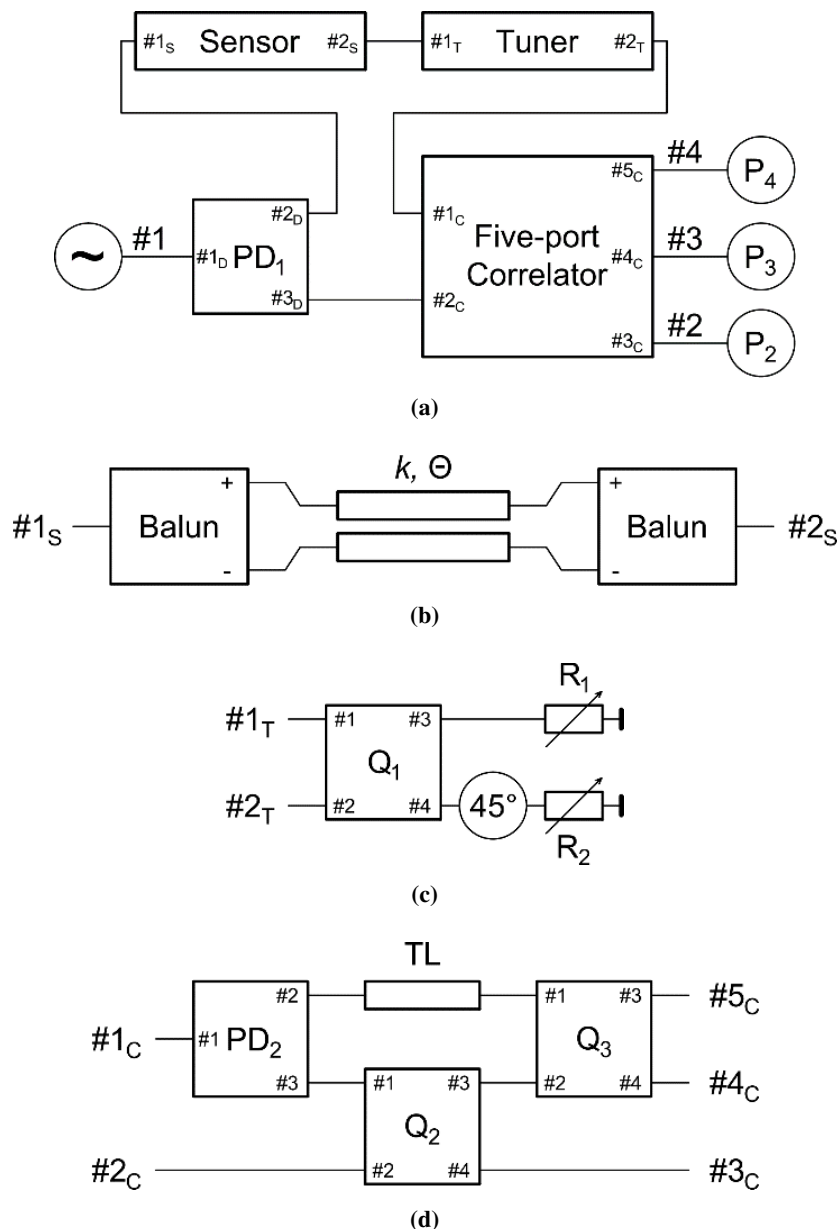
Figure 4.4: Block diagram of the considered sensor (a) and detailed diagrams of particular components: coupled-line section acting as sensing elements (b), calibration tuner (c) and five-port correlator (d) [121]. (Copyright © 2021, IEEE)

The integrated sensor is presented in Fig. 4.4. As can be seen, the sensor is four-port circuit in which the external source is connected to port #1 and ports #2 - #4 are acting as measurement ports to which

power detectors have to be connected.

Furthermore, four functional blocks can be listed: sensing element which consist of coupled-line section and two baluns 4.4a; calibration tuner consisting of 3-dB quadrature coupler and a 45° phase shifter 4.4b; a five-port correlator composed of 3-dB power divider; 3-dB and 4.77 dB quadrature couplers and transmission-line 4.4d and 3-dB power divider PD_1.
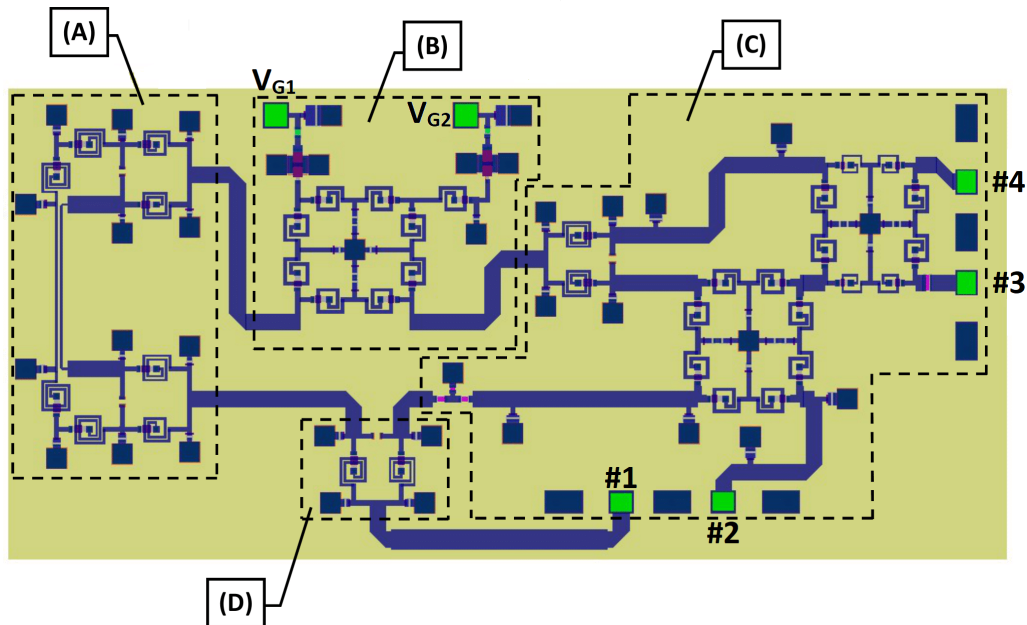
Figure 4.5: Layout of the designed monolithic integrated sensor. The following functional blocks can be seen in the picture: sensing element **(A)**, calibration tuner **(B)**, five-port correlator **(C)** and power divider **(D)** [121]. (Copyright © 2021, IEEE)

Based on the presented view, the monolithic sensor has been designed using the PH25 gallium arsenide process. The considered circuit operates at a frequency of 24 GHz. The layout of the designed integrated sensor system is shown in Fig. 4.5. The following functional blocks can be distinguished in the picture: sensing part **(A)**, calibration tuner **(B)**, five-port correlator **(C)** and power divider PD_1 **(D)**. It is worth noting, that miniaturization is one of the most crucial aspects in monolithic circuits. Therefore, to decrease the overall size of the chip, all components have been designed utilizing lumped elements. Quadrature couplers which have been used in the calibration tuner and five-port correlator are based on designs presented in Subsection 4.1.1.

A sensing part of the sensor is presented in Fig. 4.6. It is composed of a coupled-line section and balanced-unbalanced (balun) circuits which are marked **(A)** and **(B)**, respectively. The transmission-lines utilized in the coupled section have a lengths of 570 μm, widths of 8 μm and the distance between the lines is also equal to 8 μm. Furthermore, the top metallization layer in which the coupled-line section has been designed is 3 μm thick. It is worth noting that the geometry of the structure enables measurements of biological and chemical samples on a microscale. To maximize the sensor's sensitivity to the tested materials' permittivity, an odd excitation of the coupled section needs to be applied, which has been obtained with two identical baluns **(B)**. A single structure is composed of a 3-dB Wilkinson divider and a phase shifter which provides 180° of differential phase between the baluns output's. Figure 4.7 presents results obtained during simulations of the sensing part of the monolithic sensor.
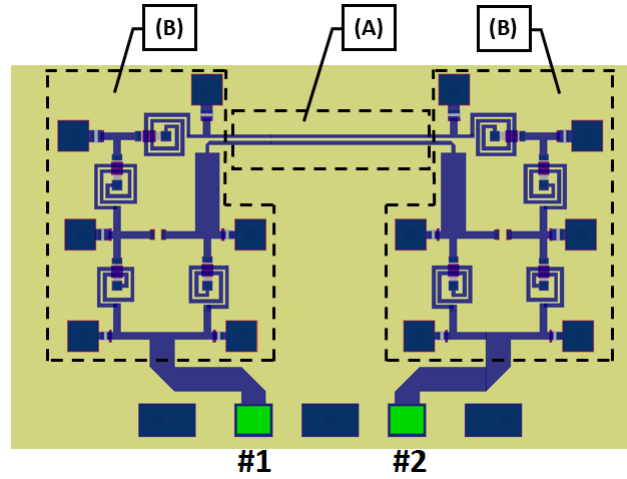
Figure 4.6: The sensing part composed of differentially-fed coupled-line section **(A)** and balanced-unbalanced circuits **(B)** [121]. (Copyright © 2021, IEEE)
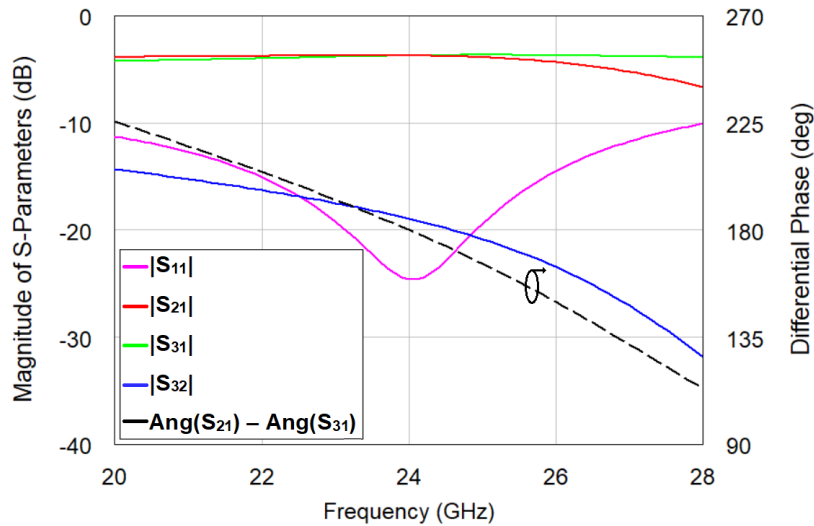
Figure 4.7: Simulated scattering parameters (solid lines) and differential phase (dashed line) of the sensing part [121]. (Copyright © 2021, IEEE)

It has been mentioned that the sensor has an integrated calibration tuner. The layout of such a circuit is shown in Fig. 4.8. The circuit is composed of an equal-split branch-line coupler (presented in Subsection 4.1.1) **(A)** and $45°$ phase shifter **(C)**. To realize the variable resistances R_1 and R_2, two 75 μm two-finger gate pHEMT transistors **(B)** were used. Their drain-source resistance realizing the mentioned resistances can be controlled by external biasing voltages V_{G1} and V_{G2}. As can be seen in Fig. 4.9 the biasing voltage from -0.8 V to 0 V provides a wide range of resistance, which in turn ensures a broad range of the calibration tuner's transmission coefficient S_{21}^T values needed for robust calibration of the sensor. The maximum spread of the S_{21}^T has been examined with the use of a simulation performed for different voltages V_{G1} and V_{G2} both ranging from -0.8 V to 0 V with steps of 10 mV. A similar procedure has been performed for the fabricated calibration tuner, with the step increased to 100 mV. The obtained results are presented in Fig. 4.10.
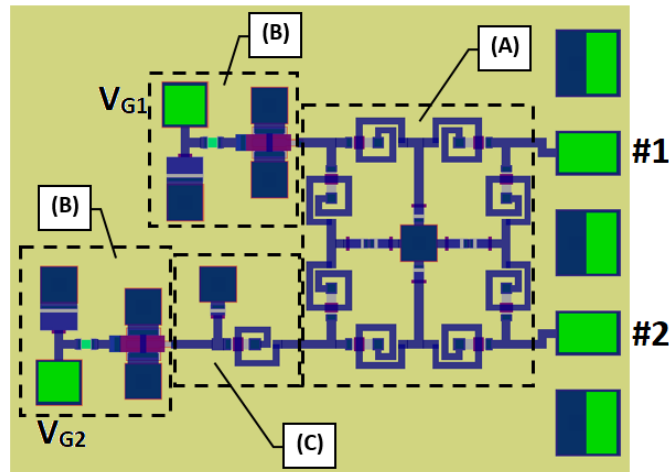
Figure 4.8: Layout of the calibration tuner with marked 3-dB lumped branch-line coupler **(A)**, pHEMT transistors acting as variable resistances R_1, R_2 **(B)** and 45° phase shifter [121]. (Copyright © 2021, IEEE)
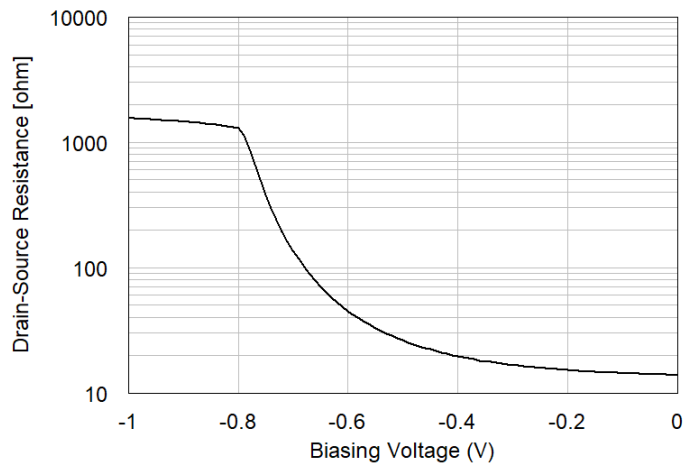
Figure 4.9: Simulated drain-source resistance of the utilized 75 μm two-finger gate pHEMT transistor vs. biasing voltage [121]. (Copyright © 2021, IEEE)

(a)   (b)
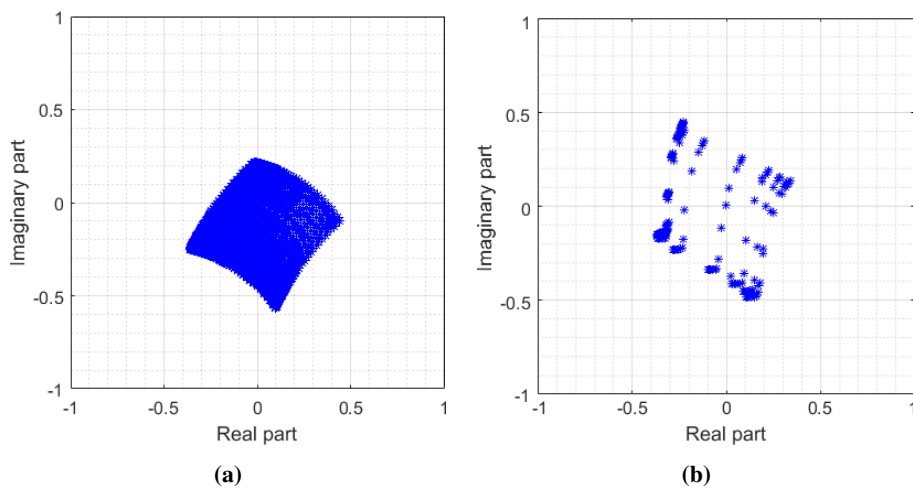
Figure 4.10: Distribution of the developed calibration tuner's transmission coefficient S_{21}^{T}. Results of electromagnetic simulation (a) and measurements of the manufactured tuner (b) [121]. (Copyright © 2021, IEEE)

The last of the considered components of the monolithic sensor is the five-port correlator which is presented in Fig. 4.11. Such a circuit consists of 3-dB and 4.77-dB branch-line couplers marked as **(A)** and **(B)**, respectively, a 3-dB Wilkinson power divider **(C)** and a quarter-wave transmission-line which is shortened by utilizing additional lumped capacitors at the ends **(C)**. The couplers which have been used in the design of the correlator are considered in the previous Subsection (4.1.1). The designed component should exhibit an equal division of the signal from each input port p_{in} (#1 and #2) to all output ports p_{out} #3, #4 and #5. Furthermore, the correlator should provide proper differential phases equal to: 120°, -120° and 0° which are obtained for phases between p_{in} and p_{out} #5, #3 and #4, respectively. To verify such properties, the simulated s-parameters together with the measurement results of the fabricated correlator have been compared and are presented in Fig. 4.12 and Fig. 4.13. As can be observed, the obtained measurements clearly correspond to the theoretical assumptions presented in the literature [121], allowing for measurements with the developed sensor at the 24 GHz center frequency.
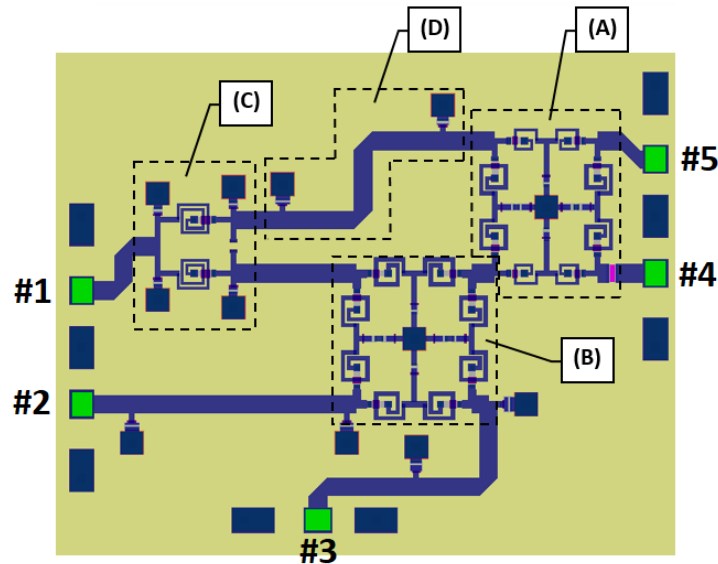
Figure 4.11: Layout of the five-port correlator designed in the PH25 process. The following elements can be seen: branch-line couplers **(A)**, **(B)**, Wilkinson power divider **(C)** and quarter-wave transmission-line **(D)** [121]. (Copyright © 2021, IEEE)
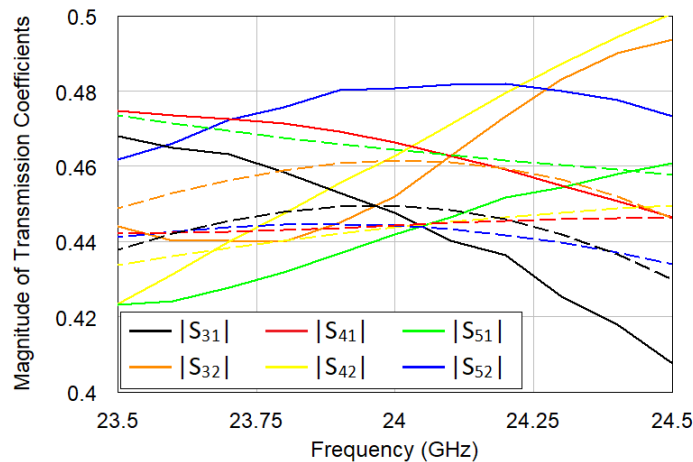
Figure 4.12: Magnitude of simulated (dashed lines) and measured (solid lines) transmission coefficients of the designed five-port correlator [121]. (Copyright © 2021, IEEE)
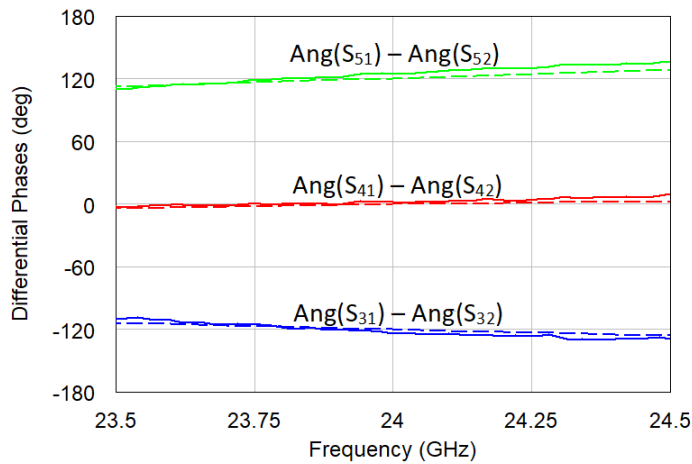
Figure 4.13: Simulated (dashed lines) and measured (solid lines) differential phases of the designed five-port correlator [121]. (Copyright © 2021, IEEE)

A photograph of the manufactured integrated sensor is presented in Fig. 4.14. The die can be divided into two parts - the top part is the complete sensor, and the bottom part is composed of its particular components (the coupled-line section, the calibration tuner and the five-port correlator) fabricated as separate circuits for experimental verification. The manufactured chip has the dimensions 3.4 mm x 4.0 mm. It is also worth noting that the PH25 process does not provide a passivation layer on the top metallization layer. Therefore, elements such as the coupled-line section are exposed. This increases the sensitivity of the sensor, as the material under test can be placed directly on the coupled section, where the electromagnetic field is the strongest. It also allows, for example, selective deposition of a thin film that changes its permittivity under a target gas exposure onto the coupled-line section.
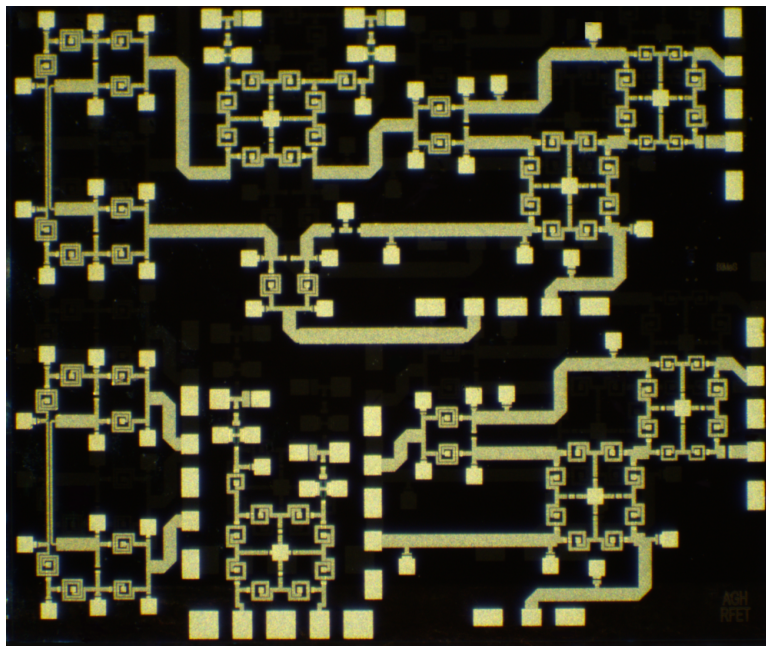
Figure 4.14: Photograph of the fabricated die composed of the monolithic integrated sensor system (top part of the chip) and its separate components: coupled-line section - sensing element, calibration tuner and five-port correlator (bottom part of the die) [121]. (Copyright © 2021, IEEE)

4.2. Application of Miniaturized Differentially-Fed Branch-Line Coupler in Balanced Low-Noise Amplifier

In this section, a novel differentially-fed branch-line coupler reported in [46] is shown. The exemplary coupler has been designed to operate at the 24 GHz center frequency in the gallium arsenide process. Moreover, to verify its applicability in balanced circuits, the proposed branch-line coupler has been utilized in a monolithic differentially excited amplifier.

4.2.1. Miniaturized Differentially-Fed Branch-Line Coupler

The differentially-fed branch-line couplers are commonly reported in literature as structures designed using the PCB technology [119], [118], [153], [30]. However, in monolithic processes, most of the known solutions are designed as single-ended structures [140], [55], [19], [143], [12], [57]. As mentioned in Subsection 4.1.1, the main issue which is observed in monolithic circuits is related to the miniaturization ability of the considered circuit. In [46], a miniaturized monolithic differentially-fed branch-line coupler designed using the gallium arsenide process is proposed. The coupler is presented in Fig. 4.15.
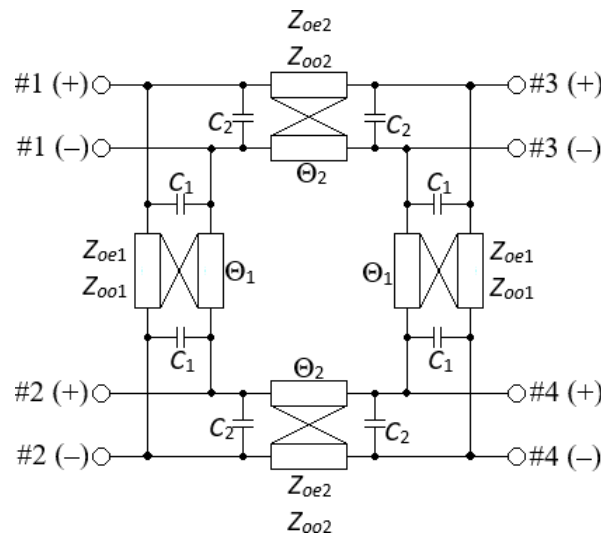
Figure 4.15: Schematic of a miniaturized differentially-fed branch-line coupler [46]. (Copyright © 2020, MDPI)

The considered circuit is composed of differentially excited transmission-lines forming sections with modal impedances $Z_{0e(1,2)}$, $Z_{0o(1,2)}$, electrical lengths $\Theta_{1,2}$ and additional capacitances $C_{1,2}$ connected at the ends of the lines. To decrease the overall dimensions of the coupler, the sections have been shortened by utilizing the method presented for a single-ended topology [41], in which additional capacitances between the lines have been added. According to this technique, the electrical length of each transmission-line can be calculated from:

$$\Theta_{1,2} = \arcsin\left(\frac{Z_1}{Z_2}\right), \tag{4.5}$$

where Z_1 corresponds to the impedance of the original section, and Z_2 corresponds to the impedance of the shorted section. The capacitances connected on both ends of the lines can be derived using:

$$C_{1,2} = \frac{1}{\omega\sqrt{\frac{1}{Z_1^2} - \frac{1}{Z_2^2}}}. \tag{4.6}$$

In the considered case, where coupled-line sections are utilized, the capacitors C_1 and C_2 have an influence only on odd-mode impedance characteristics of the coupled sections. Thus, such an impedance has to be considered during calculations of Θ and C. The values of even-mode characteristic impedances do not have an impact on the response of the designed differentially-fed hybrid coupler.
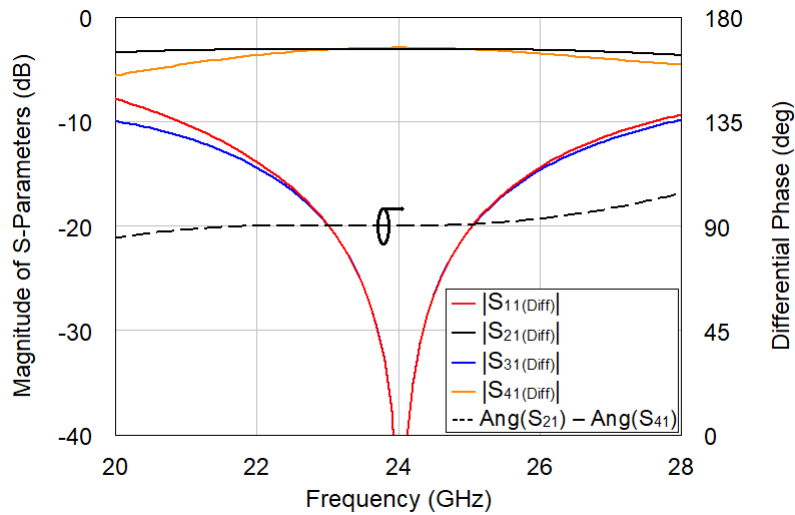
Figure 4.16: Differential scattering parameters of an ideal miniaturized differentially-fed branch-line coupler [46]. (Copyright © 2020, MDPI)
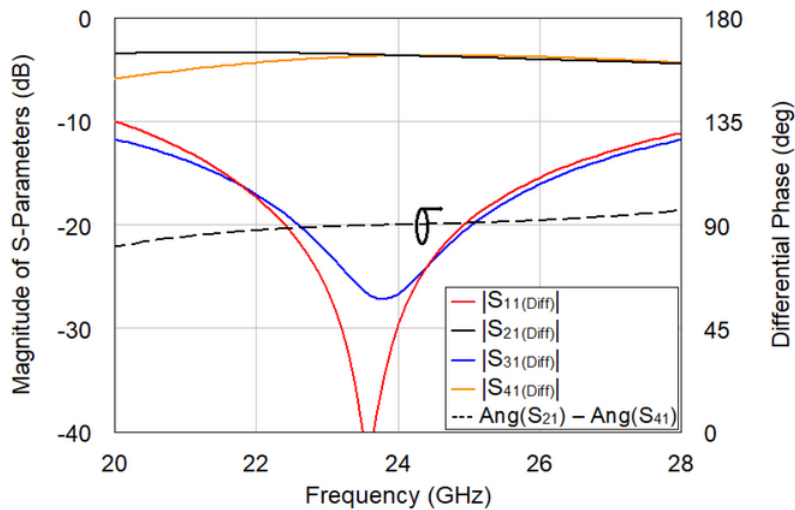
Figure 4.17: Scattering parameters (solid lines) and differential phase (dashed line) obtained during electromagnetic simulations of the differentially-fed branch-line coupler [46]. (Copyright © 2020, MDPI)

The response of an ideal 3-dB branch-line directional coupler operating at the 24 GHz center frequency is presented in Fig. 4.16. The obtained characteristics have been derived for the following calculated electrical parameters: $Z_{0o1} = 69\ \Omega$, $Z_{0o2} = 61\ \Omega$, $C_1 = 0.161\ pF$, $C_2 = 0.136\ pF$, $\Theta_1 = 21.68°$, and $\Theta_2 = 17.07°$. The differential terminating impedances of all ports are equal to $Z_{Tdiff} = 50\ \Omega$. The

circuit has been designed using the PH25 process provided by UMS, and the coupled-line sections have been analyzed electromagnetically. The simulation results are presented in Fig. 4.17.

To make measurements possible by utilizing a single-ended wafer probe system, a simple balanced-unbalanced circuit (balun) composed of lumped elements has been designed. A schematic of such a circuit is presented in Fig. 4.18. The balun operates at the same center frequency as the branch-line coupler (24 GHz). The calculated parameters of the circuit are $C_{B1} = 0.133$ pH and $L_{B1} = 0.332$ nH. It is worth mentioning that the terminating impedances of the single-ended input and differential output are 50 Ω. According to results presented in Fig. 4.19, which were obtained during simulations, the balun features bandwidth exceeding 20% taken for return losses lower than 20 dB, whereas the bandwidth of the differentially-fed coupler operates within a 10% bandwidth. Therefore, the balun should not significantly modify the coupler's frequency response.
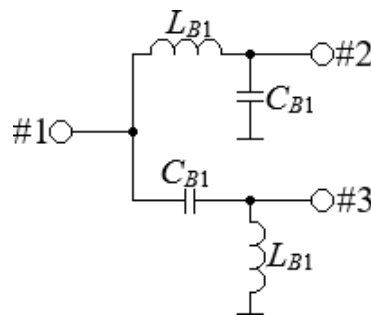
Figure 4.18: Schematic of a balanced-unbalanced (balun) circuit composed of lumped elements [46]. (Copyright © 2020, MDPI)
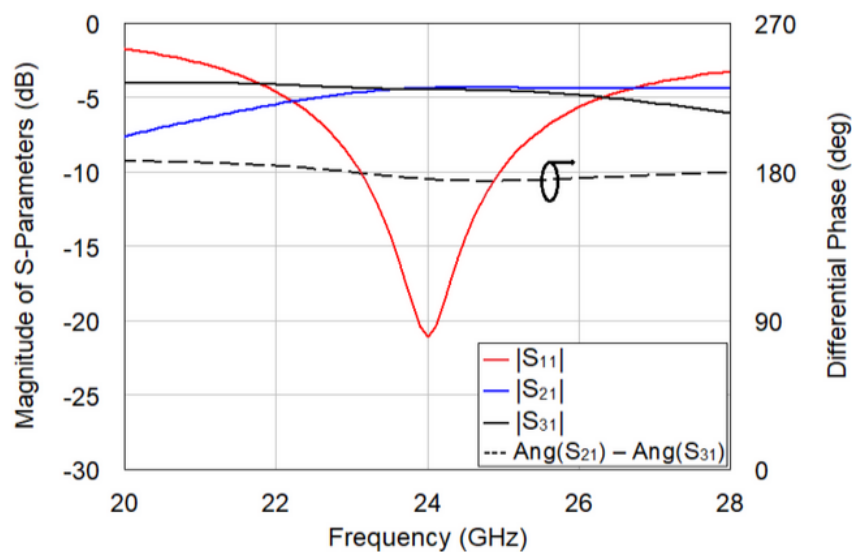
Figure 4.19: Scattering parameters (solid lines) and differential phase (dashed line) obtained during electromagnetic simulations of the LC balun [46]. (Copyright © 2020, MDPI)

(a)

(b)
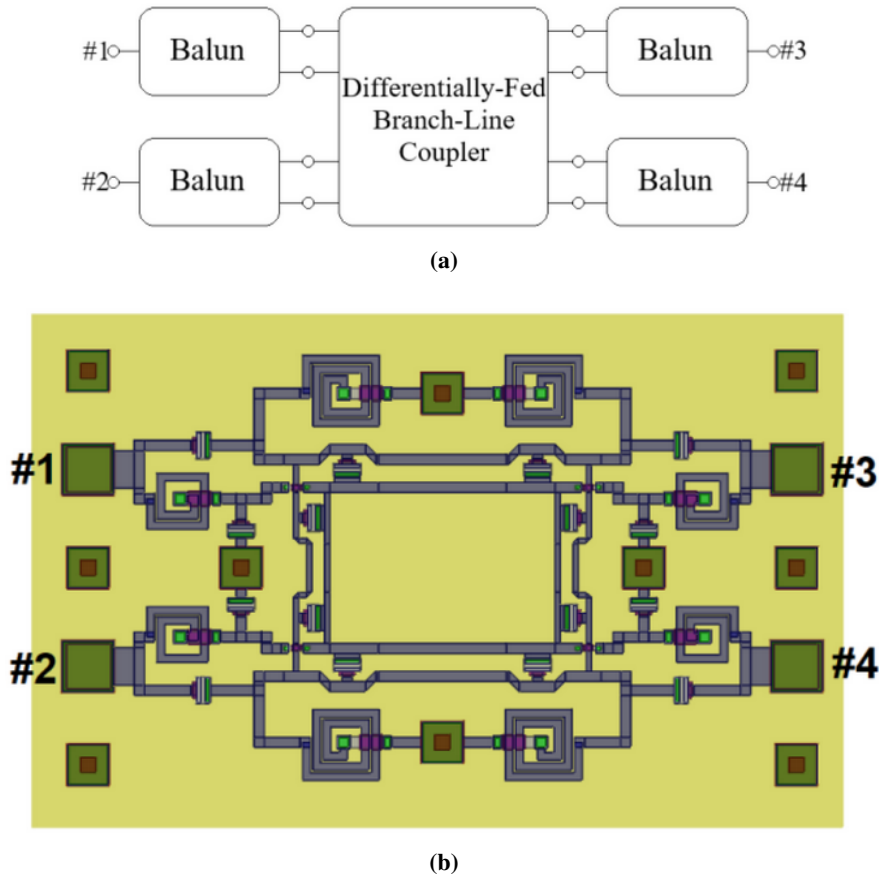
Figure 4.20: Schematic of the connection of a differentially-fed directional coupler with four lumped baluns for measurement purposes (a) and a layout of the designed monolithic branch-line coupler (b) [46]. (Copyright © 2020, MDPI)

As mentioned, the differentially-fed branch-line coupler was designed using the technology based on gallium arsenide substrate. The stack-up of the PH25 process has already been introduced in Section 2.2. A view presenting connections between the differentially-fed coupler and the baluns is shown in Fig. 4.20a and a layout of the designed die is presented in Fig. 4.20b. The electromagnetic simulations of the chip are shown together with measurements in Fig. 4.21. As can be seen, the obtained response of the branch-line hybrid coupler is in good agreement with the simulated response. Isolation and return losses of the simulated coupler are greater than 20 dB at the center frequency and the differential phase is $90°$. The obtained measurements confirm the simulations, and moreover, the observed transmission imbalance is not greater than 0.6 dB. However, the resonant frequency has been shifted towards higher frequencies of about 0.6 GHz. This is most likely caused by the accuracy of baluns' manufacturing, which, as narrowband circuits, are sensitive to lumped element values. Nevertheless, equal values of transmission and coupling at the center frequency confirm the proper operation of the coupler, which should operate well without baluns. The TEM photography presenting the fabricated die composed of the miniaturized monolithic branch-line hybrid coupler together with the baluns is shown in Fig. 4.22. The overall size of the chip is 630 μm x 487 μm.

(a)   (b)
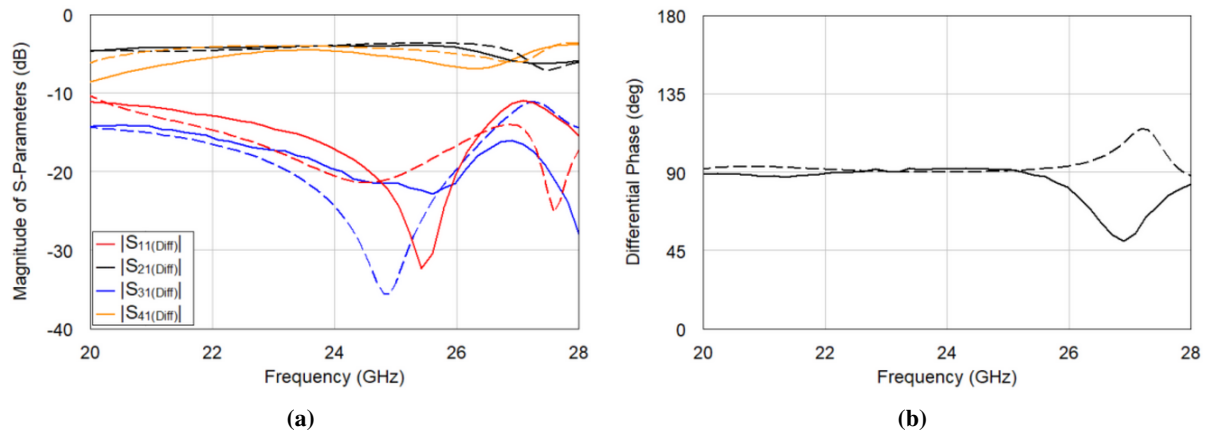
Figure 4.21: Calculated (dashed lines) and measured (solid lines) scattering parameters (a) and differential phases (b) of the designed miniaturized differentially-fed branch-line coupler together with the connected LC baluns 4.20b [46]. (Copyright © 2020, MDPI)
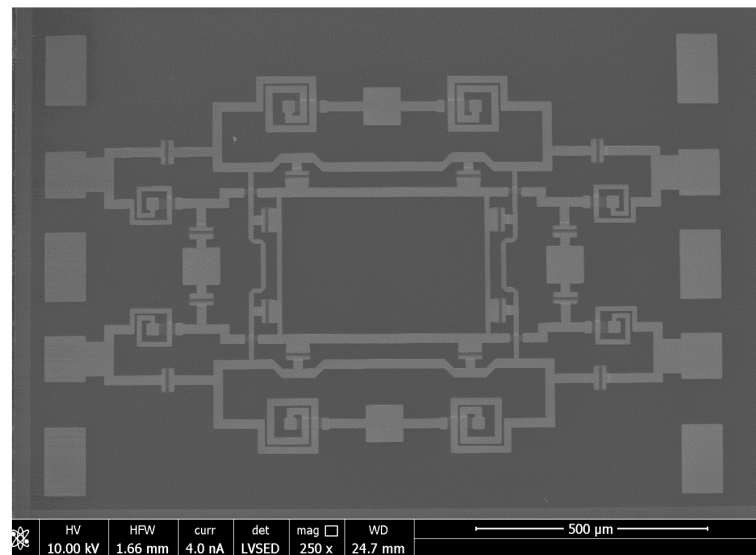
Figure 4.22: TEM photograph of the manufactured miniaturized monolithic branch-line coupler [46]. (Copyright © 2020, MDPI)

4.2.2. Monolithic Differentially-Fed Balanced Amplifier Design

Monolithic balanced amplifiers (MBA) have been the subject of intensive research for many years [102], [26], [2], [139], [85]. In the basic form, these components are composed of input and output combiners such as power dividers or directional couplers and amplifying stages. MBAs feature excellent impedance matching in the operational bandwidth of utilized combiners. Therefore, the parameters of the utilized couplers have a crucial impact on the electrical performance of the entire amplifier. Commonly designed balanced circuits are single-ended solutions such as those presented in the literature [26], [102], [85]. However, in radio systems where the reduction of crosstalk's and suppression of noise is crucial, differentially-fed amplifying stages have to be considered [1], [10], [152], [162].

This subsection is focused on the design of a differentially-fed monolithic balanced amplifier based on the gallium arsenide process. The proposed circuit is composed of the miniaturized branch-line

coupler presented in the previous subsection (4.2.1) to verify its applicability in balanced circuits. Furthermore, differential cascode amplifying stages have been used which are based on topology presented in [1].
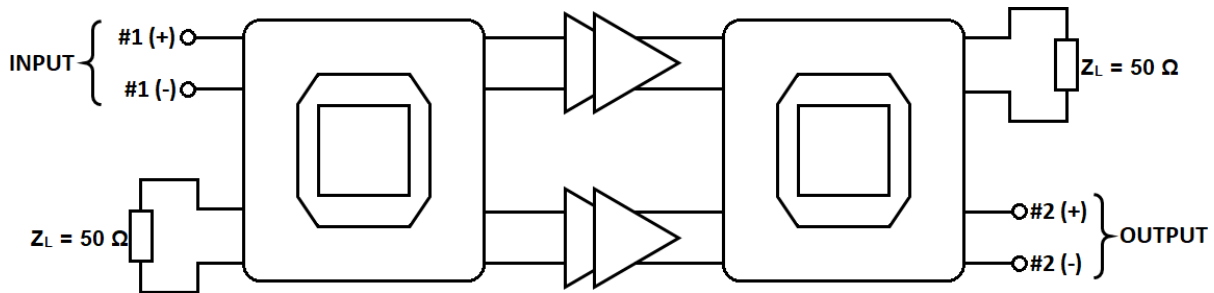
Figure 4.23: Concept view of the balanced two-stage differentially-fed amplifier.
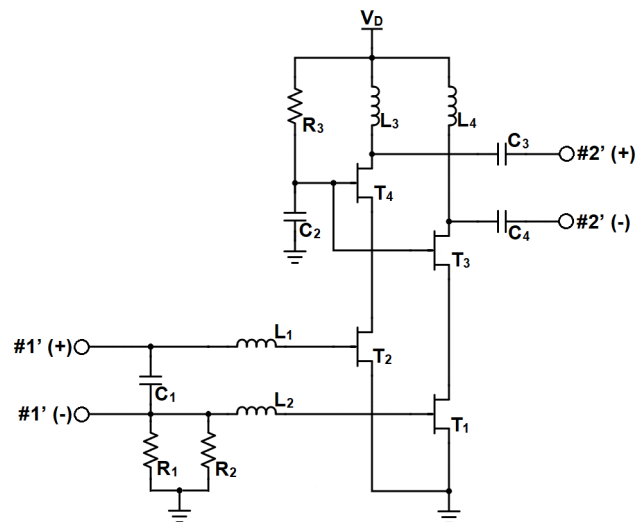
Figure 4.24: Schematic of single-stage cascode amplifier utilized in the considered differentially-fed balanced circuit.

Concept view of the balanced differentially-fed amplifier is presented in Fig. 4.23. The amplifier is composed of two differentially-fed branch-line couplers and two-stage amplifying blocks in each of quadrature channels. The isolation ports of couplers are terminated by 50 Ω resistors. Utilized branch-line couplers are based on the structure presented in the previous Subsection (4.2.1). Therefore, it features exactly the same frequency response as that presented in Fig. 4.17. The circuit schematic of a single amplifying stage which has been used is presented in Fig. 4.24 and is based on the concept introduced in the literature [1]. As it can be observed, the considered circuit is designed in the cascode topology, which has two main advantages. First, such a configuration reduces the impact of the Miller effect, and therefore increases the operational bandwidth of the amplifier. Secondly, it allows obtaining a higher output voltage swing without exceeding the recommended operational parameters of the utilized transistors. The presented single-stage is composed of four pHEMT transistors based on the gallium arsenide PH25 process provided by UMS Foundry. All utilized transistors are 48 μm four-finger structures. The amplifying stages have been biased to operate in A-class. To achieve such a condition, all stages are supplied by the same voltage applied on the transistor's drain: $V_{CC1} = V_{CC2} = V_{CC3} = V_{CC4} = 3$V.

Furthermore, gate biasing of the transistors are equal to 0V. The differentially-fed balanced amplifier has been designed to operate within the 22 - 24.5 GHz range frequency. The layout of the amplifier is shown in Fig. 4.25 where single amplifying stages are marked as the (A) areas and the utilized couplers are the (B) areas. The overall size of the chip is 2.4 x 4.0 mm.
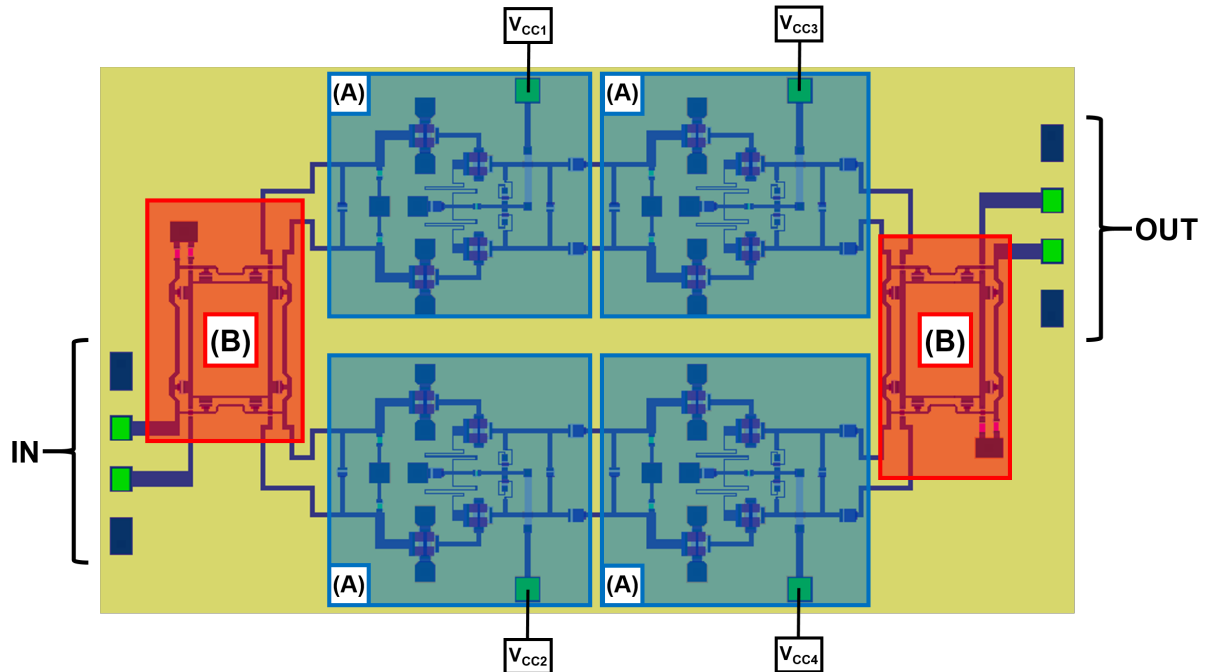
Figure 4.25: The layout of the monolithic differentially-fed balanced amplifier. The single differential amplifying stages are marked in blue (A) and the couplers occupy the red areas (B).
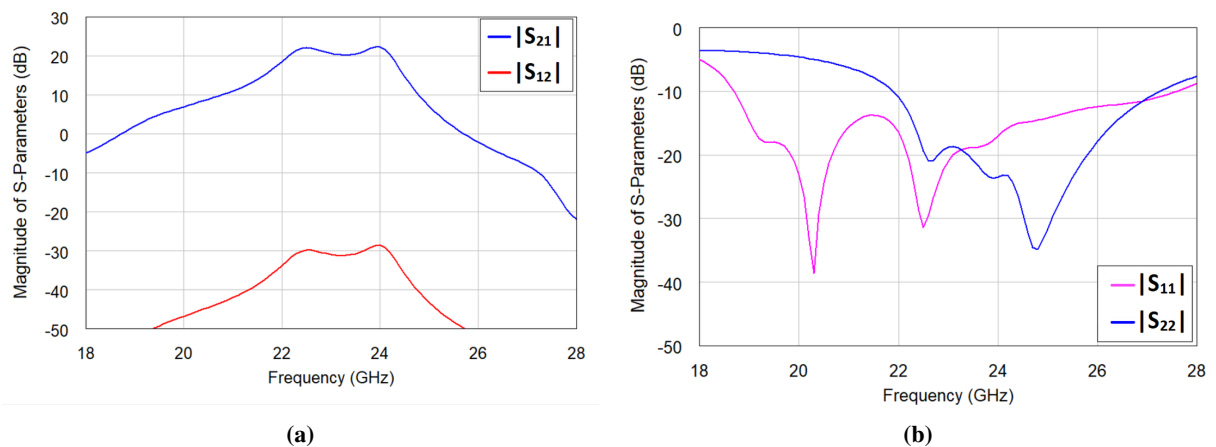
Figure 4.26: Simulated gain obtained for differential mode (a) and return losses (b) of the designed miniaturized differentially exceeded balanced amplifier designed in the PH25 process.

The obtained simulations presented in Fig. 4.26 show that gain obtained for the differential mode of the designed amplifier equals 21 dB and the reverse gain is not greater than -29.3 dB. The return losses are not greater than 10.2 dB in the operational bandwidth. Figure 4.27 shows the power-transfer functions obtained for operational frequencies f = 22, 23 and 24 GHz. The characteristics show that the maximum

available output power of the circuits reaches a value of 17.8 dBm and 17.4 dBm for 22 GHz and 24 GHz, respectively.
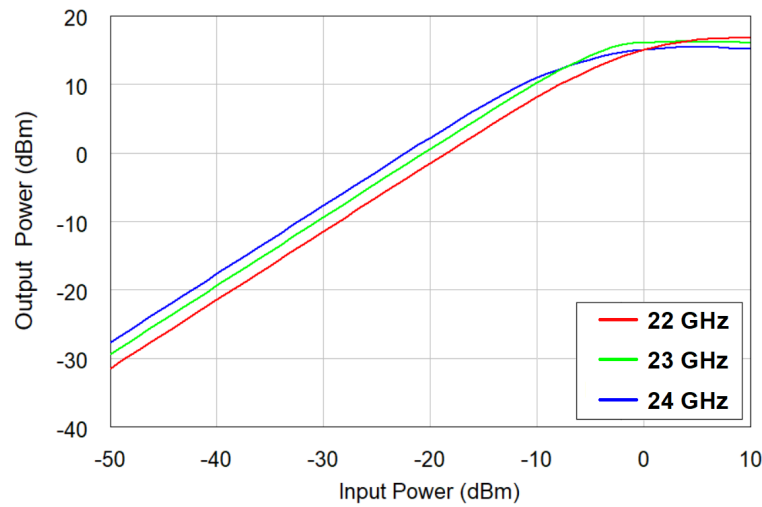
Figure 4.27: Input vs output power transfer characteristic of the monolithic differentially-fed balanced amplifier.

Figure 4.28 shows calculated 3rd intermodulation distortions (IMD3) together with the obtained levels of intercept points (OIP3). The characteristics were derived for three values of frequencies to verify the performance in the considered operational bandwidth. As can be observed, distortions do not exceed -45.3 dBm for all three cases. Moreover, the value of OIP3 is equal to 49.7 dB for the 22 GHz frequency, whereas 41.2 dB is achieved for the 24.5 GHz frequency. Furthermore, noise analysis has been conducted, and the results of the calculations are presented in Fig. 4.29. The noise figure (NF) of the balanced amplifier does not exceed 8.06 dB in the operational bandwidth and the lowest value is achieved for 22.7 GHz, where NF = 6.7 dB.

(a)	**(b)**
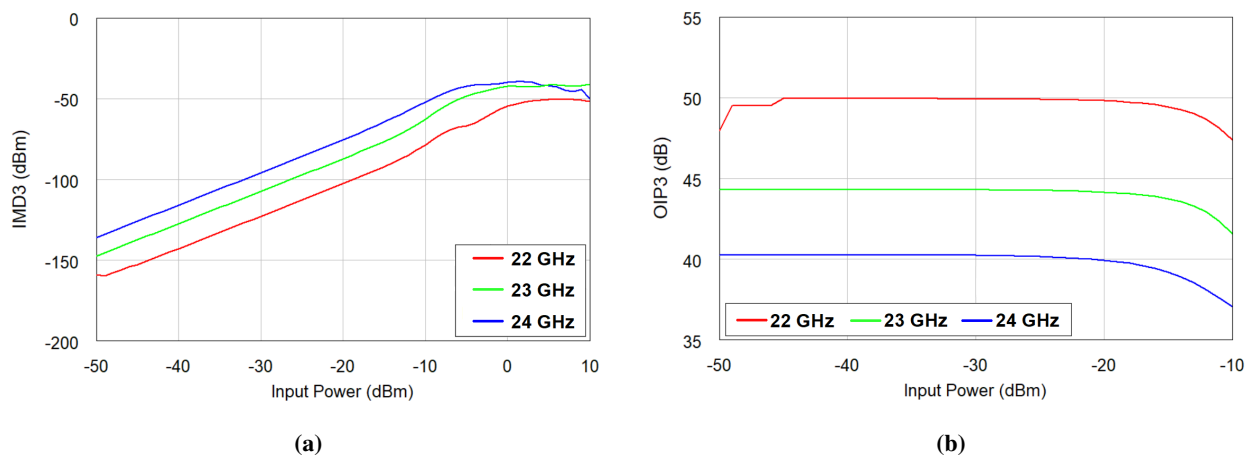
Figure 4.28: Calculated third-order intermodulation distortions level (a) and third-order intercept point (b) of the designed differentially-fed balanced monolithic amplifier. Results obtained for 22 GHz, 23 GHz and 24 GHz operational frequency.
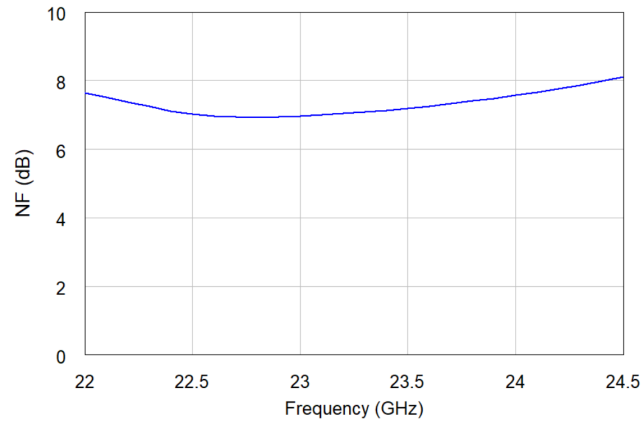
Figure 4.29: Noise figure calculated for the considered differentially excited balanced monolithic amplifier designed using the GaAs PH25 process.

4.3. Three-Conductor Compensated Directional Coupler Utilized in FMCW Radar Front-End

Sensors based on the FMCW radar concept (*frequency modulated contiuous-waveform radar*) are commonly utilized devices in different areas of engineering starting with automotive applications [72], [145], [150] and ending with medical measurements [151], [34]. Low energy consumption and compact dimensions are crucial for the development of such circuits. Therefore, the RF front-end of the radars are commonly applied in monolithic technologies [86], [27], [136], [79].

In this subsection, a simple FMCW radar operating at the 24 GHz center frequency is presented. The sensor has been designed using the mentioned PH25 process which is based on a GaAs substrate. A block diagram of the radar consisting of a *voltage controlled oscillator* (VCO), three amplifiers A_1, A_2, A_3, a mixer and a directional coupler is presented in Fig. 4.30. The radio frequency input port of the chip is named Rx and the radio transmitting output port is Tx. Moreover, the output signal operating in the baseband is received at the BB port, while the frequency of the Tx signal is controlled by an external DC voltage at the V_{TUNE} port. Power supply ports of active devices such as amplifiers are omitted in the concept schematic.
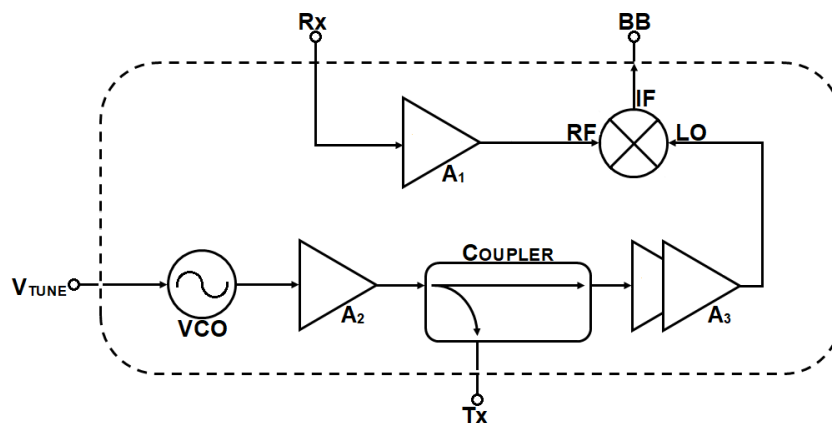
Figure 4.30: Block diagram of the proposed integrated FMCW radar front-end.
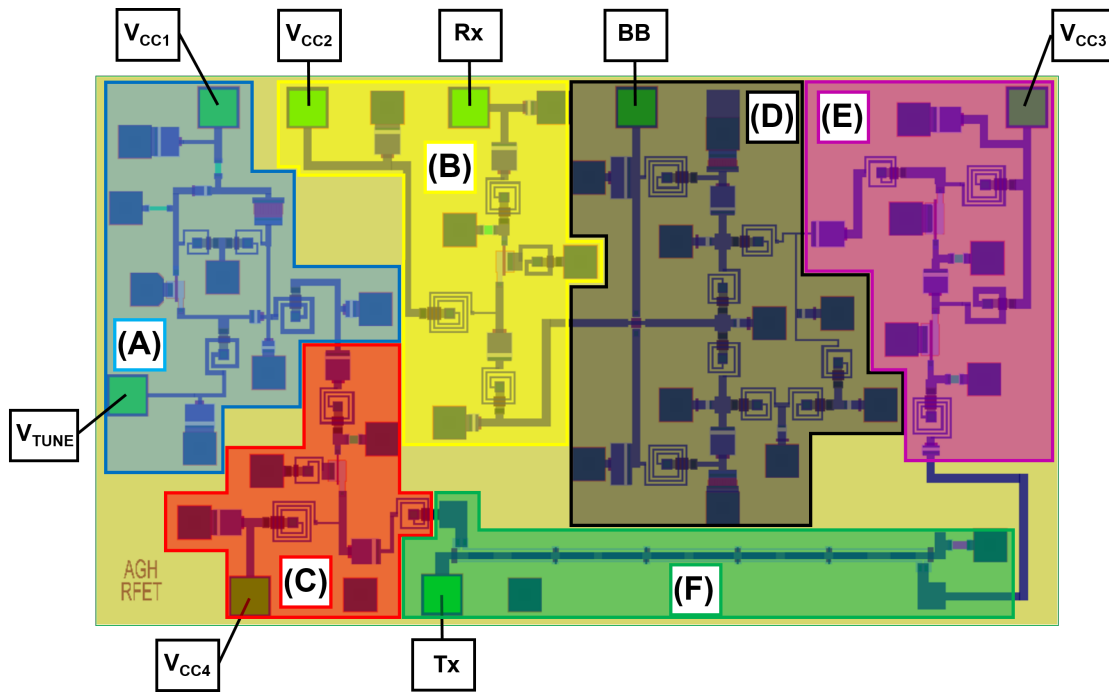
Figure 4.31: Layout of the integrated FMCW radar front-end designed using the PH25 gallium arsenide process provided by UMS.

The designed die which is presented in Fig. 4.31, occupies an area of 1.4 mm x 2.4 mm. The front-end has an internal signal source **(A)** which is directly controlled by an external biasing DC voltage, which can be derived from, for example, microcontroller. The utilized VCO is based on Hartley topology in which frequency control is achieved by capacitance changes of a diode in the resonant circuit of the oscillator. The resulting signal is amplified by a single-stage A-class amplifier composed of a two-finger pHEMT transistor **(C)** and supplied with a 2.24V voltage. Matching circuits of the amplifier have been designed using the lumped-elements technique in which spiral coils and MIM capacitors are used. The amplified signal feeds the power combiner, which in the considered radar is the 3-dB three-strip coupled-lines directional coupler presented in Subsection 2.2.2 **(F)**. The coupler divides the signal between the transmitting antenna port T_x and the internal reference signal which is once again amplified by a two-stage A-class amplifier **(E)**. The amplifier has to be supplied by a 3V power source. A second amplification is necessary for the proper operation of a single-balanced diode mixer **(D)**. Finally, the block **(B)** is the receiving amplifier which is responsible for the amplification of the received RF signal from the antenna (connected to the Rx port).

The designed FMCW radar front-end operating at the 24 GHz center frequency has been fabricated and subsequently measured. Due to the fact, that the chip has numerous ports which have to be connected with external devices, the on-chip measurements can be difficult to perform. Therefore, to simplify the measurements the die was mounted and bonded to the prepared PCB circuit.

First, the intermediate signal at the BB port was measured in terms of the VCO tuning voltage changes 4.32. The results have been compared to the simulations according to which, the generator allows a change of frequency from 23.35 GHz to 24.55 GHz and the output power at the T_x port has a value of 6.05 dBm. The measured operational frequency range of the chip is similar to the simulated

range which starts from 23.5 GHz and ends at 24.55 GHz. The measured output power is not as stable as it is in simulations. It can be seen, that for small values of biasing voltage i.e. not greater than 0.25 V, the power does not exceed 4.3 dBm. In range V_{TUNE} = 0.5 - 0.9 V the output power is similar to the results obtained during simulations.

(a) **(b)**
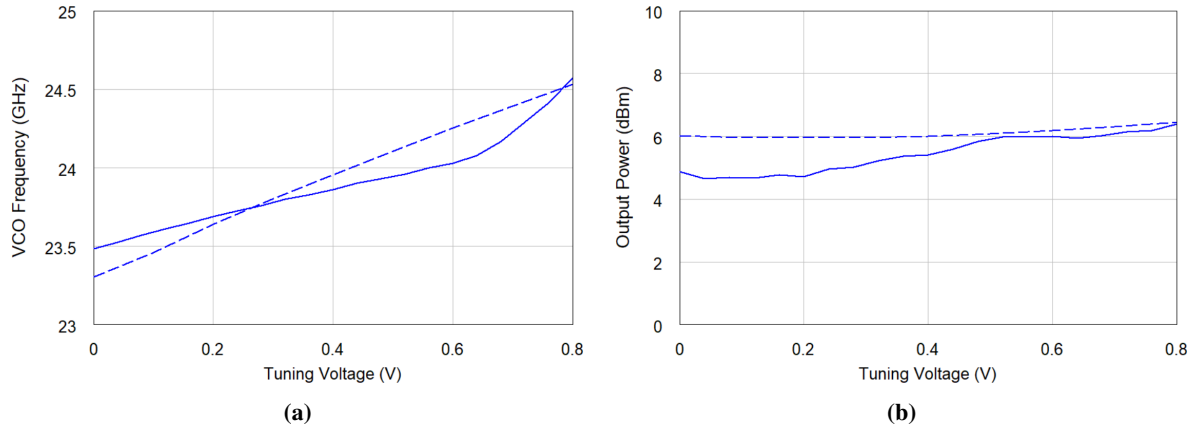
Figure 4.32: Influence of tuning voltage on Tx frequency (a) and power (b). Results obtained during simulations (dashed lines) and measurements of the fabricated die (solid lines).

(a) **(b)**
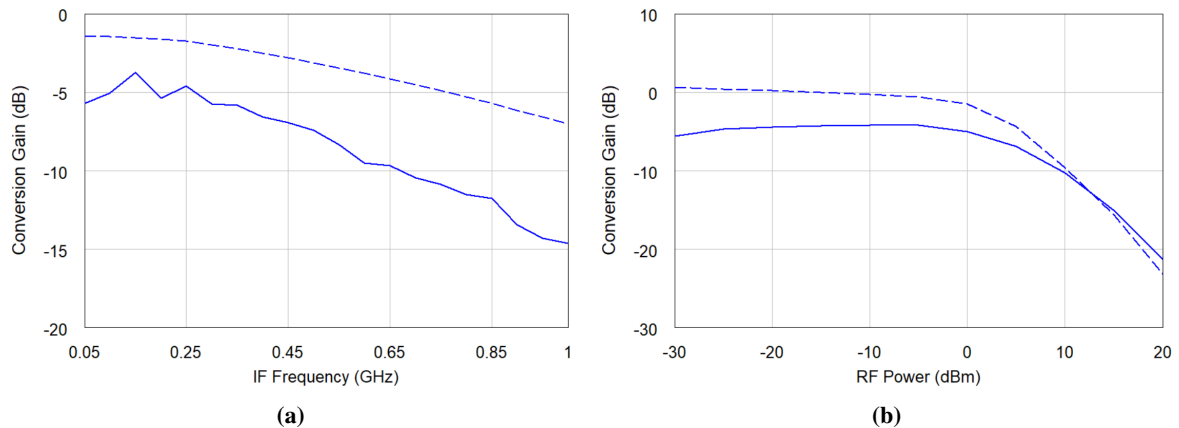
Figure 4.33: Conversion gain obtained for various intermediate frequencies (a) and RF powers at Rx port (b). Dashed lines were calculated from simulations and solid lines were obtained from measurements.

Figure 4.33 shows the simulated and measured conversion gain of the designed chip. The characteristics presented in Fig. 4.33a have been calculated assuming that the local oscillator has a frequency of 24 GHz and the RF signal received at the Rx port varies from 24.05 GHz to 25 GHz with power equal to 0 dBm. It can be observed that the conversion gain calculated during simulations is not lower than -7 dB in the considered range of the intermediate frequency, whereas the measurements show that such a parameter is not lower than -14.7 dB. Figure 4.33b presents the conversion gain computed for the case where the intermediate frequency is equal to 50 MHz, and the received RF power changes in the range of -30 dBm to 20 dBm. It can be seen that the obtained gain has relatively small fluctuations of up to 0 dBm, and after exceeding this value it decreases. The maximum difference in values between the simulated and measured results are not greater than 5.5 dB. Figure 4.34 shows the phase noise measured

at the Tx port for an operational frequency of 24 GHz. A photograph presenting the fabricated monolithic FMCW radar front-end operating at 24 GHz frequency is shown in Fig. 4.35.
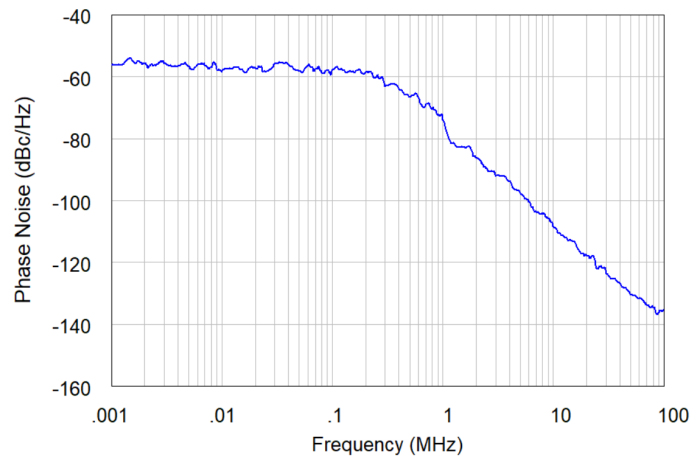
Figure 4.34: Phase noise measured at the *Tx* port of the designed 24 GHz monolithic FMCW radar front-end.
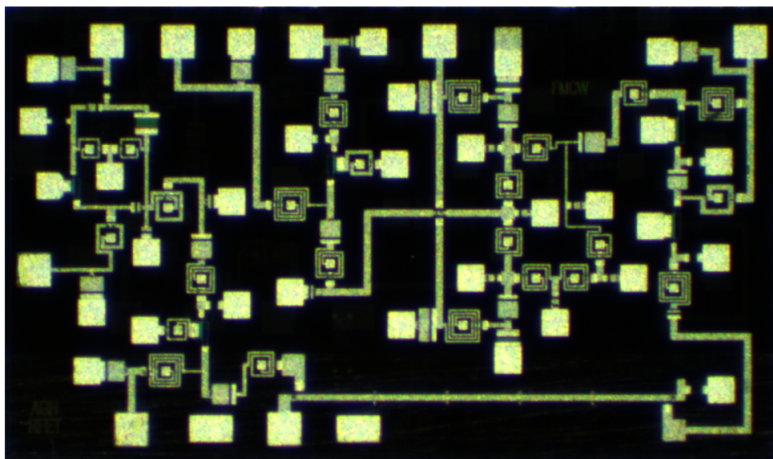
Figure 4.35: Photograph of the designed monolithic FMCW radar front-end utilized in the PH25 GaAs process.

4.4. Conclusions

In this chapter, three monolithic applications utilizing improved directional couplers have been presented. The first section focused on the design of a monolithic integrated sensor intended for dielectric permittivity measurements [121]. In the design, miniaturized lumped-elements branch-line couplers were utilized. The usage of such an approach in a monolithic circuit significantly reduces the overall size of the die. In the next section, the differentially-fed balanced amplifier consisting of miniaturized branch-line couplers has been shown. The utilized hybrid is based on a novel design presented in [46]. Finally, the FMCW radar front-end was shown in which the 3-dB compensated three-coupled-line coupler has been used [44]. It has been proven, that the proposed coupler can be used in complex circuits with good agreement with the simulations and moreover, it provides a good overall performance of the chip.

5. Summary

In this thesis, an investigation on the improved directional couplers designed in PCB and monolithic technologies has been presented. The thesis contains three main topics which are related to the design of high-performance directional couplers, impedance-transforming couplers and the applicability of the proposed couplers in monolithic complex circuits. Several novel approaches have been proposed together with appropriate numerical analysis which have been verified by simulations and physical realizations.

The author investigated the possibility of improvement of the single-ended and differentially-fed directional couplers by utilizing the capacitive compensation method and appropriate stack-up stratification. The compensation method has been used in the low-loss suspended microstrip technique for two different cases: a two-coupled-conductor section and a four-coupled-conductor Lange structure. It has been proven than the proposed approach improves the electrical performance of the couplers, which can be noticed in the increase of isolation and return losses. Moreover, a modified compensation method has also been used in monolithic technology, where three topologies were realized in the gallium arsenide process.

The improvement of the differentially-fed couplers realized in the homogeneous and inhomogeneous medium has been also studied. The author proposes a novel topology of a differentially excited tandem coupler designed using homogeneous stratification. Furthermore, symmetric and asymmetric two-coupled-conductor sections have been realized in inhomogeneous structures. In the first case, an investigation on the equalization of modal dielectric permittivies by a proper ratio between layer thicknesses of the stripline structure was conducted. In the second case, an additional compensation layer was proposed to equalize the capacitive and inductive coupling coefficients of the coupler.

Regarding impedance-transforming couplers, the author proposed three novel approaches based on impedance-transforming tandem-connected, narrow and broadband versions of rat-race couplers. It has been shown that tandem topology can achieve an impedance-transforming ratio greater than in the classic case, where $R = 2$. Moreover, it has been proven that such a coupler has a similar frequency response as a two-section structure. As previously mentioned, the author also investigated the directly-connected hybrid couplers and the possibility of their application as impedance-transforming components. It has been shown, that a narrowband version of such a coupler features such an ability without any additional elements. Moreover, to enhance operational bandwidth, the rat-race coupler needs only two coupled-line sections connected to the opposite ports of the coupler.

Additionally, the thesis shows the implementation of the proposed improved directional couplers in complex monolithic circuits such as: monolithic sensor systems, balanced amplifiers and FMCW radar

front-ends. For the purposes of this thesis, the author designed a differentially-fed balanced amplifier consisting of the novel miniaturized branch-line coupler. The single-ended branch-line coupler designed using a lumped-elements technique has been utilized in a monolithic sensor which is composed of a sensing part integrated with measurement circuitry based on a five-port correlator. In the FMCW radar front-end, the compensated three-strip coupled-line directional coupler has been utilized to increase the overall electrical performance of the chip. Both circuits have been designed in the gallium arsenide PH25 process provided by UMS.

The original achievements of the author presented in this thesis can be summarized as follows:

- the development of single-ended low-loss compensated directional couplers [122];

- the development of multi-strip low-loss compensated coupled-line directional couplers [65];

- the development of high-performance monolithic coupled-line directional couplers [44];

- the development of differentially-fed tandem-connected directional couplers in the homogeneous structure [126];

- the development of differentially-fed symmetric and asymmetric directional couplers based on the inhomogeneous stratifications [128], [45];

- the development of impedance-transforming tandem-connected directional coupler [125];

- the development of impedance-transforming narrowband and broadband rat-race couplers designed using microstrip and suspended microstrip (low-loss version) techniques [124],[123];

- the development of a monolithic integrated sensor with built-in calibration capability [121];

- the development of a miniaturized monolithic branch-line coupler [46];

- the development of a monolithic differentially-fed balanced amplifier based on a gallium arsenide substrate;

- the development of a monolithic FMCW radar front-end operating at the 24 GHz center frequency based on a gallium arsenide substrate.

Further research will be focused on the realization of high-performance broadband combined amplifiers such as multiport networks [89], [81], balanced [69], [139] and unbalanced [100] topologies, designed using PCB and monolithic technologies. In such circuits, directional couplers are utilized as one of the main components and have a direct influence on the entire performance of the amplifier. The preliminary results presented in Section 4.2 show that one of the developed couplers can be utilized in monolithic amplifiers based on gallium arsenide, and features good electrical-performance. However, such a solution is not suitable for high-power applications. Thus, the author plans to include gallium nitride processes in future research.

Another promising direction of further research can be found in the design of monolithic low-power consumption radars and sensors intended for the measurement of biological samples. The preliminary

results presented in the literature[121] and Section 4.2 show that such circuits can be designed in monolithic processes. However, further development is required in terms of improved performance.

Author's Achievements

JOURNAL PAPERS FOCUSED DIRECTLY ON THE DISSERTATION'S SUBJECT:

- R. Smolarz, K. Staszek, K. Wincza, and S. Gruszczynski "A 24 GHz microwave sensor with built-in calibration capability designed in MMIC technology," *IEEE Access*, vol. 9, pp. 31513-31524, February 2021.

- R. Smolarz, K. Wincza, and S. Gruszczynski "Modal phase velocity compensation in multilayer differentially fed directional couplers," *Microwave and Optical Technology Letters*, vol. 62, no. 5, pp. 1882-1887, May 2020.

- S. Gruszczynski, R. Smolarz, and K. Wincza, "Differential Bi-Level Microstrip Directional Coupler with Equalized Coupling Coefficients for Directivity Improvement," *Electronics*, vol. 9, no. 4, pp. 547-, March 2020.

- S. Gruszczynski, R. Smolarz, C. Wu, and K. Wincza, "Monolithic Miniaturized Differentially-Fed Branch-Line Directional Coupler in GaAs Monolithic Technology," *Electronics*, vol. 9, no. 3, pp. 446-, March 2020.

- S. Gruszczynski, R. Smolarz, and K. Wincza, "Realization of high-performance broadband quadrature directional couplers in UMS PH25 technology," *Electronics*, vol. 8, no. 12, pp. 1520-, December 2019.

- R. Smolarz, K. Wincza and S. Gruszczynski, "Impedance transforming rat-race couplers with modified Lange secton," *Journal of Electromagnetic Waves and Applications*, vol. 32, no. 8, pp. 972–983, May 2018.

- R. Smolarz, K. Wincza and S. Gruszczynski, "Impedance transforming tandem couplers with increased bandwidth and transformation ratio," *IEEE Microwave and Wireless Components Letters*, vol. 28, no. 4, pp. 299–301, March 2018.

- R. Smolarz, K. Wincza and S. Gruszczynski, "Design of low-loss durectional couplers with compensated coupled-line sections in suspended microstrip technique," *International Joutnal of RF and Microwave Computer-Aided Engineering*, vol. 27, no. 8, October 2017.

JOURNAL PAPERS NOT RELATED TO THE DISSERTATION'S SUBJECT:

- I. Piekarz, J. Sorocki, R. Smolarz, S. Gruszczynski and K. Wincza, "Four-node antenna feeding network for interfacing with differential front-end electronics," *IEEE Access*, Accepted for publication, June 2021.

- R. Smolarz, S. Gruszczynski, and K. Wincza, "Multisection ultra-broadband directional coupler designed in MMIC technology," *IEEE Access*, vol. 9, pp. 33478-33486, February 2021.

- R. Smolarz, K. Wincza and S. Gruszczynski, "Chebyshev-response branch-line couplers with enhanced bandwidth and arbitrary coupling level," *Electronics*, vol. 9, no. 11, pp. 1828 -, November 2020.

CONFERENCE COMMUNICATES FOCUSED DIRECTLY ON THE DISSERTATION'S SUBJECT:

- R. Smolarz, K. Wincza, and S. Gruszczynski, "Design of 3-dB Differentially-Fed Tandem Directional Couplers," in *Proc. of the IEEE MTT-S International Wireless Symposium (IWS)*, Guangzhou, China, May 2019, pp. 1–3.

- R. Smolarz, K. Wincza, and S. Gruszczynski, "Broadband low-loss impedance transforming rat-race coupler in suspended microstrip technique," in *Proc. of the 22nd International Microwave and Radar Conference (MIKON)*, Poznan, Poland, May 2018, pp. 291–293.

- K. Janisz, R. Smolarz, A. Rydosz, K. Wincza, and S. Gruszczynski, "Compensated 3-dB lange directional coupler in suspended microstrip technique," in *Proc. of the 7th IEEE International Symposium on Microwave, Antenna, Propagation, and EMC Technologies (MAPE) 2017*, Xi'an, China, October 2017, pp. 289–291.

CONFERENCE COMMUNICATES NOT RELATED TO THE DISSERTATION'S SUBJECT:

- R. Smolarz, S. Gruszczynski, and K. Wincza, "Design of Broadband Reduced-Length Directional Couplers Consisting Indirectly Coupled Lines Sections for Planar and MMIC Applications," in *Proc. of the 23rd International Microwave and Radar Conference (MIKON) 2020*, Warsaw, Poland, October 2020, pp. 53–55.

- R. Smolarz, K. Wincza, S. Gruszczynski, and K. Staszek, "Ultra-Wideband Multiprobe Reflectometer Designed in MMIC Technique," in *Proc. of the IEEE Asia-Pacific Microwave Conference (APMC) 2019*, Singapore, December 2019, pp. 1220–1222.

- K. Wincza, R. Smolarz, and S. Gruszczynski, "Broadband Differentially-Fed Directional Coupler Composed of Coupled and Uncoupled Sections," in the *Proc. of the IEEE Asia-Pacific Microwave Conference (APMC) 2019*, Singapore, December 2019, pp. 1131–1133.

- S. Gruszczynski, K. Wincza, and R. Smolarz, "Design of Bi-Level-Microstrip Quadrature Directional Couplers with Indirectly Coupled Lines," in *Proc. of IEEE Asia-Pacific Microwave Conference (APMC) 2019*, Singapore, Poland, December 2019, pp. 1437–1439.

- S. Gruszczynski, R. Smolarz, A. Rydosz, and K. Wincza, "Broadband Differentially-Fed Substrate-Integrated Directional Coupler," in *Proc. of the Conference on Microwave Techniques (COMITE) 2019*, Pardubice, Czech Republic, April 2019, pp. 1–3.

- K. Janisz, R. Smolarz, J. Sorocki, K. Wincza and S. Gruszczynski, "Deferentially-fed band-pass filter with common mode rejection," in *Proc. of the 22nd International Microwave and Radar Conference (MIKON) 2018*, Poznan, Poland 2018, pp. 644–645.

- R. Smolarz, K. Staszek and S. Gruszczynski, "Broadband rat-race coupler in suspended stripline technique for measurements of large-signal S parameters," in *Proc. of the 21st International Conference on Microwave, Radar and Wireless Communications (MIKON) 2016*, Krakow, Poland, May 2016, pp. 1–3.

PARTICIPATION IN RESEARCH PROJECTS:

- Research Project "Broadband directional couplers in differentially fed symmetrical coupled-lines technique" granted by National Science Center and realized at AGH University of Science and Technology in 2017-2020 - Investigator.

- Research Project "Research on measurement methods and design of biofunctional microwave systems that create microbiological sensors" granted by National Science Center and realized at AGH University of Science and Technology in 2017-2022 - Investigator.

- Research Project "Microwave multiport measurement systems for sensor applications" granted by the National Science Center under SONATA 12 Program realized at the AGH University of Science and Technology in 2017-2020 - Investigator.

- Research Project "Investigation on quasi-ideal coupled-line sections' realization in monolithic technologies and their utilization in the design of microwave integrated circuits" granted by the National Science Center under OPUS 16 Program realized at the AGH University of Science and Technology in 2018-2021 - Investigator.

PRIZES AND AWARDS:

- Distinguished by the Rector of AGH University of Science and Technology for the didactic activities in 2019.

- Title of *The Best Teacher of 2019* - awarded by the Institute of Electronics (AGH University of Science and Technology)

- Scholarships for the best PhD students awarded for the 4th year of PhD studies.

- Faculty scholarships awarded for the 1st, 3rd and 4th year of PhD studies.

- Pro-quality scholarships awarded for the 3rd and 4th year of PhD studies.

- Dean's Grants awarded in 2016 and 2018.

SCIENTIFIC AND INDUSTRIAL CAREER:

- Research Assistant (2018 -)
  AGH University of Science and Technology, Institute of Electronics, Poland
  Role: Researcher specializing in the development of high-performance microwave passive components utilized in power division circuits, and Monolithic Microwave Integrated Circuits (MMIC) design.

- Telecom Software Test Engineer (2016 - 2018)
  Nokia R&D Center, Poland
  Role: Quality Assurance (QA) Engineer, specializing in call processing, call-control and scheduler of the LTE-A standard, especially in Cat-M features.

- Telecom Software Engineer (2015 - 2016)
  Samsung Electronics, Poland
  Role: Integration and Quality Assurance (QA) engineer, specializing in call processing and call-control features of the UMTS and the Samsung pre-5G cellular standards, the 5G physical layer specialist.

Bibliography

[1] M. Abbasi, T. Kjellberg, A. de Graauw, E. van der Heijden, R. Roovers and H. Zirath, "A broadband differential cascode power amplifier in 45 nm cmos for high-speed 60 ghz system-on-chip," in *2010 IEEE Radio Frequency Integrated Circuits Symposium*.   IEEE, 2010, pp. 533–536.

[2] S. Abdelnaby, A. Freundorfer and Y. Antar, "Lumped element model of a transdirectional coupled line coupler," in *2018 18th International Symposium on Antenna Technology and Applied Electromagnetics (ANTEM)*.   IEEE, 2018, pp. 1–2.

[3] H.-R. Ahn and B. Kim, "Transmission-line directional couplers for impedance transforming," *IEEE microwave and wireless components letters*, vol. 16, no. 10, pp. 537–539, 2006.

[4] H.-R. Ahn and B. Kim, "Toward integrated circuit size reduction," *IEEE Microwave Magazine*, vol. 9, no. 1, pp. 65–75, 2008.

[5] H.-R. Ahn and S. Nam, "Wideband microstrip coupled-line ring hybrids for high power-division ratios," *IEEE transactions on microwave theory and techniques*, vol. 61, no. 5, pp. 1768–1780, 2013.

[6] H.-R. Ahn and S. Nam, "Wideband microstrip coupled-line ring hybrids for high power-division ratios," *IEEE transactions on microwave theory and techniques*, vol. 61, no. 5, pp. 1768–1780, 2013.

[7] S. Al-Taei, P. Lane and G. Passiopoulos, "Design of high directivity directional couplers in multilayer ceramic technologies," in *2001 IEEE MTT-S International Microwave Sympsoium Digest (Cat. No. 01CH37157)*, vol. 1.   IEEE, 2001, pp. 51–54.

[8] F. Ali and A. Podell, "A wide-band gaas monolithic spiral quadrature hybrid and its circuit applications," *IEEE Journal of Solid-State Circuits*, vol. 26, no. 10, pp. 1394–1398, 1991.

[9] M. Arain and N. Spencer, "Tapered asymmetric microstrip magic tee (short papers)," *IEEE Transactions on Microwave Theory and Techniques*, vol. 23, no. 12, pp. 1064–1067, 1975.

[10] M. Arsalan, A. Shamim, L. Roy and M. Shams, "A fully differential monolithic lna with on-chip antenna for a short range wireless receiver," *IEEE microwave and wireless components letters*, vol. 19, no. 10, pp. 674–676, 2009.

[11] I. J. Bahl, E. L. Griffin, J. Dilley and M. Balzan, "Low loss multilayer microstrip line for monolithic microwave integrated circuits applications," *International Journal of RF and Microwave Computer-Aided Engineering: Co-sponsored by the Center for Advanced Manufacturing and Packaging of Microwave, Optical, and Digital Electronics (CAMPmode) at the University of Colorado at Boulder*, vol. 8, no. 6, pp. 441–454, 1998.

[12] S. Banba, T. Hasegawa and H. Ogawa, "Multilayer mmic branch-line hybrid using thin dielectric layers," *IEEE Microwave and guided wave letters*, vol. 1, no. 11, pp. 346–347, 1991.

[13] T. Bertuch, "Backward directional coupler for weak coupling of double-sided microstrip lines using longitudinal double-slots," *Electronics Letters*, vol. 40, no. 5, pp. 309–310, 2004.

[14] D. E. Bockelman and W. R. Eisenstadt, "Combined differential and common-mode scattering parameters: Theory and simulation," *IEEE transactions on microwave theory and techniques*, vol. 43, no. 7, pp. 1530–1539, 1995.

[15] D. E. Bockelman and W. R. Eisenstadt, "Pure-mode network analyzer for on-wafer measurements of mixed-mode s-parameters of differential circuits," *IEEE Transactions on Microwave Theory and Techniques*, vol. 45, no. 7, pp. 1071–1077, 1997.

[16] S.-F. Chang, J.-L. Chen, Y.-H. Jeng and C.-T. Wu, "New high-directivity coupler design with coupled spurlines," *IEEE microwave and wireless components letters*, vol. 14, no. 2, pp. 65–67, 2004.

[17] J.-L. Chen, S.-F. Chang and C.-T. Wu, "A high-directivity microstrip directional coupler with feedback compensation," in *2002 IEEE MTT-S International Microwave Symposium Digest (Cat. No. 02CH37278)*, vol. 1.   IEEE, 2002, pp. 101–104.

[18] S. Chen and Q. Xue, "Compact triple-transistor doherty amplifier designs: differential/power combining," *IEEE transactions on microwave theory and techniques*, vol. 61, no. 5, pp. 1957–1963, 2013.

[19] M.-J. Chiang, H.-S. Wu, M.-L. Lee and C.-K. C. Tzuang, "Design of compact ka-band monolithic branch-line coupler on silicon substrate," in *2009 Asia Pacific Microwave Conference*.   IEEE, 2009, pp. 2124–2127.

[20] M. Chongcheawchamnan, V. Chamnanphrai and R. Phromloungsri, "Wideband multi-section quadrupled inductive-compensated parallel-coupled lines," in *2006 Asia-Pacific Microwave Conference*.   IEEE, 2006, pp. 678–681.

[21] P.-J. Chou, Y.-W. Lin and C.-Y. Chang, "Exact synthesis of full-and half-symmetric rat-race ring hybrids with or without impedance transforming characteristics," *IEEE Transactions on Microwave Theory and Techniques*, vol. 63, no. 12, pp. 3971–3980, 2015.

[22] Y.-H. Chun, J.-Y. Moon, S.-W. Yun and J.-K. Rhee, "Microstrip line directional couplers with high directivity," *Electronics Letters*, vol. 40, no. 5, pp. 317–318, 2004.

[23] E. Cohen, A. Nazimov and S. Ravid, "Accurate power detector and dual directional coupler with self-calibration in 65nm cmos," in *2015 10th European Microwave Integrated Circuits Conference (EuMIC)*. IEEE, 2015, pp. 124–127.

[24] E. G. Cristal, "Coupled-transmission-line directional couplers with coupled lines of unequal characteristic impedances," *IEEE Transactions on Microwave Theory and Techniques*, vol. 14, no. 7, pp. 337–346, 1966.

[25] D. R. Daum, M. T. Buchanan, T. Fjield and K. Hynynen, "Design and evaluation of a feedback based phased array system for ultrasound surgery," *ieee transactions on ultrasonics, ferroelectrics, and frequency control*, vol. 45, no. 2, pp. 431–438, 1998.

[26] W. R. Deal, M. Biedenbender, P.-h. Liu, J. Uyeda, M. Siddiqui and R. Lai, "Design and analysis of broadband dual-gate balanced low-noise amplifiers," *IEEE Journal of Solid-State Circuits*, vol. 42, no. 10, pp. 2107–2115, 2007.

[27] B. Ding, S. Yuan, C. Zhao, L. Tao and T. Tian, "A ka band fmcw transceiver front-end with 2-ghz bandwidth in 65-nm cmos," *IEEE Transactions on Circuits and Systems II: Express Briefs*, vol. 66, no. 2, pp. 212–216, 2018.

[28] A. Djordjevic, M. Bazdar, R. Harrington and T. Sarkar, *Matrix parameters for multiconductor transmission lines: Software and user's manual*. Artech House, 1989.

[29] A. R. Djordjevic, M. B. Bazdar, T. K. Sarkar and R. F. Harrington, "Linpar for windows: Matrix parameters for multiconductor transmission lines," *Artech House, Boston*, 1999.

[30] X. Duan, W. Feng, Y. Zhao, W. Che and R. Gómez-García, "Single-band balanced coupler with wideband common-mode suppression," in *2018 International Conference on Microwave and Millimeter Wave Technology (ICMMT)*. IEEE, 2018, pp. 1–3.

[31] M. Dydyk, "Microstrip directional couplers with ideal performance via single-element compensation," *IEEE Transactions on microwave theory and techniques*, vol. 47, no. 6, pp. 956–964, 1999.

[32] T. Emery, Y. Chin, H. Lee and V. Tripathi, "Analysis and design of ideal non symmetrical coupled microstrip directional couplers," in *IEEE MTT-S International Microwave Symposium Digest*. IEEE, 1989, pp. 329–332.

[33] M. Engels and R. Jansen, "Design of quasi-ideal couplers using multilayer mmic technology," in *1996 IEEE MTT-S International Microwave Symposium Digest*, vol. 2. IEEE, 1996, pp. 1181–1184.

[34] G.-W. Fang, C.-Y. Huang and C.-L. Yang, "Switch-based low intermediate frequency system of a vital sign radar for simultaneous multitarget and multidirectional detection," *IEEE Journal of Electromagnetics, RF and Microwaves in Medicine and Biology*, vol. 4, no. 4, pp. 265–272, 2020.

[35] A. Ferrero and M. Pirola, "Generalized mixed-mode s-parameters," *IEEE Transactions on Microwave Theory and Techniques*, vol. 54, no. 1, pp. 458–463, 2006.

[36] L. Franti and G. Paganuzzi, "Wideband high directivity microstrip couplers for microwave integrated circuits," in *1980 10th European Microwave Conference*. IEEE, 1980, pp. 377–381.

[37] D. A. Frickey, "Conversions between s, z, y, h, abcd, and t parameters which are valid for complex source and load impedances," *IEEE Transactions on microwave theory and techniques*, vol. 42, no. 2, pp. 205–211, 1994.

[38] R. C. Frye, S. Kapur and R. C. Melville, "A 2-ghz quadrature hybrid implemented in cmos technology," *IEEE Journal of Solid-State Circuits*, vol. 38, no. 3, pp. 550–555, 2003.

[39] T. Fujii, Y. Kokubo and I. Ohta, "High directivity quarter-wave microstrip couplers with periodic floating-conductors on coupled edges," in *2006 European Microwave Conference*. IEEE, 2006, pp. 32–35.

[40] J. P. Gilb and C. A. Balanis, "Improved performance of microstrip couplers through multi-layer substrates," in *1993 23rd European Microwave Conference*. IEEE, 1993, pp. 624–626.

[41] M. Gillick, I. D. Robertson and J. S. Joshi, "Cpw two-stage balanced monolithic 15 ghz amplifier using reduced-size branchline couplers," in *1993 23rd European Microwave Conference*. IEEE, 1993, pp. 764–766.

[42] Y. Goto, N. Kobayashi and M. Fujishima, "On-chip rat-race balun with stubs for matching arbitrary terminal impedances," in *2007 Asia-Pacific Microwave Conference*. IEEE, 2007, pp. 1–4.

[43] S. Gruszczyński, *Design of Quasi-ideal Coupled Lines and Their Applications in High-performance Directional Couplers*. AGH University of Science and Technology Press, 2011.

[44] S. Gruszczynski, R. Smolarz and K. Wincza, "Realization of high-performance broadband quadrature directional couplers in ums ph25 technology," *Electronics*, vol. 8, no. 12, p. 1520, 2019.

[45] S. Gruszczynski, R. Smolarz and K. Wincza, "Differential bi-level microstrip directional coupler with equalized coupling coefficients for directivity improvement," *Electronics*, vol. 9, no. 4, p. 547, 2020.

[46] S. Gruszczynski, R. Smolarz, C. Wu and K. Wincza, "Monolithic miniaturized differentially-fed branch-line directional coupler in gaas monolithic technology," *Electronics*, vol. 9, no. 3, p. 446, 2020.

[47] S. Gruszczynski and K. Wincza, "Broadband rat-race couplers with coupled-line section and impedance transformers," *IEEE microwave and wireless components letters*, vol. 22, no. 1, pp. 22–24, 2011.

[48] S. Gruszczynski and K. Wincza, "Generalized methods for the design of quasi-ideal symmetric and asymmetric coupled-line sections and directional couplers," *IEEE transactions on microwave theory and techniques*, vol. 59, no. 7, pp. 1709–1718, 2011.

[49] S. Gruszczynski, K. Wincza and J. Borgosz, "Multilayer surface-mount 3db directional coupler for application in balanced modulators," in *2008 China-Japan Joint Microwave Conference*. IEEE, 2008, pp. 547–550.

[50] S. Gruszczynski, K. Wincza and K. Sachse, "Design of compensated coupled-stripline 3-db directional couplers, phase shifters, and magic-t's—part i: Single-section coupled-line circuits," *IEEE transactions on microwave theory and techniques*, vol. 54, no. 11, pp. 3986–3994, 2006.

[51] S. Gruszczynski, K. Wincza and K. Sachse, "Design of compensated coupled-stripline 3-db directional couplers, phase shifters, and magic-t's—part ii: Broadband coupled-line circuits," *IEEE transactions on microwave theory and techniques*, vol. 54, no. 9, pp. 3501–3507, 2006.

[52] S. Gruszczynski, K. Wincza and K. Sachse, "Design of high-performance three-strip 3-db directional coupler in multilayer technology with compensated parasitic reactances," *Microwave and Optical Technology Letters*, vol. 49, no. 7, pp. 1656–1659, 2007.

[53] S. Gruszczynski, K. Wincza and K. Sachse, "Design of a broadband low-loss coupled-line multisection symmetrical 3-db directional coupler in suspended stripline technology," in *2010 Asia-Pacific Microwave Conference*. IEEE, 2010, pp. 1228–1231.

[54] W. Guo, X. Zhu, H. Liu, R. Yue and S. Wang, "Effects of milk concentration and freshness on microwave dielectric properties," *Journal of Food Engineering*, vol. 99, no. 3, pp. 344–350, 2010.

[55] M. Hartmann, K. Seemann, H. Jager, E. Kolmhofer and R. Weigel, "Monolithic integration of microstrip line couplers for automotive radar applications at 77 ghz using a si-hbt technology," in *2006 Asia-Pacific Microwave Conference*. IEEE, 2006, pp. 811–816.

[56] Q. He, Y. Liu, S. Li, M. Su and Y. Wu, "A novel 180° rat-race hybrid with arbitrary power division for complex impedances," *Journal of Electromagnetic Waves and Applications*, vol. 27, no. 3, pp. 318–329, 2013.

[57] K. Hettak, G. A. Morin and M. G. Stubbs, "Compact mmic cpw and asymmetric cps branch-line couplers and wilkinson dividers using shunt and series stub loading," *IEEE transactions on microwave theory and techniques*, vol. 53, no. 5, pp. 1624–1635, 2005.

[58] H. J. Hindin and A. Rosenzweig, "3-db couplers constructed from two tandem connected 8.34-db asymmetric couplers (correspondence)," *IEEE Transactions on Microwave Theory and Techniques*, vol. 16, no. 2, pp. 125–126, 1968.

[59] H. Hindin and A. Rosenzweig, "3-db couplers constructed from two tandem connected 8.34-db asymmetric couplers (correspondence)," *IEEE Transactions on Microwave Theory and Techniques*, vol. 16, no. 2, pp. 125–126, 1968.

[60] A. Hirota, Y. Tahara and N. Yoneda, "A compact forward coupler using coupled composite right/left-handed transmission lines," *IEEE transactions on microwave theory and techniques*, vol. 57, no. 12, pp. 3127–3133, 2009.

[61] M. Hofmann, S. Linz, R. Weigel, G. Fischer and D. Kissinger, "A multiband 2-port vna for biomedical applications based on two six-port-junctions," in *2013 IEEE MTT-S International Microwave Symposium Digest (MTT)*. IEEE, 2013, pp. 1–4.

[62] M. Horno and F. Medina, "Multilayer planar structures for high-directivity directional coupler design," *IEEE transactions on microwave theory and techniques*, vol. 34, no. 12, pp. 1442–1449, 1986.

[63] J.-A. Hou and Y.-H. Wang, "A compact quadrature hybrid based on high-pass and low-pass lumped elements," *IEEE Microwave and Wireless components LETTERS*, vol. 17, no. 8, pp. 595–597, 2007.

[64] K. Janisz, I. Piekarz, K. Staszek, K. Wincza and S. Gruszczynski, "Differentially fed directional couplers with coupled-conductors of unequal widths," *IEEE Microwave and Wireless Components Letters*, vol. 28, no. 9, pp. 759–761, 2018.

[65] K. Janisz, R. Smolarz, A. Rydosz, K. Wincza and S. Gruszczynski, "Compensated 3-db lange directional coupler in suspended microstrip technique," in *2017 7th IEEE International Symposium on Microwave, Antenna, Propagation, and EMC Technologies (MAPE)*. IEEE, 2017, pp. 288–291.

[66] T. Jensen, V. Zhurbenko, V. Krozer and P. Meincke, "Coupled transmission lines as impedance transformer," *IEEE Transactions on microwave Theory and Techniques*, vol. 55, no. 12, pp. 2957–2965, 2007.

[67] H. Jeon, Y. Park, Y. Huang, J. Kim, K. Lee, C. Lee and J. S. Kenney, "A triple-mode balanced linear cmos power amplifier using a switched-quadrature coupler," *IEEE Journal of Solid-State Circuits*, vol. 47, no. 9, pp. 2019–2032, 2012.

[68] D. Ji and J. Kim, "A multiband directional coupler using soi cmos for rf front-end applications," *IEEE Microwave and Wireless Components Letters*, vol. 28, no. 2, pp. 126–128, 2018.

[69] J. Jin and S. S. H. Hsu, "A 0.18-μm cmos balanced amplifier for 24-ghz applications," *IEEE Journal of Solid-State Circuits*, vol. 43, no. 2, pp. 440–445, 2008.

[70] X. Jing and S. Sun, "Design of impedance transforming 90 degree patch hybrid couplers," in *2014 Asia-Pacific Microwave Conference*. IEEE, 2014, pp. 25–27.

[71] E. Jones, "Coupled-strip-transmission-line filters and directional couplers," *IRE Transactions on Microwave Theory and Techniques*, vol. 4, no. 2, pp. 75–81, 1956.

[72] Y. Ju, Y. Jin and J. Lee, "Design and implementation of a 24 ghz fmcw radar system for automotive applications," in *2014 International Radar Conference*. IEEE, 2014, pp. 1–4.

[73] S. Julrat and S. Trabelsi, "Portable six-port reflectometer for determining moisture content of biomass material," *IEEE Sensors Journal*, vol. 17, no. 15, pp. 4814–4819, 2017.

[74] C.-S. Kim, J.-S. Lim, D.-J. Kim and D. Ahn, "A design of single and multi-section microstrip directional coupler with the high directivity," in *2004 IEEE MTT-S International Microwave Symposium Digest (IEEE Cat. No. 04CH37535)*, vol. 3. IEEE, 2004, pp. 1895–1898.

[75] M. Kumar, S. Subbarao, R. Menna and H.-C. Huang, "Monolithic gaas interdigitated couplers," *IEEE Transactions on Microwave Theory and Techniques*, vol. 31, no. 1, pp. 29–32, 1983.

[76] S. Kumar and T. Danshin, "Multisection broadband impedance transforming branchline quad hybrid suitable for mmic realisation," *Electronics Letters*, vol. 28, no. 14, pp. 1368–1370, 1992.

[77] S. Kumar, C. Tannous and T. Danshin, "A multisection broadband impedance transforming branch-line hybrid," *IEEE Transactions on Microwave Theory and Techniques*, vol. 43, no. 11, pp. 2517–2523, 1995.

[78] S. Kumpang, R. Phromloungsri and M. Chongcheawchamnan, "Design high-directivity parallel-coupled lines with step-impedance transmission lines," in *2007 Asia-Pacific Microwave Conference*. IEEE, 2007, pp. 1–4.

[79] J. Lamberg, M. Gawronski, J. Geddes, W. Carlyon, R. Hart, G. Dow, E. Holmes and M. Huang, "A compact high performance w-band fmcw radar front-end based on mmic technology," in *1999 IEEE MTT-S International Microwave Symposium Digest (Cat. No. 99CH36282)*, vol. 4. IEEE, 1999, pp. 1797–1800.

[80] J. Lange, "Interdigitated strip-line quadrature hybrid," in *1969 G-MTT International Microwave Symposium*, 1969, pp. 10–13.

[81] H. L. Lee, D.-H. Park, M.-Q. Lee and J.-W. Yu, "Reconfigurable 2x2 multi-port amplifier using switching mode hybrid matrices," *IEEE microwave and wireless components letters*, vol. 24, no. 2, pp. 129–131, 2013.

[82] S. Lee, T. Baek, M. Han, S. Choi, D. Ko and J. Rhee, "94 ghz mmic single balanced mixer for fmcw radar sensor application," in *Proceedings of 2012 5th Global Symposium on Millimeter-Waves*, 2012, pp. 351–354.

[83] R. Levy, "General synthesis of asymmetric multi-element coupled-transmission-line directional couplers," *IEEE Transactions on Microwave Theory and Techniques*, vol. 11, no. 4, pp. 226–237, 1963.

[84] L. Li, J.-F. Mao and L.-S. Wu, "A single-ended-to-balanced impedance-transforming branch-line coupler with arbitrary power division ratio," *IEEE Transactions on Microwave Theory and Techniques*, vol. 67, no. 3, pp. 949–956, 2019.

[85] C.-C. Lin, C.-H. Yu, H.-C. Kuo and H.-R. Chuang, "Design of 60-ghz 90-nm cmos balanced power amplifier with miniaturized quadrature hybrids," in *2014 IEEE Topical Conference on Power Amplifiers for Wireless and Radio Applications (PAWR)*. IEEE, 2014, pp. 52–54.

[86] K. Lin, Y. E. Wang, C.-K. Pao and Y.-C. Shih, "A ka-band fmcw radar front-end with adaptive leakage cancellation," *IEEE Transactions on Microwave Theory and Techniques*, vol. 54, no. 12, pp. 4041–4048, 2006.

[87] S. Lin, M. Eron, S. Turner and J. Sepulveda, "Development of wideband low-loss directional coupler with suspended stripline and microstrip line," *Electronics letters*, vol. 47, no. 25, pp. 1377–1379, 2011.

[88] D.-L. Luong, G. Acri, F. Podevin, D. Vincent, E. Pistono, A. Serrano and P. Ferrari, "Forward-wave directional coupler based on slow-wave coupled microstrip lines," *IET Microwaves, Antennas & Propagation*, vol. 13, no. 14, pp. 2486–2489, 2019.

[89] A. Mallet, A. Anakabe, J. Sombrin and R. Rodriguez, "Multiport-amplifier-based architecture versus classical architecture for space telecommunication payloads," *IEEE transactions on microwave theory and techniques*, vol. 54, no. 12, pp. 4353–4361, 2006.

[90] S. March, "A wideband stripline hybrid ring (correspondence)," *IEEE Transactions on Microwave Theory and Techniques*, vol. 16, no. 6, pp. 361–361, 1968.

[91] S. L. March, "Phase velocity compensation in parallel-coupled microstrip," in *1982 IEEE MTT-S International Microwave Symposium Digest*. IEEE, 1982, pp. 410–412.

[92] W. Marynowski, A. Kusiek, A. Walesieniuk and J. Mazur, "Investigations of broadband multilayered coupled line couplers," in *2008 14th Conference on Microwave Techniques*. IEEE, 2008, pp. 1–4.

[93] H. Mgombelo, H. Ali and M. Kissaka, "New impedance transforming rat-race hybrid ring," *Electronics Letters*, vol. 26, no. 13, pp. 837–839, 1990.

[94] W. Mizuhara, T. Shidei, A. Kosuge, T. Takeya, N. Miura, M. Taguchi, H. Ishikuro and T. Kuroda, "A 0.15 mm-thick non-contact connector for mipi using vertical directional coupler," in *2013 IEEE International Solid-State Circuits Conference Digest of Technical Papers*. IEEE, 2013, pp. 200–201.

[95] I. A. Mocanu, N. Militaru, G. Lojewski, T. Petrescu and M. G. Banciu, "Backward couplers using coupled composite right/left-handed transmission lines," in *2010 8th International Conference on Communications*. IEEE, 2010, pp. 267–270.

[96] R. K. Mongia, J. Hong, P. Bhartia and I. J. Bahl, *RF and microwave coupled-line circuits*. Artech house, 2007.

[97] J. Muller, C. Friesicke and A. F. Jacob, "Stepped impedance microstrip couplers with improved directivity," in *2009 IEEE MTT-S International Microwave Symposium Digest*. IEEE, 2009, pp. 621–624.

[98] J. Muller and A. F. Jacob, "Complex compensation of coupled line structures in inhomogeneous media," in *2008 IEEE MTT-S International Microwave Symposium Digest*. IEEE, 2008, pp. 1007–1010.

[99] D. P. Nguyen, B. L. Pham and A. Pham, "A compact ka-band integrated doherty amplifier with reconfigurable input network," *IEEE Transactions on Microwave Theory and Techniques*, vol. 67, no. 1, pp. 205–215, 2019.

[100] G. R. Nikandish, R. B. Staszewski and A. Zhu, "Unbalanced power amplifier: An architecture for broadband back-off efficiency enhancement," *IEEE Journal of Solid-State Circuits*, vol. 56, no. 2, pp. 367–381, 2021.

[101] A. E. Omer, G. Shaker, S. Safavi-Naeini, H. Kokabi, G. Alquié, F. Deshours and R. M. Shubair, "Low-cost portable microwave sensor for non-invasive monitoring of blood glucose level: novel design utilizing a four-cell csrr hexagonal configuration," *Scientific Reports*, vol. 10, no. 1, pp. 1–20, 2020.

[102] T. Padmaja, R. N'Gongo, P. Ratna, P. Vasu, J. S. Babu and V. Kirty, "A 18–40ghz monolithic gaas phemt low noise amplifier," in *2008 International Conference on Recent Advances in Microwave Theory and Applications*. IEEE, 2008, pp. 309–311.

[103] P. Pahl, S. Diebold, D. Schwantuschke, S. Wagner, R. Lozar, R. Quay, I. Kallfass and T. Zwick, "A 65–100 ghz impedance transforming hybrid coupler for a v-/w-band algan/gan mmic," in *2013 European Microwave Conference*. IEEE, 2013, pp. 1383–1386.

[104] S. J. Parisi, "180 degrees lumped element hybrid," in *IEEE MTT-S International Microwave Symposium Digest*, 1989, pp. 1243–1246 vol.3.

[105] R. Phromloungsri and M. Chongcheawchamnan, "A high directivity coupler design using an inductive compensation technique," in *2005 Asia-Pacific Microwave Conference Proceedings*, vol. 5. IEEE, 2005, pp. 4–pp.

[106] I. Piekarz, J. Sorocki, K. Janisz, K. Wincza and S. Gruszczynski, "Wideband three-section symmetrical coupled-line directional coupler operating in differential mode," *IEEE Microwave and Wireless Components Letters*, vol. 28, no. 6, pp. 488–490, 2018.

[107] I. Piekarz, J. Sorocki, K. Wincza, S. Gruszczynski and J. Papapolymerou, "High-performance differentially fed coupled-line directional couplers realised in inhomogeneous medium," *IET Microwaves, Antennas & Propagation*, vol. 13, no. 12, pp. 2005–2012, 2019.

[108] A. Podell, "A high directivity microstrip coupler technique," in *G-MTT 1970 International Microwave Symposium*. IEEE, 1970, pp. 33–36.

[109] D. M. Pozar, *Microwave engineering*.   John wiley & sons, 2009.

[110] I. Robertson, R. Herath, M. Gillick and J. Bharj, "Solid state power amplifier using impedance-transforming branch-line couplers for l-band satellite systems," in *1993 23rd European Microwave Conference*.   IEEE, 1993, pp. 448–450.

[111] S. Ryynänen, "The electromagnetic properties of food materials: a review of the basic principles," *Journal of food engineering*, vol. 26, no. 4, pp. 409–429, 1995.

[112] K. Sachse, "The scattering parameters and directional coupler analysis of characteristically terminated asymmetric coupled transmission lines in an inhomogeneous medium," *IEEE transactions on microwave theory and techniques*, vol. 38, no. 4, pp. 417–425, 1990.

[113] K. Sachse and A. Sawicki, "Quasi-ideal multilayer two-and three-strip directional couplers for monolithic and hybrid mics," *IEEE Transactions on microwave theory and techniques*, vol. 47, no. 9, pp. 1873–1882, 1999.

[114] I. Sakagami, M. Tahara and M. Fujii, "Planar four-way power divider using impedance-transforming branch-line couplers," in *2008 Asia-Pacific Microwave Conference*. IEEE, 2008, pp. 1–4.

[115] I. Sakagami and W. Tuya, "Impedance-transforming lumped-element co-directional couplers and their circuit structure," in *2005 Asia-Pacific Microwave Conference Proceedings*, vol. 3.   IEEE, 2005, pp. 4–pp.

[116] A. Sawicki and K. Sachse, "Novel coupled-line conductor-backed coplanar and microstrip directional couplers for pcb and ltcc applications," *IEEE Transactions on microwave theory and techniques*, vol. 51, no. 6, pp. 1743–1751, 2003.

[117] B. Sheleg and B. E. Spielman, "Broad-band directional couplers using microstrip with dielectric overlays," *IEEE Transactions on Microwave Theory and Techniques*, vol. 22, no. 12, pp. 1216–1220, 1974.

[118] J. Shi, J. Qiang and Q. Cao, "Single-layer balanced branch-line coupler," in *2016 IEEE 5th Asia-Pacific Conference on Antennas and Propagation (APCAP)*.   IEEE, 2016, pp. 17–18.

[119] J. Shi, J. Qiang, K. Xu, W. Qin, L. Zhou and Q. Cao, "A differential branch-line coupler," in *2015 IEEE 4th Asia-Pacific Conference on Antennas and Propagation (APCAP)*.   IEEE, 2015, pp. 431–432.

[120] K. Shibata, H. Yanagisawa and Y. Ishihata, "Three-line microstrip directional coupler with dielectric overlay," *Electronics Letters*, vol. 19, no. 22, pp. 911–912, 1983.

[121] R. Smolarz, K. Staszek, K. Wincza and S. Gruszczynski, "A 24 ghz microwave sensor with built-in calibration capability designed in mmic technology," *IEEE Access*, pp. 1–1, 2021.

[122] R. Smolarz, K. Wincza and S. Gruszczynski, "Design of low-loss directional couplers with compensated coupled-line sections in suspended microstrip technique," *International Journal of RF and Microwave Computer-Aided Engineering*, vol. 27, no. 8, p. e21125, 2017.

[123] R. Smolarz, K. Wincza and S. Gruszczynski, "Broadband low-loss impedance transforming rat-race coupler in suspended microstrip technique," in *2018 22nd International Microwave and Radar Conference (MIKON)*. IEEE, 2018, pp. 291–293.

[124] R. Smolarz, K. Wincza and S. Gruszczynski, "Impedance transforming rat-race couplers with modified lange section," *Journal of ElEctromagnEtic WavEs and applications*, vol. 32, no. 8, pp. 972–983, 2018.

[125] R. Smolarz, K. Wincza and S. Gruszczynski, "Impedance transforming tandem couplers with increased bandwidth and transformation ratio," *IEEE Microwave and Wireless Components Letters*, vol. 28, no. 4, pp. 299–301, 2018.

[126] R. Smolarz, K. Wincza and S. Gruszczynski, "Design of 3-db differentially-fed tandem directional couplers," in *2019 IEEE MTT-S International Wireless Symposium (IWS)*. IEEE, 2019, pp. 1–3.

[127] R. Smolarz, K. Wincza and S. Gruszczynski, "Chebyshev-response branch-line couplers with enhanced bandwidth and arbitrary coupling level," *Electronics*, vol. 9, no. 11, p. 1828, 2020.

[128] R. Smolarz, K. Wincza and S. Gruszczynski, "Modal phase velocity compensation in multilayer differentially fed directional couplers," *Microwave and Optical Technology Letters*, vol. 62, no. 5, pp. 1882–1887, 2020.

[129] J. Sorocki, I. Piekarz, I. Slomian, S. Gruszczynski and K. Wincza, "Single-layer coupled-line magic-ts utilizing left-handed transmission line sections," in *2014 20th International Conference on Microwaves, Radar and Wireless Communications (MIKON)*. IEEE, 2014, pp. 1–3.

[130] J. Sorocki, I. Piekarz, K. Wincza and S. Gruszczynski, "Impedance transforming directional couplers with increased achievable transformation ratio," *International Journal of Microwave and Wireless Technologies*, vol. 9, no. 3, pp. 509–513, 2017.

[131] J. Sorocki, K. Staszek, I. Piekarz, K. Wincza and S. Gruszczynski, "Directional couplers with reduced coupling requirements as connection of coupled-line sections and left-handed transmission lines," *IET Microwaves, Antennas & Propagation*, vol. 8, no. 8, pp. 580–588, 2014.

[132] K. Staszek, A. Szkudlarek, M. Kawa and A. Rydosz, "Microwave system with sensor utilizing go-based gas-sensitive layer and its application to acetone detection," *Sensors and Actuators B: Chemical*, vol. 297, p. 126699, 2019.

[133] K. Staszek, "Six-port calibration utilizing matched load and unknown calibration loads," *IEEE Transactions on Microwave Theory and Techniques*, vol. 66, no. 10, pp. 4617–4626, 2018.

[134] K. Staszek, I. Piekarz, J. Sorocki, S. Koryciak, K. Wincza and S. Gruszczynski, "Low-cost microwave vector system for liquid properties monitoring," *IEEE Transactions on Industrial Electronics*, vol. 65, no. 2, pp. 1665–1674, 2017.

[135] K. Staszek, K. Wincza and S. Gruszczynski, "Rigorous approach for design of differential coupled-line directional couplers applicable in integrated circuits and substrate-embedded networks," *Scientific reports*, vol. 6, p. 25071, 2016.

[136] E. Suijker, L. de Boer, G. Visser, R. van Dijk, M. Poschmann and F. van Vliet, "Integrated x-band fmcw front-end in sige bicmos," in *The 40th European Microwave Conference*. IEEE, 2010, pp. 1082–1085.

[137] Y. Sun and A. P. Freundorfer, "A new overlay coupler for direct digital modulator in gaas hbt," *IEEE transactions on microwave theory and techniques*, vol. 52, no. 8, pp. 1830–1835, 2004.

[138] A. Talebzadeh, A. Mohammadi and A. Abdipour, "Miniaturized branch-line coupler for 60 ghz frequency band applications using cmos technology," in *2012 Second Conference on Millimeter-Wave and Terahertz Technologies (MMWaTT)*, 2012, pp. 44–47.

[139] P. V. Testa, C. Carta, B. Klein, R. Hahnel, D. Plettemeier and F. Ellinger, "A 210-ghz sige balanced amplifier for ultrawideband and low-voltage applications," *IEEE Microwave and Wireless Components Letters*, vol. 27, no. 3, pp. 287–289, 2017.

[140] C. Toker, M. Saglam, M. Ozme and N. Gunalp, "Branch-line couplers using unequal line lengths," *IEEE Transactions on Microwave Theory and Techniques*, vol. 49, no. 4, pp. 718–721, 2001.

[141] A. L. Topa, C. R. Paiva and A. M. Barbosa, "Novel propagation features of double negative h-guides and h-guide couplers," *Microwave and Optical Technology Letters*, vol. 47, no. 2, pp. 185–190, 2005.

[142] I. Toyoda, T. Hirota, T. Hiraoka and T. Tokumitsu, "Multilayer mmic branch-line coupler and broad-side coupler," in *IEEE 1992 Microwave and Millimeter-Wave Monolithic Circuits Symposium Digest of Papers*, 1992, pp. 79–82.

[143] I. Toyoda, T. Hirota, T. Hiraoka and T. Tokumitsu, "Multilayer mmic branch-line coupler and broad-side coupler," in *IEEE 1992 Microwave and Millimeter-Wave Monolithic Circuits Symposium Digest of Papers*. IEEE, 1992, pp. 79–82.

[144] S. Trabelsi and S. O. Nelson, "Microwave sensing of quality attributes of agricultural and food products," *IEEE Instrumentation Measurement Magazine*, vol. 19, no. 1, pp. 36–41, 2016.

[145] F. Uysal, "Phase-coded fmcw automotive radar: System design and interference mitigation," *IEEE Transactions on Vehicular Technology*, vol. 69, no. 1, pp. 270–281, 2019.

[146] S. Uysal and H. Aghvami, "Synthesis, design, and construction of ultra-wide-band nonuniform quadrature directional couplers in inhomogeneous media," *IEEE transactions on microwave theory and techniques*, vol. 37, no. 6, pp. 969–976, 1989.

[147] J. Villotte, M. Aubourg and Y. Garault, "Modified suspended striplines for microwave integrated circuits," *Electronics Letters*, vol. 14, no. 18, pp. 602–603, 1978.

[148] R. Vishnu, "Design and development of a dual directional coupler with transformers for hf band applications," in *2016 International Conference on Communication Systems and Networks (ComNet).* IEEE, 2016, pp. 117–119.

[149] F. Voineau, B. Martineau, M. Sié, A. Ghiotto and E. Kerhervé, "A differential vertical hybrid coupler and low capacitance rf pads for millimeter-wave applications in 28 nm cmos fdsoi," in *2018 IEEE 18th Topical Meeting on Silicon Monolithic Integrated Circuits in RF Systems (SiRF).* IEEE, 2018, pp. 57–59.

[150] H.-N. Wang, Y.-W. Huang and S.-J. Chung, "Spatial diversity 24-ghz fmcw radar with ground effect compensation for automotive applications," *IEEE Transactions on Vehicular Technology*, vol. 66, no. 2, pp. 965–973, 2016.

[151] S. Wang, A. Pohl, T. Jaeschke, M. Czaplik, M. Köny, S. Leonhardt and N. Pohl, "A novel ultra-wideband 80 ghz fmcw radar system for contactless monitoring of vital signs," in *2015 37th Annual International Conference of the IEEE Engineering in Medicine and Biology Society (EMBC).* IEEE, 2015, pp. 4978–4981.

[152] T.-P. Wang and S.-H. Chiang, "A high-gain low-power low-noise-figure differential cmos lna with 33% current-reused negative-conductance accommodation structure," in *2015 28th IEEE International System-on-Chip Conference (SOCC).* IEEE, 2015, pp. 78–81.

[153] Y. Wang, K. Ma and S. Mou, "A transformer-based 3-db differential coupler," *IEEE Transactions on Circuits and Systems I: Regular Papers*, vol. 65, no. 7, pp. 2151–2160, 2017.

[154] C. Wei, R. F. Harrington, J. R. Mautz and T. K. Sarkar, "Multiconductor transmission lines in multilayered dielectric media," *IEEE Transactions on Microwave Theory and Techniques*, vol. 32, no. 4, pp. 439–450, 1984.

[155] D. Willems and I. Bahl, "An mmic-compatible tightly coupled line structure using embedded microstrip," *IEEE transactions on microwave theory and techniques*, vol. 41, no. 12, pp. 2303–2310, 1993.

[156] K. Wincza and S. Gruszczynski, "Method for the design of low-loss suspended stripline directional couplers with equalized inductive and capacitive coupling coefficients," *Microwave and optical technology letters*, vol. 51, no. 2, pp. 315–319, 2009.

[157] K. Wincza and S. Gruszczynski, "Three-section symmetrical 3-db directional coupler in multilayer microstrip technology designed with the use of multi-technique compensation," *Microwave and Optical Technology Letters*, vol. 51, no. 4, pp. 902–906, 2009.

[158] K. Wincza and S. Gruszczynski, "Asymmetric coupled-line directional couplers as impedance transformers in balanced and n-way power amplifiers," *IEEE transactions on microwave theory and techniques*, vol. 59, no. 7, pp. 1803–1810, 2011.

[159] K. Wincza, S. Gruszczynski and S. Kuta, "Approach to the design of asymmetric coupled-line directional couplers with the maximum achievable impedance-transformation ratio," *IEEE transactions on microwave theory and techniques*, vol. 60, no. 5, pp. 1218–1225, 2012.

[160] K. Wincza, I. Piekarz and S. Gruszczynski, "Two-section asymmetric coupled-line impedance transforming directional couplers," *IET Microwaves, Antennas & Propagation*, vol. 9, no. 4, pp. 343–350, 2014.

[161] Y. Wu, M. Her, Y. Wang and M. Hsu, "Stepped-impedance directional coupler with enhanced isolation using interdigital capacitance compensation," *Electronics Letters*, vol. 41, no. 10, pp. 598–599, 2005.

[162] M. Yamagata and H. Hashemi, "A differential x/ku-band low noise amplifier in 0.13-\ μ m cmos technology," *IEEE microwave and wireless components letters*, vol. 17, no. 12, pp. 888–890, 2007.

Kraków, 21.07.2021

OŚWIADCZENIE AUTORA PRACY

Oświadczam, świadomy odpowiedzialności karnej za poświadczenie nieprawdy, że niniejszą pracę doktorską wykonałem osobiście i samodzielnie oraz że nie korzystałem ze źródeł innych niż wymienione w pracy.

. . . .

(Podpis)